Laser Guide Star Only Adaptive Optics

The Development of Tools and Algorithms for the Determination of Laser Guide Star Tip-Tilt

Andrew Paul Reeves

A thesis presented for the degree of
Doctor of Philosophy

Centre for Advanced Instrumentation
The University of Durham
United Kingdom
6th July 2015

Laser Guide Star Only Adaptive Optics

The Development of Tools and Algorithms for the Determination of Laser Guide Star Tip-Tilt

Andrew Paul Reeves

Abstract

Adaptive Optics (AO) is a technology which corrects for the effects of the atmosphere and so improves the optical quality of ground based astronomical observations. The bright "guide stars" required for correction are not available across the entire sky, so Laser Guide Stars (LGSs) are created. A Natural Guide Star (NGS) is still required to correct for tip-tilt as the LGS encounters turbulence on the uplink path resulting in unpredictable "jitter", hence limiting corrected sky coverage. In this thesis an original method is proposed and investigated that promises to improve the correction performance for tomographic AO systems using only LGSs, and no NGS, by retrieving the LGS uplink tip-tilt.

To investigate the viability of this method, two unique tools have been developed. A new AO simulation has been written in the Python programming language which has been designed to facilitate the rapid development of new AO concepts. It features realistic LGS simulation, ideal to test the method of LGS uplink tip-tilt retrieval. The Durham Real-Time Adaptive Optics Generalised Optical Nexus (DRAGON) is a laboratory AO test bench nearing completion, which features multiple LGS and NGS Wavefront Sensors (WFSs) intended to further improve tomographic AO. A novel method of LGS emulation has been designed, which re-creates focus anisoplanatism, elongation and uplink turbulence. Once complete, DRAGON will be the ideal test bench for further development of LGS uplink tip-tilt retrieval.

Performance estimates from simulation of the LGS uplink tip-tilt retrieval method are presented. Performance is improved over tomographic LGS AO systems which do not correct for tip-tilt, giving a modest improvement in image quality over the entire night sky. Correction performance is found to be dependent on the atmospheric turbulence profile. If combined with ground layer adaptive optics, higher correction performance with a very high sky coverage may be achieved.

Contents

List of Figures

List of Tables

List of listings

Declaration

The work in this thesis is based on research carried out at the Centre for Advanced Instrumentation, the Department of Physics, University of Durham, England. No part of this thesis has been submitted elsewhere for any other degree or qualification and it is the sole work of the author unless referenced to the contrary in the text.

Some of the work presented in this thesis has been published in conference proceedings - the relevant publications are listed below.

Publications

S. Rolt, A. Basden, N. Bharmal1a, D. Bramall, N. Dipper, D. Geng, T. Morris, R. Myers, and A. Reeves. DRAGON, a flexible, visible-light AO testbed. In *Second International Conference on Adaptive Optics for Extremely Large Telescopes.*, volume 1, page 8P, 2011

A. P. Reeves, R. M. Myers, T. J. Morris, A. G. Basden, N. A. Bharmal, S. Rolt, D. G. Bramall, N. A. Dipper, and E. J. Younger. DRAGON: a wide-field multipurpose real time adaptive optics test bench. In *SPIE Astronomical Telescopes+ Instrumentation*, pages 84474Y–84474Y. International Society for Optics and Photonics, 2012

A. Reeves, R. Myers, T. Morris, A. Basden, and N. Bharmal. Real-Time Laser Guide Star Elongation and Uplink Turbulence in the Lab. In *Proceedings of the Third AO4ELT Conference*, volume 1, page 35, 2013

T. Morris, E. Gendron, A. Basden, O. Martin, J. Osborn, D. Henry, Z. Hubert, G. Sivo, D. Gratadour, F. Chemla, et al. Multiple Object Adaptive Optics: Mixed NGS/LGS tomography. In *Proceedings of the Third AO4ELT Conference*, volume 1, page 114, 2013

N. Dipper, A. Basden, U. Bitenc, R. Myers, A. Richards, and E. Younger. Adaptive Optics Real-time Control Systems for the E-ELT. In *Proceedings of the Third AO4ELT Conference*, volume 1, page 41, 2013

Acknowledgements

There are a lot of people who have helped enormously with this thesis and throughout my PhD studies.

Firstly, and most importantly, thank you to Hannah, who has kept me going through all the hard bits over the last few years. I'm especially grateful for her help during the "write-up", she has read every word of this thesis, some of them many times. She is, I imagine, rather bored of it by now. Nevertheless, she has continued to provide excellent advice which is of great use. Our cat, Mia's advice has been rather less useful – I suspect it usually involves biscuits.

I am incredibly grateful to my supervisors, Richard Myers and Tim Morris, for allowing me to do my PhD with the CfAI, I have had an incredibly fun, interesting and fulfilling three and a half years. They have provided crucial advice on experimental and theoretical matters, as well as what seems to have been an awful lot of beer. I would also like to acknowledge the funding of STFC who made this project possible in the first place.

Alistair Basden has created the fantastic real-time control system, DARC, which has powered many of the experiments presented here and his help with it has been indispensable. Equally important, frequent conversations with James Osborn, Nazim Ali Bharmal and Tim Butterley have turned my mind to more mathematical methods of problem solving. Discussions with Nigel Dipper and, more recently, Matthew Townson have guided me through the creation of the new AO simulation.

Thanks also to many others who have provided their advice or their time in helping with various bits in the DRAGON project, Urban Bitenc, Eddy Younger, Mark Dubbeldam, Steve Rolt and David Bramall. Thank you also to all of those in CfAI who have generally made the last few years so enjoyable.

Nomenclature

AO Adaptive Optics

ALTAIR Altitude Conjugate Adaptive Optics for the Infra-red

ANN Artificial Neural Network

AOF Adaptive Optics Facility

APD Avalanche Photo-Diode

API Application Programming Interface

ARGOS Advanced Rayleigh Ground Layer Adaptive Optics System

BLAS Basic Linear Algebra Subprograms

CCD Charged Coupled Device

CfAI Centre for Advanced Instrumentation

CFHT Canada France Hawaii Telescope

CPU Central Processing Unit

CURE Cumulative Reconstructor

DARC Durham Adaptive optics Real-time Controller

DASP Durham Adaptive Optics Simulation Platform

DM Deformable Mirror

DOE Diffractive Optical Element

DPO Durham Precision Optics

DRAGON Durham Real-Time Adaptive Optics Generalised Optical Nexus

E-ELT European Extremely Large Telescope

ELT Extremely Large Telescope

ESO European Southern Observatory

FFT Fast Fourier Transform

FFTW Fastest Fourier Transform in the West

FPGA Field Programmable Gate Array

FWHM Full Width at Half Maximum

GeMS Gemini Multi-Conjugate Adaptive Optics System

GigE Gigabit Ethernet

GPI Gemini Planet Imager

GPU Graphical Processing Unit

GLAO Ground Layer Adaptive Optics

GLAS Ground Layer Adaptive Optics System

GMT Giant Magellan Telescope

GUI Graphical User Interface

HOMER Hartmann Oriented Multi-conjugate Experimental Resource

HOT High Order Test-bench

HST Hubble Space Telescope

IFU Integral Field Unit

JIT Just-In-Time

JWST James Webb Space Telescope

LBT Large Binocular Telescope

LED Light Emitting Diode

LGS Laser Guide Star

LLT Laser Launch Telescope

LTAO Laser Tomographic Adaptive Optics

MAD Multi-conjugate Adaptive optics Demonstrator

MARTINI Multiple Aperture Real Time Image Normalisation Instrument

MCAO Multi-Conjugate Adaptive Optics

MACAO Multi-Application Curvature Adaptive Optics

MEMS Micro-Electro-Mechanical System

MMSE Minimum Mean Square Error

MOAO Multi-Object Adaptive Optics

MOS Multi-Object Spectrograph

MPI Message Passing Interface

MTF Modulation Transfer Function

MVM Matrix Vector Multiplication

NAOMI Nasmyth Adaptive Optics for Multi-purpose Instrumentation

NAOS Nasmyth Adaptive Optics System

NGS Natural Guide Star

NIR Near Infra-Red

OOMAO Object-Oriented, *Matlab*® & Adaptive Optics

OpenCL Open Compute Library

ONERA Office National d'études et de Recherches Aérospatiales

OTF Optical Transfer Function

PSF Point Spread Function

PyAOS Python Adaptive Optics Simulation

Pyro Python Remote Objects

RMS Root Mean Square

RTCS Real-Time Control System

SAXO SPHERE Adaptive Optics for eXoplanet Observation

SCAO Single Conjugate Adaptive Optics

SH Shack-Hartmann

SNR Signal to Noise Ratio

SPHERE Spectro-Polarimetry High-contrast Exoplanet Research

TAS Target Acquisition System

TMT Thirty Metre Telescope

VHDL VHSIC Hardware Description Language

VHSIC Very High Speed Integrated Circuit

VLT Very Large Telescope

VOLT Victoria Open Loop Test-bench

WFS Wavefront Sensor

WHT William Herschel Telescope

XAO Extreme Adaptive Optics

YAO Yorick Adaptive Optics

If the Theory of making Telescopes could at length be fully brought into Practice, yet there would be certain Bounds beyond which Telescopes could not perform. For the Air through which we look upon the Stars, is in a perpetual Tremor; as may be seen by the tremulous Motion of Shadows cast from high Towers, and by the twinkling of the fix'd Stars. But these Stars do not twinkle when viewed through Telescopes which have large apertures. For the Rays of Light which pass through divers parts of the aperture, tremble each of them apart, and by means of their various and sometimes contrary Tremors, fall at one and the same time upon different points in the bottom of the Eye, and their trembling Motions are too quick and confused to be perceived severally. And all these illuminated Points constitute one broad lucid Point, composed of those many trembling Points confusedly and insensibly mixed with one another by very short and swift Tremors, and thereby cause the Star to appear broader than it is, and without any trembling of the whole. Long Telescopes may cause Objects to appear brighter and larger than short ones can do, but they cannot be so formed as to take away that confusion of the Rays which arises from the Tremors of the Atmosphere.

Opticks, Isaac Newton (1730)

Chapter 1

Introduction to Adaptive Optics

1.1 A Short History of Adaptive Optics

1.1.1 Astronomy in the Early 20th Century

As humanity has progressed, so has our ability to observe the cosmos in greater detail. Adaptive Optics represents one of the most recent development in the history of astronomy, allowing us to study smaller objects, at further distances, in ever greater detail.

Throughout the 20th Century optical telescopes have steadily increased in size. Larger telescopes allow a greater light collecting area, enabling us to observe stars, galaxies and planets further from the Earth. Just as significantly, larger telescopes theoretically provide greater resolution so by increasing the diameter of a telescope, one can observe smaller or further targets (Rayleigh, 1880).

The modern age of astronomy was marked by the development of the Mount Wilson observatory in Los Angeles County, California. Observations and spectra were recorded onto photographic film, using the 60 inch (1.52 m) and 100 inch (2.54 m) diameter telescopes, with exposures lasting as long as 11 hours. These telescopes brought huge numbers of faint stars, star clusters and galaxies into range, providing a wealth of new information on the temperatures, compositions, motion distributions and distances of stars (Hardy, 1998). It was also where Edwin Hubble famously determined the relationship between the distance and the velocity of “nebulae”, establishing the scale and the expansion of the universe (Hubble, 1929).

The next major milestone in telescope construction, was the creation of the 200 inch (5.1 m) Hale telescope at the Palomar observatory, also in California. This represented a doubling of telescope diameter, effectively quadrupling the light collecting area. Ground breaking work was undertaken, such as the identification of distinct stellar populations of different age and elemental composition, leading to a new understanding of galaxy formation and stellar evolution (Greenstein and Tandberg Hanssen, 1954; Baade and Swope, 1955).

1.1.2 Problems in the Air

Yet the Hale telescope represented a plateau in ground based telescope design. Though the replacement of photographic film with electronic photo-electric detectors such as Charged

Coupled Devices (CCDs) vastly increased sensitivity, the full potential resolution of even the Hale telescope was rarely reached. This is because light must pass through atmospheric turbulence before arriving at the telescope. Atmospheric turbulence mixes air with differing temperatures, and hence with different refractive indices. As a result the light passing through the atmosphere is deviated. As the turbulence moves, the distortions quickly change and hence the optical resolution of long exposure images is rapidly decreased. The blurring of the astronomical images has the effect of making telescopes less light efficient as light from a single point is spread across a larger area on the detector, so it is effectively not as bright. This lost light also significantly adds to background noise across the rest of the image. To some extent this blunts the advantages of increased light gathering area when making telescopes larger.

One solution to the problem of atmospheric turbulence is to avoid it entirely by launching telescopes into space. This approach has resulted in projects such as the Hubble Space Telescope (HST)(Williams et al., 1996), the Herschel telescope (Pilbratt et al., 2010) and the upcoming James Webb Space Telescope (JWST) (Gardner et al., 2006). Existing space telescopes have made enormous advances in the field of astronomy, allowing reliably high spatial resolution in all sections of the sky. With an 8 m diameter primary mirror the JWST will no doubt provide similar advances again. However space telescopes are very expensive to produce and launch and once in position they are difficult or even impossible to maintain and upgrade. For these reasons it is vital that astronomers have access to high resolution ground based telescopes which can compete with, or at the very least complement, space telescopes.

1.1.3 The Beginnings of Adaptive Optics

Adaptive Optics is a technology with the aim of correcting for the optical effects of atmospheric turbulence, allowing ground based telescopes to achieve their potential resolution and light efficiency. The idea was initially proposed by Horace W. Babcock in 1953, though contemporary technology was not suitably advanced to realise the concept (Babcock, 1953). The idea of compensating for the effects of atmospheric turbulence was developed further in 1972 when the U.S. Department of Defence was attempting to better observe orbiting Soviet satellites. Their experiments were successful and it was not long before the potential benefits to astronomy became apparent (Hardy, 1998).

Experiments into astronomical AO were begun by The Office National d'études et de Recherches Aérospatiales (ONERA) at the 1.52 m telescope of the Observatoire de Haute Provence. This experimental system was named "COME-ON" and an image showing the effects of AO correction is shown Fig. 1.1 (Rousset et al., 1990). The lure of AO is clear, one can observe what seems to be a single star, then turn the AO system on to discover the single star was in fact a binary system. Facility AO systems offering modest gains in image quality were soon built, such as the Multiple Aperture Real Time Image Normalisation Instrument (MARTINI) system on the William Herschel Telescope (WHT) (Doel et al., 1991). Laser Guide Stars (LGSs) which had again been tested first by the U.S. Department of Defence began to be used for astronomical AO to account for the lack of suitably bright

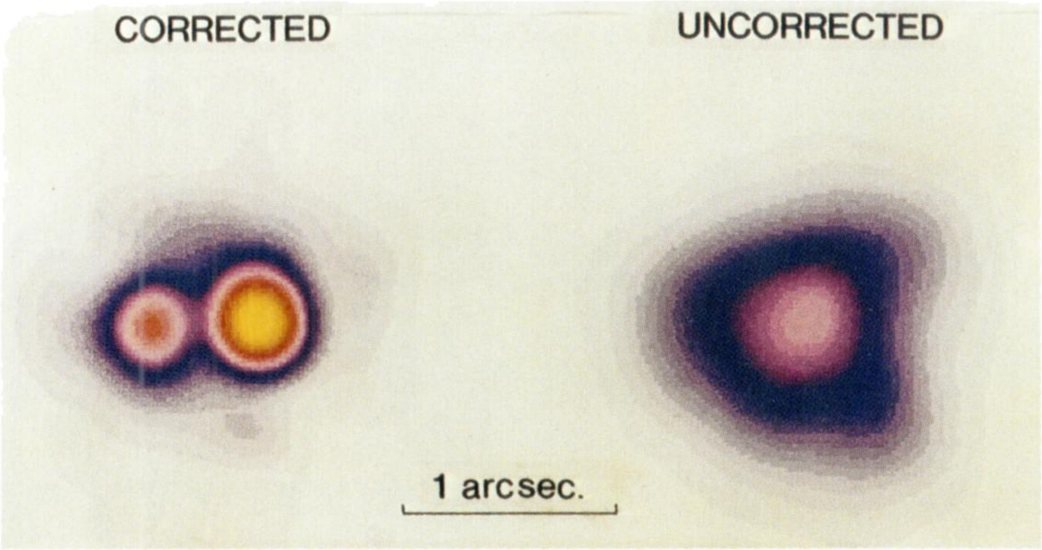

Figure 1.1: A pair of images from the COME-ON AO system (Rousset et al., 1990). The image on the right shows an uncorrected star as observed from the 1.52 m telescope of the Observatoire de Haute Provence. On the left is the AO corrected image, where it is now obvious that the “star” is actually a binary pair.

guide stars in some parts of the sky (Foy and Labeyrie, 1985; Fugate et al., 1994; Max et al., 1997).

1.1.4 Adaptive Optics Now and into the Future

A majority of the new generation of 8 to 10 m observatories have been equipped with AO systems, such as the Very Large Telescope (VLT) (Brandner et al., 2002), Keck (Wizinowich et al., 2000a), Gemini (Herriot et al., 2000), and Subaru (Takami et al., 1998). LGS systems are used to relax the requirements on the AO guide star allowing AO correction across more of the night sky. They have begun to become commonplace amongst facilities featuring AO corrected instruments (Boccas et al., 2006; Wizinowich et al., 2006; Hayano et al., 2008). Using AO, modern telescopes can provide diffraction limited resolution and high throughput, achieving the theoretical resolution and throughput of primary mirrors of 8 m diameter and upwards.

The coming generation of Extremely Large Telescopes (ELTs) offers a new challenge to AO scientists. The huge diameter of ELT scale systems creates problems for all components of AO systems. Simply making components with the required size and number of correction elements to cover the full diameter is a challenge (Gilmozzi and Spyromilio, 2007). Controlling the huge number of elements with current control algorithms at an adequate frame rate stretches even the power of the fastest current computers (Feng et al., 2012). The size of the structure of ELTs make them very prone to vibrations that must be compensated for best AO performance (Pott et al., 2012). Research is currently being undertaken into all these issues to ensure that AO systems for ELTs are successful.

Even with a LGS, a natural star is still required for correction. The LGS moves in the sky due to turbulence, so conventional LGS systems cannot provide “tip-tilt” information, without which the image wanders on the detector. For current LGS systems a Natural Guide Star (NGS) is required to provide this tip-tilt information. Much of the sky is made unavailable to AO systems due to a lack of suitably bright guide stars. State of the art AO systems are being designed which observe multiple laser or natural guide stars simultaneously in order to further increase the quality and availability of correction (Gendron et al., 2011; Rigaut et al., 2012), but as yet none can offer complete correction over the entire night sky.

1.2 Basic Adaptive Optics Operation

Studying Adaptive Optics (AO) can seem a daunting prospect when first approaching the subject as current, state of the art, systems can feature multiple Wavefront Sensors (WFSs), Deformable Mirrors (DMs), lasers and require complex software and equipment for real-time control. Despite this, the basic principle behind AO is remarkably simple.

Light from an astronomical science target such as a distant galaxy, a star or a planet, which has become aberrated by its propagation through the atmosphere enters a telescope. The light is directed to a DM, a mirror that can rapidly change its shape, which is configured in such a way to remove the aberration from the light. After this point the light is split into a “science” stream and an AO stream, often using a dichroic beam splitter to split the light by wavelength band. The science light is brought to a focus and a corrected image is formed onto an imaging detector or a spectrograph.

The AO path is directed to a WFS, used to measure the optical aberration introduced to the science target light by the atmosphere. Information from the WFS is processed by a computational system, termed the Real-Time Control System (RTCS), and the required correction is calculated. The DM is now updated to a better shape with which to correct the atmospheric aberrations. This process is illustrated in Fig. 1.2. This configuration of AO system is often termed a Single Conjugate Adaptive Optics (SCAO) system, as the WFS and DM are optically conjugate to only one plane - usually the telescope pupil.

1.3 Thesis Motivation

Traditionally, astronomers have sought to observe sections of the sky which are far from bright sources in order to reduce background noise. It is highly desirable that further studies can be performed in these areas with the increased light efficiency and resolution offered by AO. Conversely, AO can only provide significant correction when the science target, or a nearby star, is bright enough to be used for the purpose of wavefront sensing. An excellent example is the “Hubble Deep Field”, taken close to the galactic pole away from bright sources which could be used as a Natural Guide Star (NGS) for AO corrected ground based telescope follow-up studies (Williams et al., 1996).

Methods exist which can increase the fraction of the sky available for AO correction. These include the use of Laser Guide Stars (LGSs) and multiple WFSs to build a tomographic vertical profile of the atmospheric turbulence. However, because of the uplink effect on LGSs,

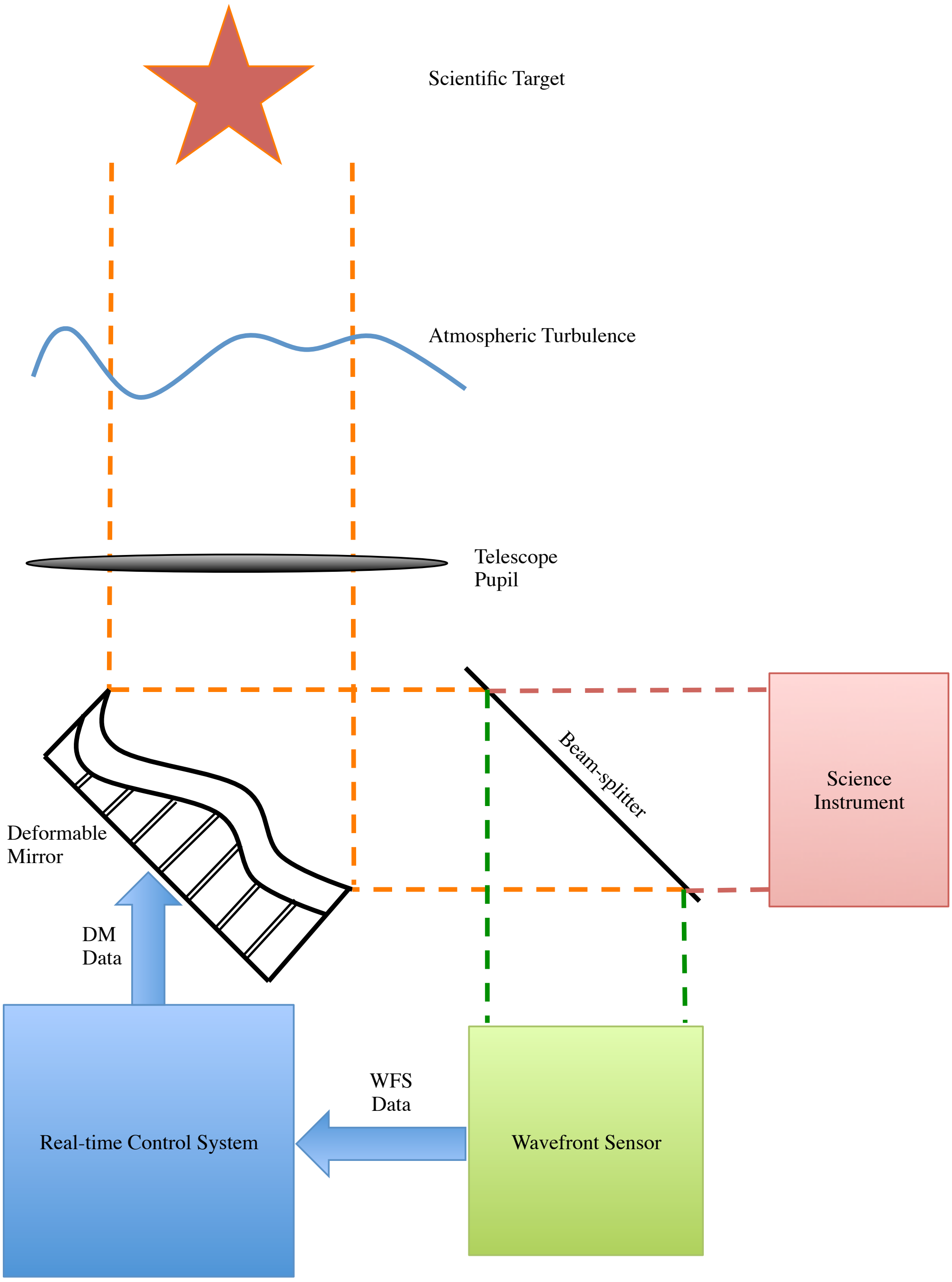

Figure 1.2: A cartoon showing the operation of a simple SCAO system. A small proportion of light from a science target is used to perform wavefront sensing. Data from the WFSs is sent to an RTCS to be processed, and a new shape sent to the DM. Meanwhile, a science instrument observes a corrected image.

none can provide good correction with full “sky-coverage”, that is, there are scientific targets of interest for which AO is unavailable. If the need for NGSs could be removed then AO could be used to study the entire sky, including areas far from bright sources. Even a relaxing of the requirements for an NGS would allow more sources to be used and improve sky coverage for many applications.

In this thesis a method is proposed to improve the sky-coverage of AO systems using tomographic LGS AO systems by retrieving the LGS uplink tip-tilt signal and integrating it into the correction algorithm. This approach may reduce or, for some scientific applications, even remove the need for a dedicated NGS as the majority of information required for correction can be obtained from LGSs alone. Without the need for a NGS the entire sky is available for AO correction and the resolving and light correcting power of modern ground based telescopes can be unleashed on all astronomical targets.

The development of new control algorithms and components for AO is vital to improve the performance of both existing telescopes and future Extremely Large Telescopes (ELTs). A further aim of the project is the development of two tools, a new AO simulation and a novel laboratory test bench, which can be used to rapidly develop and deploy such improvements. These tools will be indispensable in investigating the potential of the LGS uplink tip-tilt retrieval algorithm.

1.4 Thesis Synopsis

To understand fully how improved full sky-coverage AO correction can be achieved it is first necessary to fully understand modern AO systems and the statistical description of atmospheric turbulence. These are explained in Chapter 2. A review of contemporary AO systems is contained in Chapter 3, with a particular focus on LGSs and tomographic AO systems.

A new flexible and user-oriented AO simulation has been created and this is presented in Chapter 4. The Durham Real-Time Adaptive Optics Generalised Optical Nexus (DRAGON) is an advanced AO lab test-bench that has also been constructed. DRAGON has many novel features such as multiple LGS and NGS WFSs. Most relevantly, a unique method of LGS creation has been implemented which includes an accurate method of emulating LGS uplink effects in real time. DRAGON is described in detail in Chapter 5.

Chapter 6 introduces the method of uplink tip-tilt retrieval and describes its theoretical basis. Results of this method from the simulation are presented in Chapter 7. Finally, conclusions are drawn on the method and the suitability of the simulation and DRAGON is assessed.

Chapter 2

Theoretical Considerations

2.1 Atmospheric Turbulence

Before commencing a study of tomographic Adaptive Optics (AO) systems it is necessary to understand the basic theory describing atmospheric turbulence. Only by accounting for the underlying statistical properties of the turbulence can an AO system be successfully optimised.

Though an AO system is often called upon to remove semi-static errors caused by imperfections or misalignments in the telescope optical train, these tend to vary slowly, if at all. The requirements for correcting atmospheric turbulence are much more stringent as turbulence changes quickly, and spatial scales are shorter.

When searching for a theoretical description of the effects of atmospheric turbulence on astronomical light, it is useful that there is a large difference between the turbulence scale and that of the light. Atmospheric turbulence eddies have a typical scale of 10 cm and visible light a wavelength of $\approx 500\,\mathrm{nm}$, a difference of some 200,000 times. For the most part this means that diffraction can be ignored as the diffraction angles are very small and a geometric ray tracing approach can be used. The turbulence also varies on a much larger time scale than the light, the typical variation of the turbulence is about 12 orders of magnitude larger than the time period of a cycle of light. This allows us to consider the atmosphere as frozen in time with respect to the light's travel (Hardy, 1998).

2.1.1 Kolmogorov Theory

2.1.1.1 Structure Function

The turbulence in the atmosphere is ultimately caused by heating from the sun. During the day energy is passed to the air through solar radiation causing movement of air. At night turbulence is caused by the mixing of large air masses with differing temperatures. It has been noted that turbulence is not a simple process to model analytically (Fefferman, 2000), as it is largely a random process but it is possible to model its statistical properties. In 1941 Kolmogorov proposed a mathematical description of these properties (Kolmogorov, 1941). In this model energy is added to the air over a large spatial scale, the "outer-scale", which breaks down to ever smaller scales, eventually reaching an "inner-scale" whereby the energy is dissipated as friction between molecules.

The Reynolds number provides a metric to determine whether fluid flow will be turbulent or laminar (Reynolds, 1894). It is defined as

$$Re = \frac{V_0 L_0}{\nu_0} \tag{2.1}$$

where V_0 is the characteristic velocity of the fluid, L_0 its characteristic size and ν_0 its viscosity. A moderately sized atmospheric disturbance may have a size of 15 m, velocity $1\,\mathrm{m\,s^{-1}}$ and the viscosity of air is $15 \times 10^{-6}\,\mathrm{m^2\,s^{-1}}$, resulting in a Reynolds number of 1×10^6, exceeding the critical value for air of ≈ 2300 (Warhaft, 1997), meaning that airflow in the atmosphere is almost always turbulent (Hardy, 1998).

This process continues in a steady state where that the input energy is equal to the viscous energy dissipation. The velocity fluctuations, V ($\mathrm{m\,s^{-1}}$), are dependant upon the turbulence scale size, l (m), and the rate of energy input, ϵ ($\mathrm{kg\,m^2\,s^{-3}}$). Dimensional analysis leads to the conclusion that

$$V \propto \epsilon^{1/3} l^{1/3} \tag{2.2}$$

As we are only interested in the difference in the properties of turbulence, not absolute values themselves, a structure function is defined describing the difference in velocity between two points in the turbulence medium. Using Eq. (2.2),

$$D_v(r) = \langle |V(x) - V(x+r)|^2 \rangle = C_V^2 r^{2/3} \tag{2.3}$$

where, $\langle\rangle$ represents an ensemble average, $V(x)$ is the velocity at some point x, and $V(x+r)$ the velocity at a point r away. C_V^2 is a parameter depending on the energy input into the medium.

This is a velocity structure function but when considering the effects of turbulence upon light we are really interested in the fluctuation of refractive index within the medium. This inflicts phase delays to rays of light resulting in aberrations. Refractive index fluctuations are related to velocity fluctuations and there is a similar structure function describing them (Roddier, 1981).

$$D_N(r) = \langle |n(x) - n(x+r)|^2 \rangle = C_N^2 r^{2/3} \tag{2.4}$$

Where $n(x)$ and $n(x+r)$ are the refractive indices at two points separated by r and the value C_N^2 is called the refractive index structure coefficient which describes the strength of the fluctuation. The process is described as "homogeneous" as it depends only upon the magnitude of r and not its direction. It is also "isotropic" as it does not depend on the position of point x, only the separation between x and $x + r$. The refractive index structure function describes the strength of the turbulence and does vary, but over much larger distances than r so can be considered constant. The limits of r between which Eq. (2.4) is valid are the outer and inner scales where energy is input and dissipated respectively. The integral of this value over the astronomical line of site gives a measure of the total wavefront degradation or astronomical "seeing" (Roddier, 1981).

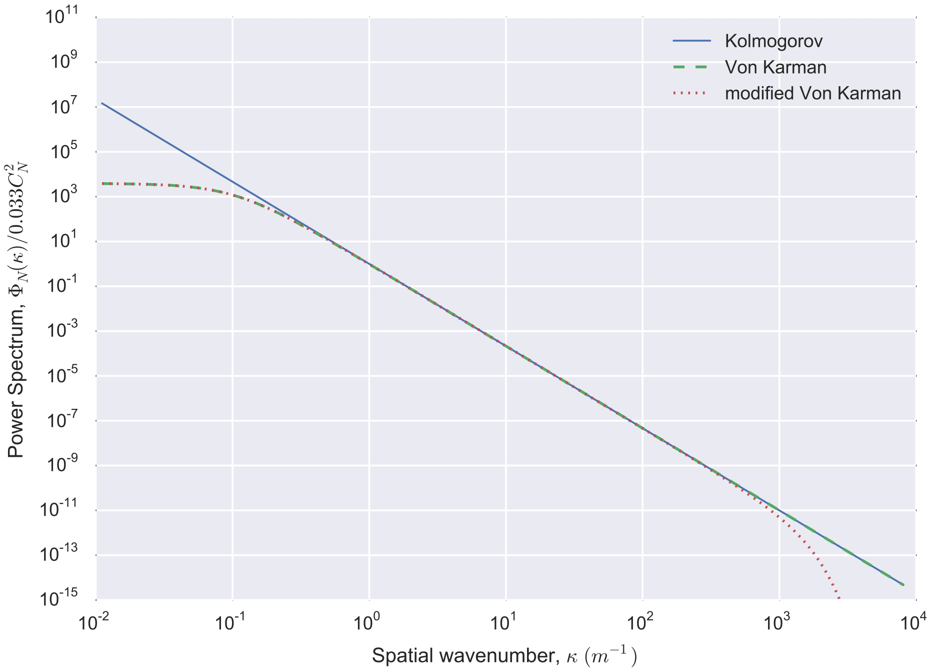

Figure 2.1: A plot of the Kolmogorov, von Kármán and modified von Kármán refractive index variation spatial power spectra. In the Kolmogorov regime the $-11/3$ power law is observed on all spatial scales, for the von Kármán, this breaks down at low spatial frequencies due to the outer-scale. The modified von Kármán also accounts for the inner-scale at high spatial frequencies.

2.1.1.2 Spatial Power Spectra

Tatarski et al. (1961) showed that one can derive the power spectrum of the refractive index variations. It is expressed as a function of the spatial wave number κ, where

$$\kappa = \frac{2\pi}{l} \tag{2.5}$$

and l is the scale size of the fluctuations. The 3-dimensional power spectrum is given by

$$\Phi_N^K(\kappa) = 0.033C_N^2\kappa^{-11/3} \tag{2.6}$$

This is referred to as the Kolmogorov power spectrum, and is only valid for spatial separations which are greater than the inner-scale but less than the outer-scale. Other models for the power spectra exist which account for these quantities, most commonly the von Kármán spectrum and modified von Kármán spectrum are used. The former accounts for the outer-scale, and the latter for both the inner and outer-scales (Von Kármán, 1948).

The von Kármán spectrum is given by

$$\Phi_N^{VK}(\kappa) = \frac{0.033C_N^2}{(\kappa^2+\kappa_0^2)^{11/6}} \tag{2.7}$$

and the modified von Kármán spectrum by

$$\Phi_N^{mvK}(\kappa) = 0.033 C_N^2 \frac{\exp(-\kappa^2/\kappa_m^2)}{(\kappa^2+\kappa_0^2)^{11/6}} \tag{2.8}$$

where $k_m = 5.92/l_0$ and $k_0 = 2\pi/L_0$ (Schmidt, 2010). l_0 and L_0 represent the inner and outer scales respectively. It is interesting to note that as $L_0 \to \infty$ and $l_0 \to 0$, both Eq. (2.7) and Eq. (2.8) collapse to the Kolmogorov power spectrum, Eq. (2.6). All three spectra are plotted in Fig. 2.1. Values of l_0 have been measured to range from 1 mm to 10 mm (Roddier, 1981). L_0 is a more difficult parameter to ascertain. It is likely that it varies greatly and has been measured to range from 10 m (Consortini et al., 2002) to 50 m (Rigaut et al., 1991) and even up to 300 m (Agabi et al., 1995).

2.1.2 Imaging Through the Atmosphere

When considering the effects of the atmosphere on imaging, the wavefront perturbation caused by the refractive index variations must be determined. The deformation of the wavefront surface is given by the sum of the optical path variations,

$$\delta = \int n(z)dz \tag{2.9}$$

where z is the optical path length in the direction of light propagation. Note that this expression is wavelength independent, hence the deformation of a surface required to correct for wavefront deviation is the same for all wavelengths, though atmospheric dispersion effects may become apparent at low visible wavelengths. This allows AO systems to measure the wavefront error at a single wavelength band yet provide correction across the entire spectrum.

The wavefront phase variation is given by

$$\phi = k \int n(z)dz \tag{2.10}$$

where k is the wavenumber of the light, and is given as

$$k = \frac{2\pi}{\lambda} \tag{2.11}$$

Eq. (2.10) shows that the phase deviation is dependent on the wavelength of the light, longer wavelength light will be less degraded by the turbulence than that at short wavelengths.

Similarly to refractive index fluctuations, a phase structure function can also be expressed.

$$D_\phi(r) = \langle|\phi(x) - \phi(x+r)|^2\rangle \tag{2.12}$$

Roddier (1999) shows that by combining Eq. (2.4), Eq. (2.10) and Eq. (2.12) and performing the integration one can derive the 2-dimensional structure function

$$D_\phi(r) = 2.91 k^2 r^{5/3} \int C_N^2(z)dz \tag{2.13}$$

and when the zenith angle that a telescope observes, γ, is included,

$$D_\phi(r) = \frac{2.91k^2}{\cos(\gamma)} r^{5/3} \int C_N^2(h)dh \tag{2.14}$$

where h is the height of each turbulence layer.

It is useful to define an intuitive measure of turbulence strength. Fried (1965) defined such a measure, r_0, known as the Fried parameter. The phase structure function can be expressed in terms of r_0,

$$D_\phi(r) = 6.88\Big(\frac{r}{r_0}\Big)^{5/3} \tag{2.15}$$

where

$$r_0 = \left[0.42\frac{k^2}{\cos(\gamma)}\int C_N^2(h)dh\right]^{-3/5} \tag{2.16}$$

The Fried parameter is the diameter of telescope over which turbulent effects begin to seriously limit performance (i.e. a telescope with diameter larger than r_0 actually has an effective resolution similar to that of a telescope with diameter r_0) (Fried, 1966). It also has the property that there is roughly one radian of Root Mean Square (RMS) wavefront error over a patch of turbulence of diameter r_0. The well known Rayleigh criterion states that the resolving power of an imaging system can be expressed as

$$\Delta\theta \approx \frac{\lambda}{D} \tag{2.17}$$

where $\Delta\theta$ is the smallest possible resolvable angle for a system with a circular aperture of diameter D, observing light of wavelength λ (Rayleigh, 1880). For a telescope observing through uncorrected turbulence, if $D > r_0$, then

$$\Delta\theta \approx \frac{\lambda}{r_0} \tag{2.18}$$

and the telescope's resolving power is no longer dependent upon its diameter but the atmospheric conditions.

As the turbulence is not static the effect of its temporal statistical properties must also be considered. Turbulent layers can mostly be approximated as frozen phase screens which move across the telescope line of sight. This is called the Taylor approximation (Taylor, 1938). A parameter describing temporal statistics which is analogous to r_0 can be defined as the time over which one radian of RMS wavefront error will be observed. If r from Eq. (2.15) is expressed as $\tilde{\nu}\tau$, where $\tilde{\nu}$ is a weighted average of the velocities of the turbulent layers and τ is the time between two measurements, then

$$D_\phi(\tau) = \sigma_{time}^2(\tau) = 6.88\Big(\frac{\tilde{\nu}\tau}{r_0}\Big)^{5/3} \tag{2.19}$$

where $\sigma_{time}^2(\tau)$ is the wavefront variance over a time τ. The Greenwood time delay, τ_0 is defined as the time delay when $\sigma_{time}^2(\tau) = 1$ (Greenwood, 1977; Fried, 1990), hence

$$\tau_0 = (6.88)^{-3/5}\frac{r_0}{\tilde{\nu}} = 0.314\frac{r_0}{\tilde{\nu}} \tag{2.20}$$

To properly characterise atmospheric turbulence and design a correction system, both the Fried parameter, r_0 and the Greenwood time delay, τ_0 must be considered. For good observing sites, such as the Roque de los Muchachos Observatory, the median r_0 has been measured to be $\approx 13\,\mathrm{cm}$ and τ_0 to be $\approx 5.58\,\mathrm{ms}$, though these values can vary greatly (Vernin et al., 2011).

2.1.3 Zernike Polynomials

Zernike polynomials, or "modes" are used to describe many optical systems which feature circular apertures (Born and Wolf, 1964). They are are a set of 2-dimensional polynomials defined on a unit circle using polar co-ordinates by

$$\begin{aligned} Z_{even,j} &= \sqrt{n+1}R_n^m(r)\sqrt{2}\cos(m\theta) \\ Z_{odd,j} &= \sqrt{n+1}R_n^m(r)\sqrt{2}\sin(m\theta) \\ Z_j &= \sqrt{n+1}R_n^0(r) \end{aligned} \tag{2.21}$$

where

$$R_n^m(r) = \sum_{s=0}^{(n-m)/2} \frac{(-1)^s(n-s)!}{s![(n+m)/2-s]![(n-m)/2-s]!} r^{n-2m} \tag{2.22}$$

n and m are radial and azimuthal orders respectively, r and θ are polar coordinates and the j value is a numbering system introduced by Noll (1976). Zernike polynomials are orthogonal such that

$$\int d^2r W(r) Z_j Z_{j'} = \delta_{jj'} \tag{2.23}$$

where

$$\begin{aligned} W(r) &= 1/\pi & r &\leq 1 \\ &= 0 & r &> 1 \end{aligned}$$

and $\delta_{jj'}$ is the Kronecker delta function. The first fifteen Zernike Polynomials are illustrated in Fig. 2.2. The first modes represent traditional optical aberrations, such as piston, tip, tilt, focus, astigmatism and spherical aberration.

They are useful in considering atmospheric turbulence as any arbitrary wavefront over a circular aperture can be expressed as a sum of Zernike polynomials. As suggested from the power spectra presented in Fig. 2.1, the lower order spatial modes contain the majority of the power in turbulence induced wavefront error, and the biggest gain in image quality is found from correcting these.

In this thesis there is a strong focus on modes $j = 2$ and $j = 3$, tip and tilt respectively. The effect of these is an overall image motion without any other instantaneous image degradation. If uncorrected they will significantly decrease long exposure resolution as the image will move around during an exposure as the atmospheric turbulence changes. Noll (1976) derived the uncorrected residual wavefront error for a given number of corrected Zernike polynomials radial orders. This is shown for the first twenty radial orders in Fig. 2.3, illustrating the importance of correcting for low-order spatial modes, as these contain the greatest coefficients of wavefront error. Conan et al. (1995) has analysed the temporal power spectra of Zernike polynomials in atmospheric turbulence, determining that these lowest order modes also vary slowest, hence may be corrected with lowest frequency.

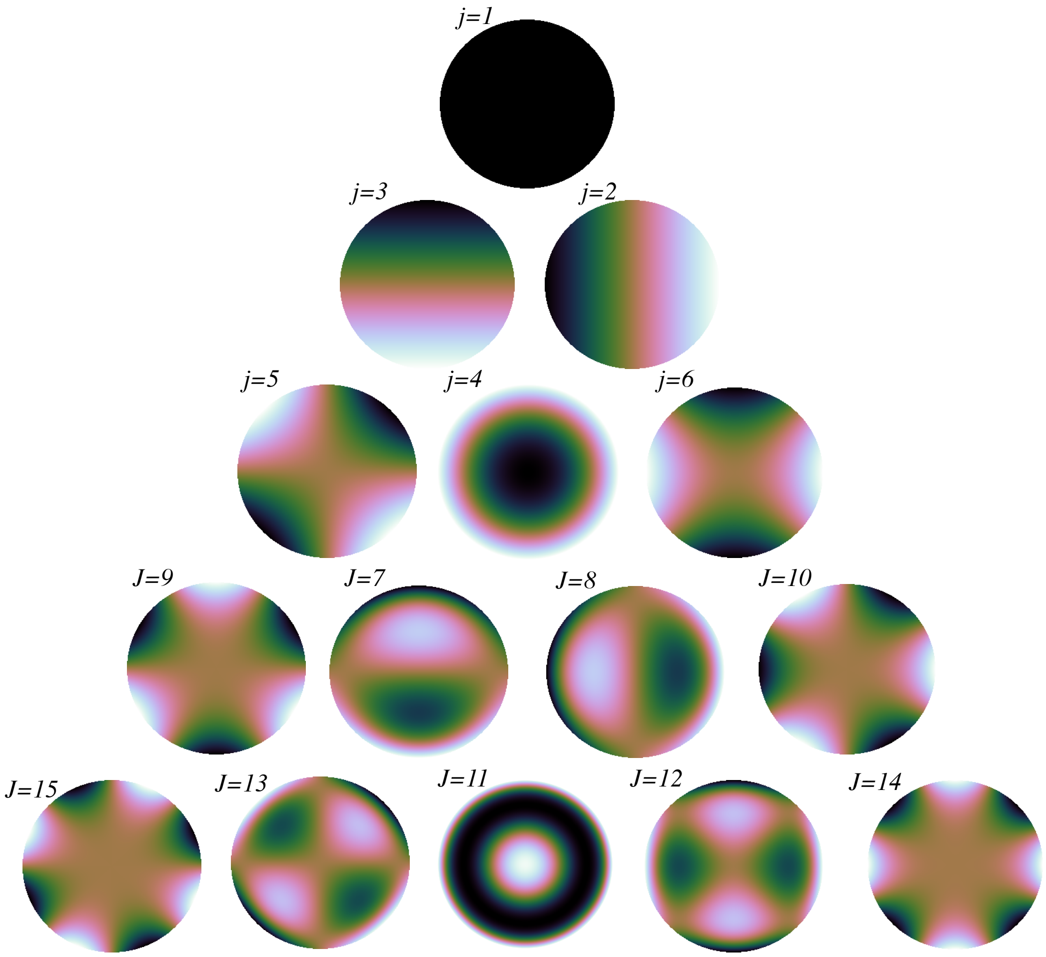

Figure 2.2: The first fifteen Zernike polynomials. The j value is the numbering system introduced by Noll (1976). Any circular image can be expressed as an infinite sum of these orthogonal Zernike polynomials.

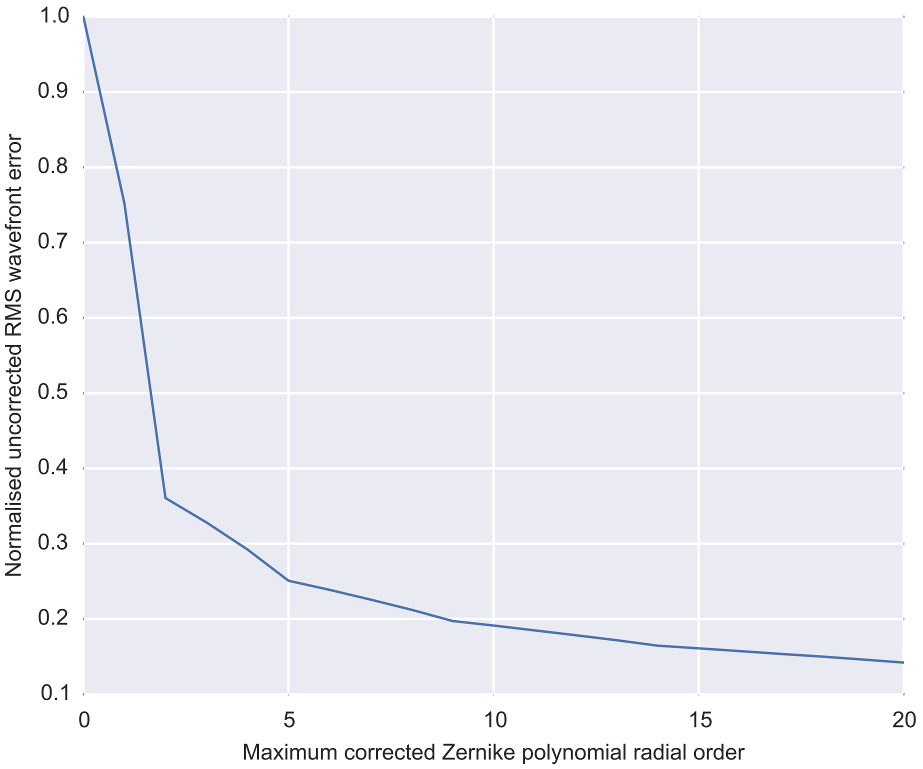

Figure 2.3: The residual uncorrected RMS wavefront error for the number of correction Zernike polynomial radial orders. Correcting the lowest spatial order modes gives the greatest reduction in wavefront error.

2.2 Common Components of Adaptive Optics Systems

Despite the many modes of AO operation, all systems share some common components. All must feature some method of wavefront sensing, a method of correcting for the aberrated wavefront and a Real-Time Control System (RTCS) to transform Wavefront Sensor (WFS) data to Deformable Mirror (DM) commands.

2.2.1 Wavefront Sensors

WFSs are an area of extremely active research within AO and there are a number of different types available, such as the curvature sensor (Roddier and Roddier, 1988) used on many early systems, the pyramid WFS (Ragazzoni, 1996) and the recently proposed YAW (Gendron et al., 2010), each with advantages and drawbacks. The work in this thesis is performed exclusively using Shack-Hartmann (SH) WFSs so discussion here is limited to those alone.

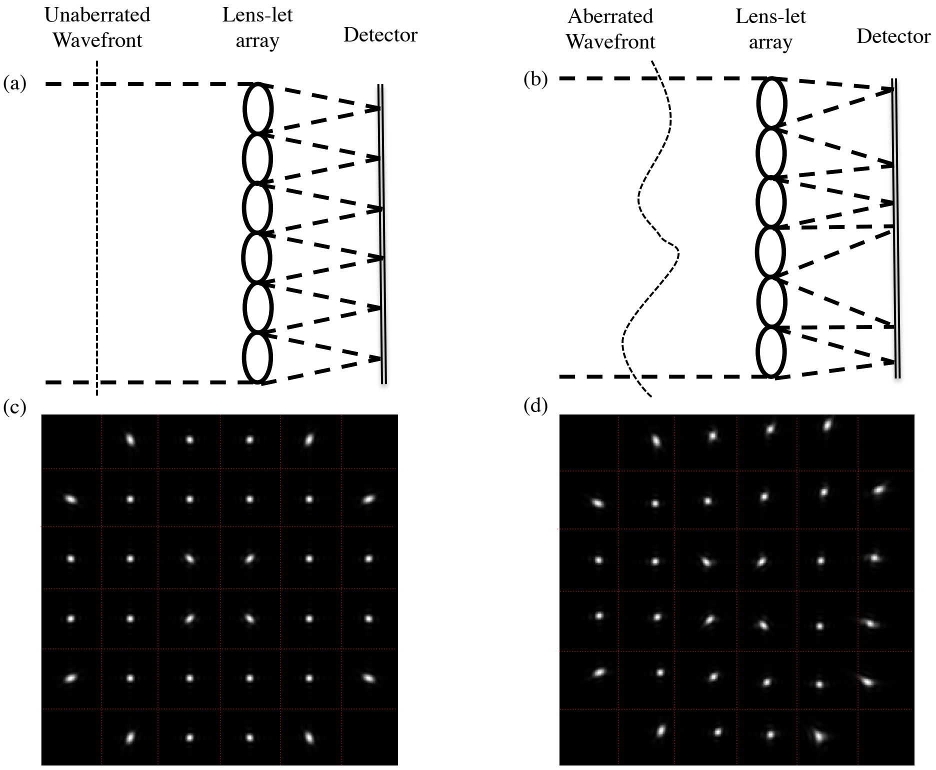

Figure 2.4: An illustration of the Shack-Hartmann WFS. (a) and (c) shows the operation of and the resulting image through an annular aperture from a SH WFS when exposed to an unaberrated wavefront. Light from each lenslet is undeviated and a regular grid of spots is observed. (b) and (d) show the same for the SH WFS when observing an aberrated wavefront. Light from each lenslet is deviated, and the grid is no longer regular, the deviation of each spot is calculated to take a measurement of the gradient of the wavefront across each sub-aperture. Sub-aperture boundaries are denoted by red dotted lines and the misshapenness of some spots is caused by their partial illumination through an annular aperture.

2.2.1.1 Shack-Hartmann Wavefront Sensor

The most common form of WFS in use in current AO systems is the SH WFS (Hardy, 1998) its operation is illustrated in Fig. 2.4. A lenslet array, an optical element formed from a grid of many small lenses, is placed in a plane optically conjugate to that where maximum wavefront reconstruction sensitivity is required, in many AO systems this is the plane optically conjugate to the telescope pupil. A detector, often a Charged Coupled Device (CCD), is placed at the focal plane of all the lenslets and hence records a grid of spots. The small optical systems formed by each lenslet are referred to as sub-apertures. If no wavefront aberration is present in the incoming light, the spots will all be undeviated and form a regular grid, however, if the wavefront is aberrated the grid will no longer be regular. The deviation of each spot from its central position can be calculated using a centroiding algorithm, producing a measurement of the gradient of the wavefront over that sub-aperture(Platt et al., 2001).

2.2.1.2 Open and Closed Loop Operation

For Single Conjugate Adaptive Optics (SCAO) AO systems the WFSs will be “closed loop” on the DMs, that is, they only ever observe a corrected wavefront. For a SH WFS, this means that the spots should only move a relatively small distance. A SH WFS operating in such conditions does not require a large field of view or number of detector pixels per sub-aperture to stay in a linear and sensitive regime.

In contrast, some of the tomographic modes of AO described in § 2.4 require that the WFSs do not observe any correction, hence are “open loop” on the DMs. This mode of operation provides challenges for the design of an appropriate SH WFS. The spots can no longer be relied upon to stay close to the centre of each sub-aperture so the WFS must feature a greater field of view per sub-aperture. In order that the sub-aperture maintains a linear response across the majority of the field of view more pixels are required. More pixels across a sub-aperture increases the read and photon noise for a given light flux so effectively reduces the WFS Signal to Noise Ratio (SNR).

2.2.2 Deformable Mirrors

The DM is responsible for correcting the aberrated wavefront and ultimately removing the optical aberrations. Though other technologies such as spatial light modulators are available to alter the phase of light, none are as light efficient or as responsive as a DM. Most DMs consist of a polished surface from which the light will be reflected, and a system of some actuators behind the surface to push or pull it into the required shape. The shapes that are formed on the mirror surface by an activation of each individual actuator are known as the “influence functions” of the DM (Pearson and Hansen, 1977).

The DM characteristics depend greatly on the actuator technology. If piezo-electric actuators are used then hysteresis, where the actuator does not take the same position for an identical command, must be considered. Piezo electric actuators cannot usually be stacked densely so for high-order DMs the mirrors become very large. Micro-Electro-Mechanical System (MEMS) DMs on the other hand use electrostatic actuators, which are fabricated using a similar method to computer microchips (Perreault et al., 2002), can be stacked very densely. Boston Micromachines for example, offer a 64×64 actuator DM within a 25 mm aperture. However, MEMS DMs have a relatively small stroke so can only be used to remove high order aberrations once low-order modes have been removed by a different DM technology.

Finally, a new class of adaptive secondary DM have recently become popular. This is a replacement to the telescope’s secondary mirror and is operated by voice-coil actuators. They feature very large stroke and can contain a large number of actuators due to their relatively large diameter but entail a large degree of planning as they are integrated into the telescope and are expensive due to their large size (Madec, 2012).

2.2.3 Wavefront Reconstructors

The AO “reconstructor” describes the algorithm which converts measured WFS data to commands to be sent to the DM. Obviously correction performance is hugely dependent on the implementation of this reconstructor.

The simplest reconstruction method is to measure and invert the system "interaction matrix". This matrix describes the change in WFS measurements for a known activation of each DM actuator and is obtained during system calibration. The interaction matrix can be expressed algebraically,

$$\tilde{\mathbf{s}} = \hat{\mathbf{M}}_{\mathbf{i}}\tilde{\mathbf{d}} \tag{2.24}$$

where $\tilde{\mathbf{s}}$ is a vector of all WFS measurements, $\tilde{\mathbf{d}}$ is a vector of all DM actuator commands, and $\hat{\mathbf{M}}_{\mathbf{i}}$ is the interaction matrix which relates the two and is of size (number of WFS measurements, number of DM actuators).

Once the interaction matrix has been obtained, it is necessary to invert it so that an estimate of the required DM commands can be computed to correct for a wavefront observed by the WFS, hence,

$$\tilde{\mathbf{d}}_{\mathbf{est}} = \hat{\mathbf{W}}\tilde{\mathbf{s}} \tag{2.25}$$

where $\hat{\mathbf{W}}$ is the reconstruction, or "command" matrix and $\hat{\mathbf{W}}\hat{\mathbf{M}}_{\mathbf{i}} = \hat{\mathbf{I}}$, the identity matrix. The command matrix will be of size (number of DM actuators, number of WFS measurements). During AO operation this command matrix can be applied to a vector of WFS measurements from each WFS integration as a Matrix Vector Multiplication (MVM) operation. The result can then be applied directly to the DM to correct the wavefront.

As the interaction matrix will generally not be square a pseudo-inversion method must be used. It is possible that the DM can form shapes which the WFS senses poorly such as so-called "waffle" modes. If left unmitigated these can adversely affect the AO performance by adding unseen wavefront error to the optical path. They are eliminated by setting small singular values to zero after performing a Singular Value Decomposition when inverting the matrix. The advantage of the interaction matrix approach is that all misalignments, rotations and offsets in the system are encoded within the interaction and subsequent control matrices as well as measuring the DM actuator influence functions.

For very high spatial order systems with many WFS measurements and DM actuators, the MVM operation can be too computationally expensive to complete at the required, very high, system update rates of >1 kHz. To perform the reconstruction faster other algorithms have been developed such as the Cumulative Reconstructor (CURE) (Rosensteiner, 2011), or Fourier transform based methods (Poyneer et al., 2002). These algorithms can reconstruct the wavefront faster than a MVM for large systems but as they may not use the interaction matrix they do not always account for the system alignment, hence the AO system must be very well aligned, calibrated and characterised before they are effective.

2.3 Adaptive Optics Theory

2.3.1 Point Spread Function

It is difficult to assess the AO correction performance from an extended object as the intensity distribution observed on the detector is a product of both the object shape, the telescope's Optical Transfer Function (OTF) and the AO system's correction characteristics. The Point Spread Function (PSF) is the intensity distribution observed on the detector

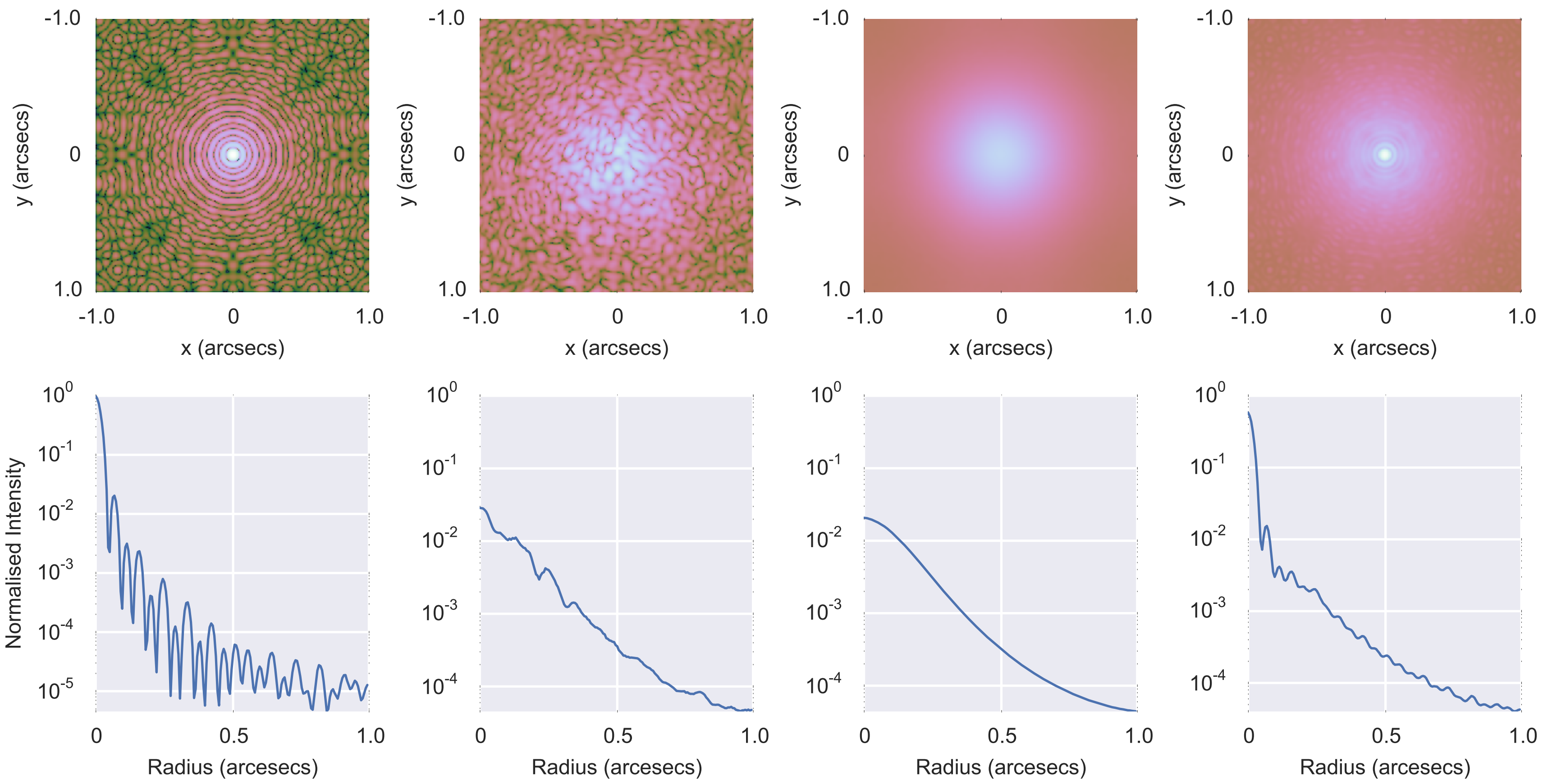

Figure 2.5: Simulated PSFs, from left to right, in the case of no aberration, an instantaneous image through atmospheric turbulence, a long exposure image through atmospheric turbulence, and an AO corrected PSF. In each case a plot of the azimuthally averaged PSF is also presented below. Logarithmic scales are used for both colour scaling in the PSF images, and the intensity axis of the azimuthal averages. All values are normalised to the maximum value of the unaberrated PSF. Artifacts in the PSF images are a result of the finite spatial sampling when performing a FFT.

when imaging a point source and is only dependent on the optical system. In practice, an object much smaller than the theoretical resolution of the imaging system can be considered as a point source. When the optical system is actually used to observe an extended object, the final intensity distribution on the detector is a convolution of the object shape and the PSF of the optical system (Hecht, 1998).

The PSF contains information required to characterise the optical system. The OTF, and hence its absolute value, the Modulation Transfer Function (MTF) can be derived from the Fourier transfer of the PSF, and the optical resolution of the system can be computed. An example of some simulated PSFs are given in Fig. 2.5, showing a PSF in the case of no aberration, instantaneous and long exposure PSFs when imaging through turbulence and an AO corrected PSF. The effect of the atmospheric turbulence is clear, creating multiple "speckles" at points of constructive interference due to the deviated rays of light. As these change with the turbulence, they average in the long exposure case, showing a PSF with increased width hence reducing the system's optical resolution. Though the AO system returns the PSF to its original width, note that the peak intensity is still significantly lower than in the unaberrated case. This is due to uncorrected high spatial frequency aberrations causing a "halo" around the PSF, which would require an AO system with higher spatial order to better correct.

2.3.2 Performance Metrics

In order to assess the performance of an AO system it is necessary to define some performance metrics. As different science cases may have very different requirements of an AO system it is not possible to fully express AO performance in a single value. Instead, there are a number of different metrics which can be used.

2.3.2.1 Strehl Ratio

The Strehl ratio (Strehl, 1894, 1902) is commonly used to describe the correction performance of AO systems (Hardy, 1998; Roddier, 1999). It is defined as the ratio of the measured peak intensity of the AO corrected PSF to the perfect peak intensity of the unaberrated PSF, or

$$S = \frac{I_{\mathrm{meas}}}{I_{\mathrm{perfect}}} \tag{2.26}$$

where I_{meas} is the measured peak intensity and I_{perfect} is the unaberrated peak intensity.

In AO simulation it is trivial to generate the perfect PSF peak intensity to use to calculate the corrected PSF strehl ratio. In general though it is difficult to estimate the peak intensity of a perfect, unaberrated PSF, as there will almost always be some aberration or other imperfections present in a real optical system, even with no atmospheric turbulence. The Strehl ratio can be estimated from a known wavefront error. Maréchal (1947) derived an approximation for the relationship between Strehl ratio and wavefront error,

$$S \approx \exp(-\sigma_p^2) \tag{2.27}$$

where $\sigma_p = k\Delta\phi_p$, the incident mean square phase error. This approximation holds true for the case of low wavefront error, less than 1 rad, but begins to break down as the error becomes larger than this. The importance of this relationship is that it allows the prediction of AO imaging performance by considering the sum of the wavefront error contributions from various AO error sources such the fitting error, (§ 2.3.3) temporal error (§ 2.3.4) and angular anisoplanatism (§ 2.3.5). Correspondingly, it also allows an estimate to be made of residual wavefront error from single analysis of the PSF.

2.3.2.2 Full Width at Half Maximum

The Full Width at Half Maximum (FWHM) is a value which can be used to describe the size of the PSF. For applications which do not require the AO system to reach the diffraction limit of the telescope the FWHM can be a useful performance metric. It can be used to calculate the imaging resolution of the AO system and the size which contains a high ratio of the light intensity (Hecht, 1998). The FWHM is a metric which has been well understood by astronomers for many years and so can be used when communicating performance estimates or requirements to non-AO specialists.

However, Fig. 2.5 illustrates why the FWHM is rarely used as a performance metric for AO systems with a very high spatial resolution. The resolution limit of the telescope can be reached with even partial correction, at which point the FWHM reaches a minimum and will decrease no further. In this regime the Strehl ratio is more useful as it can still measure the increase in AO performance after the diffraction limit has been reached.

2.3.2.3 Ensquared Energy

For some applications within astronomy, absolute imaging resolution is not the required metric for assessing the suitability of an AO system. In spectroscopy the instrument requires the maximum flux within the area of each spectrograph spatial pixel, or “spaxel”. In this case a more appropriate performance metric is the so-call “ensquared energy” (sometimes “encircled energy”) (Davies and Kasper, 2012). This is the percentage of the intensity in the PSF which is inside a square (or circular) pixel or spaxel of a given diameter, typically 50-200 mas (Hubin et al., 2005; Andersen et al., 2006; Marchetti et al., 2006; Assémat et al., 2007; Wizinowich et al., 2008). Unlike the Strehl ratio, ensquared energy is a metric that can be taken directly by astronomers to estimate the performance and the end-to-end system SNR through inclusion within instrument models. It is thus a very attractive metric for systems such as integral field spectrographs where spaxel sizes can be larger than the diffraction limit.

The drawback of this approach, rather than measuring Strehl ratio, is that there is no clear analytical expression relating the ensquared energy to the wavefront error making it less useful for predicting performance.

2.3.2.4 Sky Coverage

As is discussed in § 2.3.5, AO systems are currently limited to observing in patches of the sky which contain bright Natural Guide Stars (NGSs) to use for either all WFS information or to provide tip-tilt information for a Laser Guide Star (LGS) AO system. AO corrected "sky coverage" is an expression of the percentage of the sky which features such a NGS and hence is available for correction.

The sky coverage value is hugely dependent upon the particular AO system and the requirements of an AO instrument to fulfill its science cases. The Spectro-Polarimetry High-contrast Exoplanet Research (SPHERE) and Gemini Planet Imager (GPI) instruments mentioned in § 3.2, for instance, require a very bright NGS in order to provide extremely high spatial order correction, with a Strehl ratio of up to 0.9, hence sky coverage is low (Petit et al., 2008). The Advanced Rayleigh Ground Layer Adaptive Optics System (ARGOS) at the Large Binocular Telescope (LBT) on the other hand, feeds an Near Infra-Red (NIR) imager and Multi-Object Spectrograph (MOS) with lesser Strehl ratio requirements of ≈ 0.1. Using a tomographic LGS AO system, this allows the system to observe up to 84 % of the sky (Rabien et al., 2010; Hart et al., 2011).

As noted by Ellerbroek and Tyler (1998), bright stars suitable for use as NGSs are prevalent at low galactic latitudes but less so around the galactic poles. Sky coverage calculations for the Gemini North telescope LGS AO system show that when observing at low galactic latitudes, the sky coverage can reach up to 90 % for a Strehl ratio of 0.5 in H band using a LGS AO system, but only ≈ 50 % at the galactic pole. This study also illustrates the benefit of using a LGS, as with only NGSs, these values are reduced to ≈ 4 % and ≈ 1 % respectively.

2.3.3 Spatial Resolution

The spatial resolution of the AO system is defined primarily by either the number of WFS sub-apertures or the number of DM actuators. In the rest of this analysis it will be assumed that the DM and WFS resolutions are arranged in the "Fried geometry", where the WFS has one less sub-aperture in each dimension than DM actuators in each dimension and each actuator is situated in the vertices between square sub-apertures. Such a configuration is common amongst astronomical AO systems (Flicker et al., 2000; Poyneer et al., 2002; Myers et al., 2008; Bouchez et al., 2009)

Because the spatial resolution cannot be infinite there will always be some "fitting error" as the WFS and DM do not have a high enough fidelity to perfectly fit the shape of the wavefront. Using the the expressions derived in § 2.1.2, the mean square fitting error can be expressed as

$$\sigma_F^2 = a_F \left(\frac{d}{r_0}\right)^{5/3} \tag{2.28}$$

where d is the sub-aperture diameter, r_0 is the Fried parameter and a_F is a fitting parameter corresponding to the DM type used to correct the wavefront. Hardy (1998) gives some examples of a_F for different DM technologies. These range from a value of $1.26\,\mathrm{rad}^2$ for a DM with piston only segments, 0.28-$0.34\,\mathrm{rad}^2$ for continuous phase sheet DMs and $0.14\,\mathrm{rad}^2$ for segmented DMs with three actuators per segment, allowing tip, tilt and piston movement.

The practical spatial resolution of the system is ultimately flux limited. An increased number of sub-apertures decreases the flux availably for each sub-aperture, leading to longer WFS exposure times or a lower SNR. Large numbers of sub-apertures also place an increased strain on the RTCS which requires more powerful computers and faster interfaces to run at the required rate.

2.3.4 Temporal Resolution

As the turbulence in the atmosphere changes the correction must be updated continuously. If τ_0 is known then the temporal error due to a given delay, τ, can be computed by substituting Eq. (2.20) back into Eq. (2.19),

$$\sigma_T^2(\tau) = \left(\frac{\tau}{\tau_0}\right)^{5/3} \tag{2.29}$$

Ideally, τ will be made as small as possible by running the system as quickly as possible. This is limited by the speed that one can take a WFS exposure, read the WFS detector, compute the DM commands and finally apply them to the DM. All of these steps are related to the spatial resolution of the system. When an AO system is being designed, Eq. (2.28) and Eq. (2.29) must be considered along with expected values of r_0, τ_0 and guide star luminosity for the observatory site. This can be applied to the requirements of the system to determine an optimal spatial and temporal resolution.

2.3.5 Angular Anisoplanatism

In general a science target is not bright enough for a WFS to use. In this case one can find a suitably bright "guide star" that is close to the science target and can be used to feed the WFS. This geometry is illustrated in Fig. 2.6.

If the chosen guide star is an astronomical object, it is termed a NGS (in contrast to a LGS introduced in § 2.3.6). If the guide star is very close to the scientific target it is possible to achieve correction at a similar level to that if the science target is used to feed the WFS. As the turbulence in the atmosphere is not all at ground altitude, the AO system will lose corrective performance as the angle between the guide star and the science target increases. This effect is called "angular anisoplanatism", and the area around a guide star for which there is less than 1 radian of wavefront error the "isoplanatic patch". The isoplanatic patch size is a function of the strength of the atmospheric turbulence and its vertical profile, i.e. the heights of the various turbulence layers.

We can derive an expression to analyse angular anisoplanatism by considering the phase structure function, Eq. (2.14). The separation of the NGS and science object meta-pupils at a turbulence layer at height h, is

$$r(z) = \frac{\theta h}{\cos(\gamma)} \tag{2.30}$$

where θ is the angular separation between the NGS and science object, and γ is the zenith angle of the observation. Substituting into Eq. (2.14),

$$\langle \sigma_\theta^2 \rangle = 2.91 \frac{k^2}{\cos(\gamma)^{8/3}} \theta^{5/3} \int_h h^{5/3} C_N^2(h) dh \tag{2.31}$$

The isoplanatic angle over which there is 1 rad of wavefront error can be defined as

$$\theta_0 = [2.91 \frac{k^2}{\cos(\gamma)^{8/3}} \int_h h^{5/3} C_N^2(h) dh]^{-3/5} \tag{2.32}$$

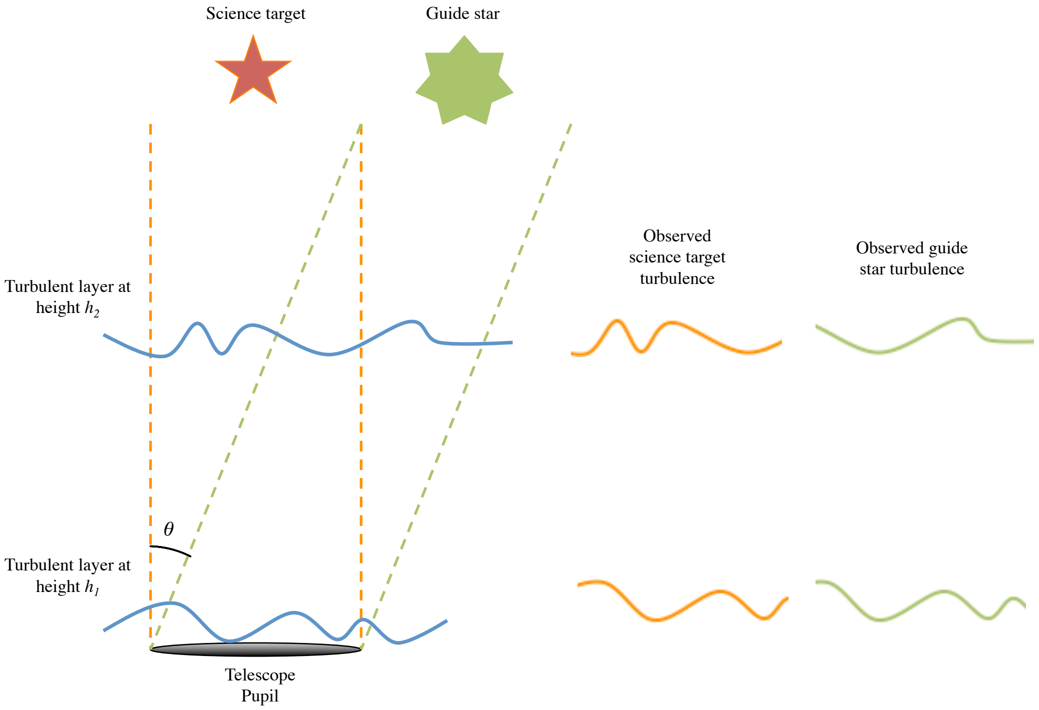

Figure 2.6: Illustration showing the geometry of an AO system where a separate guide star is used for wavefront sensing. As the angle between the guide star and the science target increases, the AO system loses performance. Adequate correction is only possible within the isoplanatic patch size around the guide star. This is clearly dependent on the vertical profile of the turbulence. If high layers dominate the patch will be small as turbulence quickly de-correlates but if turbulence is close to the pupil then correction is possible over much larger angles.

It can also be expressed in terms of r_0 and the atmospheric turbulence weighted average, $\bar{h}$ (Fried, 1982)

$$\theta_0 = 0.314 \frac{r_0 \cos(\gamma)}{\bar{h}} \tag{2.33}$$

where $\bar{h}$ is defined by,

$$\bar{h} = \left(\frac{\mu_{5/3}}{\mu_0}\right)^{3/5} \tag{2.34}$$

and μ is a turbulence moment, defined by

$$\mu_m = \int_0^\infty C_N^2(h) h^m dh \tag{2.35}$$

An expression for wavefront error for a given isoplanatic angle can now be constructed as

$$\sigma_\theta^2(\theta) = (\theta/\theta_0)^{5/3} \tag{2.36}$$

Angular anisoplanatism also implies that there is a limit to the size of science target that can be observed using a single guide star. This effectively limits the field of view for simple

AO systems to the isoplanatic patch size, often only a few arc-seconds (Foy and Labeyrie, 1985). Even across this patch correction will not be uniform and will likely be better near to the guide star and be less effective at the edges of the field.

2.3.6 Laser Guide Stars

2.3.6.1 Laser Guide Star Generation

If a science target of interest is not located within the isoplanatic patch size of a suitably bright guide star it is possible to create an artificial guide star using a laser (Foy and Labeyrie, 1985). The laser is propagated from a small Laser Launch Telescope (LLT) placed either behind the telescope central obscuration (termed “centre-launched”) or at the side of the telescope primary mirror (termed “side-launched”). There are two varieties of laser used to create a LGS.

A Rayleigh LGS is created by propagating a beam into the atmosphere and observing the light back scattered from molecules in the atmosphere (Primmerman et al., 1991; Fugate et al., 1991). This requires that the laser is pulsed and synchronised with a shuttering mechanism in the WFS so that only light at a specified altitude is observed. As the atmospheric air pressure decreases with altitude, the scattered return also decreases. This limits the altitude of Rayleigh LGS to around 20-25 km (Thompson and Castle, 1992).

More commonly, LGSs are created using a sodium laser which is used to excite sodium atoms in the mesospheric sodium layer causing them to emit light (Thompson and Gardner, 1987). This is a layer of sodium atoms formed by meteoric ablation as they burn up in the Earth’s atmosphere. The laser light excites the D_2 line of the sodium atoms to induce radiation at a wavelength of 589 nm that can be used to feed a WFS. The sodium layer exists at an altitude of 90 km above the earth and has a thickness of around 10 km, though both the mean altitude and thickness have been known to fluctuate over timescales of minutes and hours (Pfrommer et al., 2009). This means that a continuous wave sodium LGS cannot be used to detect atmospheric focus aberrations, as the absolute height of the beacon is not known and a NGS must be found to provide this information. If a pulsed sodium laser is paired with a shuttered WFS, then light can be isolated at a known height, in a similar fashion to when using a Rayleigh LGS (Zhang et al., 2014). For the remainder of this thesis this is the assumed mode of sodium LGS operation.

The finite depth of the sodium layer actually creates a plume of light. Sections of the telescope which view this at an angle observe a cigar shaped object rather than a point source as is the case for a NGS. This is detrimental to wavefront sensing, as most WFSs function with the assumption that the guide star is a diffraction limited point source. This effect scales with telescope diameter, so though it is not a major source of error for 8 m class telescopes which may experience elongation up to $\approx 2''$, mitigation is vital to ensure good operation at Extremely Large Telescope (ELT) scales (Schreiber et al., 2009), where elongation will reach $\approx 10''$.

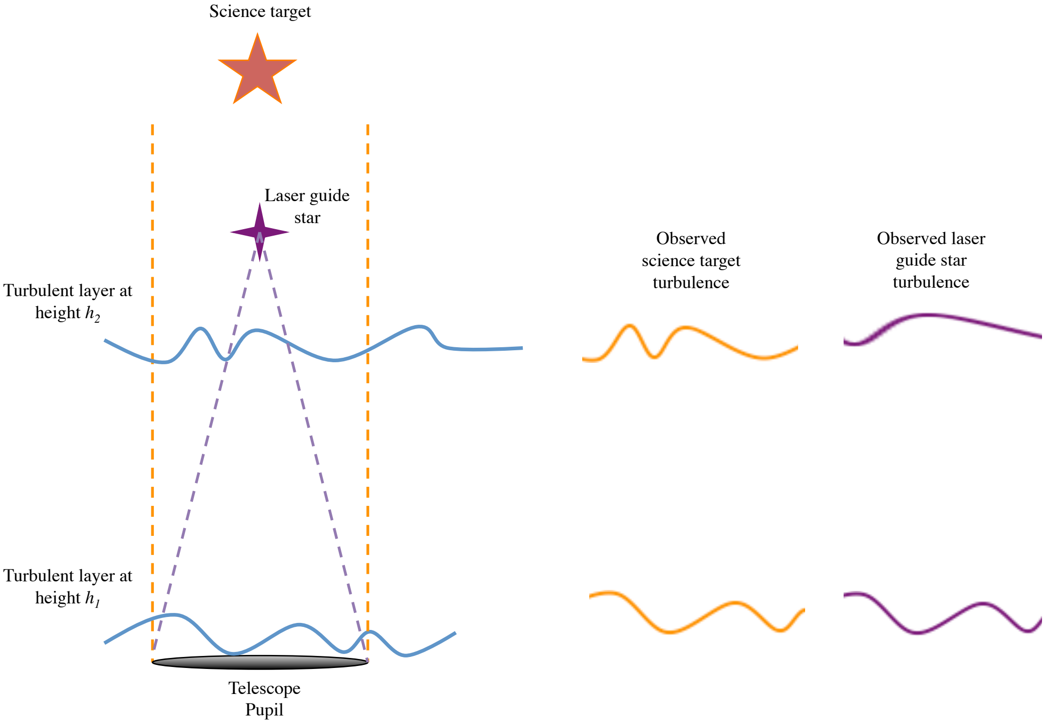

Figure 2.7: An illustration of focus anisoplanatism, or “cone effect”. The light from an LGS travels in a cone, rather than a cylinder as for the science target so they observe different turbulence. As shown, high turbulence layers are responsible for more anisoplanatism.

2.3.6.2 Focus Anisoplanatism

Which ever method is used to create a LGS, it exists at a finite altitude and light travels back to the telescope through a cone. This means that for high altitude turbulence layers, the patch of turbulence observed by the LGS will be different to that observed by the astronomical science target. This is termed focus anisoplanatism, or the “cone effect”, and is illustrated in Fig. 2.7. Fried and Belsher (1994) studied this effect in detail, and derived an expression for the focus anisoplanatic error,

$$\sigma_{FA}^2 = (D/d_0)^{5/3} \tag{2.37}$$

where D is the diameter of the telescope primary collector, and d_0 is a parameter dependant upon the atmospheric turbulence profile, integrated turbulence strength, LGS altitude and wavelength. Hardy (1998) derives

$$d_0 = \left\{ k^2 \left[0.057\mu_0^+(H) + 0.5\frac{\mu_{5/3}^-(H)}{H^{5/3}} - 0.452\frac{\mu_2^-(H)}{H^2} \right] \right\}^{-3/5} \tag{2.38}$$

where H is the altitude of the LGS, k is the wavenumber of the light, and μ_0^+, $\mu_{5/3}^-$ and μ_2^-

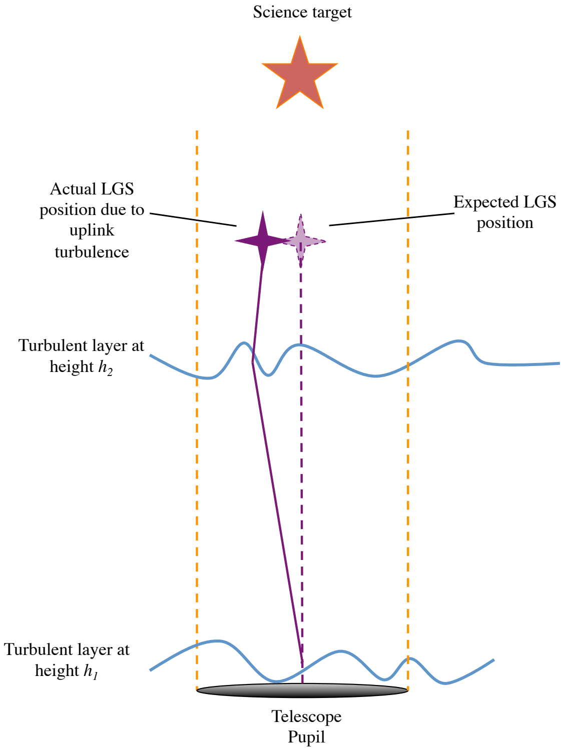

Figure 2.8: An illustration of the effect of LGS uplink turbulence. Due to turbulence the laser beam passes through in its uplink path it deviates making its absolute position in the sky unknown. If it is assumed to be in its expected position above the telescope then spurious tip-tilt correction signals will be sent to the DM.

are partial turbulence moments, defined as

$$\begin{aligned}\mu_m^+ &= \int_H^\infty dz C_N^2(z) z^m \\ \mu_m^- &= \int_0^H dz C_N^2(z) z^m\end{aligned} \qquad (2.39)$$

Eq. 2.37 shows that focus anisoplanatism become more pronounced for larger telescope diameters, so though single sodium laser systems can provide acceptable performance for current telescopes, a single LGS is not adequate for ELT scale systems. Focus anisoplanatism also decreases as the altitude of the LGS increases, hence single Rayleigh LGS are rarely used for facility AO systems on current large telescopes. Focus anisoplanatism can be overcome completely when a tomographic AO system is used with multiple LGSs. Such systems are described in § 2.4.

2.3.6.3 Laser Guide Star Uplink Tip-Tilt Error

The laser must pass up through turbulence as it travels to form a guide star. The laser beam is small so this manifests as the addition of low spatial order "tip" and "tilt" modes, making the guide star jitter in the sky unpredictably, an effect illustrated in Fig. 2.8. A movement of the guide star is observed by the LGS WFS as a tip-tilt aberration present in the atmosphere. If the LGS WFS signals corresponding to tip-tilt are sent to the DM then the wrong correction will be applied, as they are not experienced by the science target. For this reason, all tip-tilt information from a WFS LGS is usually discarded and a NGS must be found to supply it instead.

Thankfully, a tip-tilt sensor is very undemanding in terms of required guide star brightness as it only requires a single sub-aperture and, as mentioned previously in § 2.1.3, atmospheric tip-tilt modes also vary slowest. Consequently, LGSs do provide a gain in terms of sky coverage as they lessen the requirement on the NGS. They do not provide consistent correction across the full sky though, as a suitably luminous tip-tilt NGS is not to be found in certain parts of the sky. It is estimated that current LGS systems can provide diffraction limited correction for up to 90 % of the sky, though this value is significantly lower around the galactic poles where there are few bright stars (Davies and Kasper, 2012).

2.3.6.4 Proposed Mitigation of Laser Guide Star Uplink Effects

One solution to the issues caused by LGS uplink turbulence is to only correct for higher order spatial modes and not correct for tip-tilt at all, using only the telescope's built in guiding system to slowly correct for large tip-tilt offsets. This results in full sky coverage AO correction though the correction performance is low. Such an AO mode has been suggested by Davies et al. (2008), who explain that, despite the low AO performance, it provides greater throughput and resolution than the seeing limited case, so is still of use for some spectrographic applications.

A number of AO schemes have been suggested by Belen'kii (1994, 1995, 2000). These involve using separate LGS beam monitoring telescopes which observe the beam from a different location and feed back position information that is used to calculate the absolute position of the LGS. Due to the large cost overhead of creating extra telescopes solely for LGS AO, it has yet to be implemented. Ragazzoni et al. (1995) has also proposed such an auxiliary telescope and has further proposed methods using auxiliary LGSs launched from positions apart from the main telescope (Ragazzoni, 1996, 1997). Again, these approaches have too large a cost, complexity and effort overhead to truly be considered practical.

More recently, Basden (2014) has proposed correcting with a Laser Tomographic Adaptive Optics (LTAO) system without using a NGS, with science images recorded on a short exposure detector. In this scenario, all modes other than tip and tilt can be corrected and it is accepted that the image will wander on the detector. If the science detector has a short enough exposure time it will return a stack of well corrected images where the image is offset in each. The image can then be reconstructed post exposure by shifting and summing each image in the stack. This method has promise, but also has some downsides. It is unlikely that it could provide correction for spectrographs as the result could not be simply shifted and summed. For imaging, it requires that the science camera must run at short exposure times, typically running at faster than 1 Hz, which would significantly increase the noise on the detector. Finally, there must be enough flux per short exposure science image, which may be composed of many pixels, to perform a centroiding algorithm and shift and add. It is not clear why it would not be more beneficial to simply run a tip tilt WFS, which could have as few as four pixels, fed from otherwise filtered wavelength bands of the science target. For these reasons, it is unlikely that this method will provide acceptable LGS AO correction over the entire sky.

2.4 Tomographic Adaptive Optics

2.4.1 Tomographic Adaptive Optics Modes

The question of increasing the AO corrected field of view has been addressed by tomographic AO configurations including Ground Layer Adaptive Optics (GLAO), Multi-Conjugate Adaptive Optics (MCAO) and Multi-Object Adaptive Optics (MOAO). LTAO is a further tomographic AO configuration developed to mitigate LGS focus anisoplanatism. All of these involve using multiple WFSs observing guide stars in different directions amongst the AO corrected field of view to build a "tomographic" vertical profile of the atmospheric turbulence.

2.4.1.1 Ground Layer Adaptive Optics

In a GLAO system only the ground layer of turbulence is corrected. This is often the greatest contributor to integrated seeing strength, so can give significant gains in performance (Shepherd et al., 2014). It is also common to all observation directions, so provides correction across almost the entire field of view of the telescope. As no attempt is made to correct for higher turbulence layers AO performance is not as high as when other tomographic AO modes are implemented. The ARGOS for example at the LBT aims for Strehl ratios of only 0.1 (Rabien et al., 2010).

GLAO is a relatively simple tomographic mode to operate as the ground layer is the only optical plane that is common to all WFSs. To correct for it, the common WFS signal must be isolated. In the simplest case by taking the mean of all the WFSs though more complex tomographic algorithms, similar to those for MOAO or MCAO, can be more effective (Van Dam et al., 2013).

Though GLAO does not provide the optimal correction for high spatial resolution applications, it can provide consistent correction over a very large field of view with very high sky coverage (Rigaut, 2002; Tokovinin, 2004).

2.4.1.2 Multi-Conjugate Adaptive Optics

MCAO aims to provide an astronomical instrument with a large continuous AO corrected field of view by splitting the required correction onto multiple DMs, where each DM corrects for turbulence at a certain height (Beckers, 1989; Johnston and Welsh, 1991). As is shown in Fig. 2.9, a larger section of high layer turbulence is corrected, so the corrected field of view of the instrument is considerably increased. MCAO has been tested on sky using the Multi-conjugate Adaptive optics Demonstrator (MAD) system (Marchetti et al., 2003), and the first facility system, the Gemini Multi-Conjugate Adaptive Optics System (GeMS), has recently been commissioned (Rigaut et al., 2012).

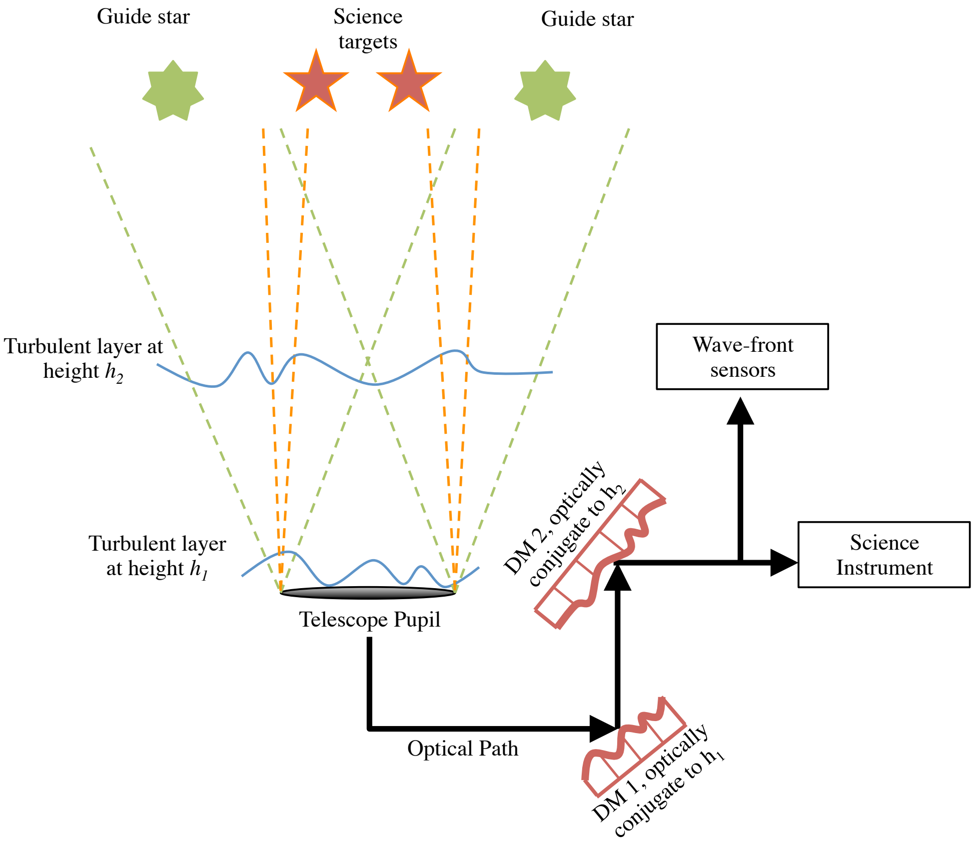

Figure 2.9: A schematic diagram of an MCAO system. Multiple DMs are used, where each DM is optical conjugate to different heights, utilising information from multiple WFSs. This corrects for a larger continuous field of view.

2.4.1.3 Multi-Object Adaptive Optics

MOAO uses the tomographic information in a different manner and instead of providing one continuously corrected field of view, corrects for a finite number of individual lines of sight within a large “field of regard”. Multiple WFSs again provide a tomographic reconstruction of the atmosphere above the telescope, then separate scientific targets are picked off individually. The optimum correction for each science direction is calculated from the WFSs data and a different DM is used to perform correction for each line of sight to each science target. As the DMs do not seek to minimise the wavefront error in the direction of the WFSs, but in multiple science directions, they must be open loop with respect to the WFSs.

This increases the complexity of the system as a simple interaction matrix based reconstructor which accounts for system misalignments as component positions, such as that described in § 2.2.3, cannot be used. Instead, the system must be very accurately characterised and calibrated to ensure optimal performance and complex reconstructors must be used. To perform this calibration, it has been proposed that a “truth” WFS is available to be placed in each science direction, before being removed for a science exposure.

MOAO hugely increases observing efficiency over SCAO by enabling the observation of

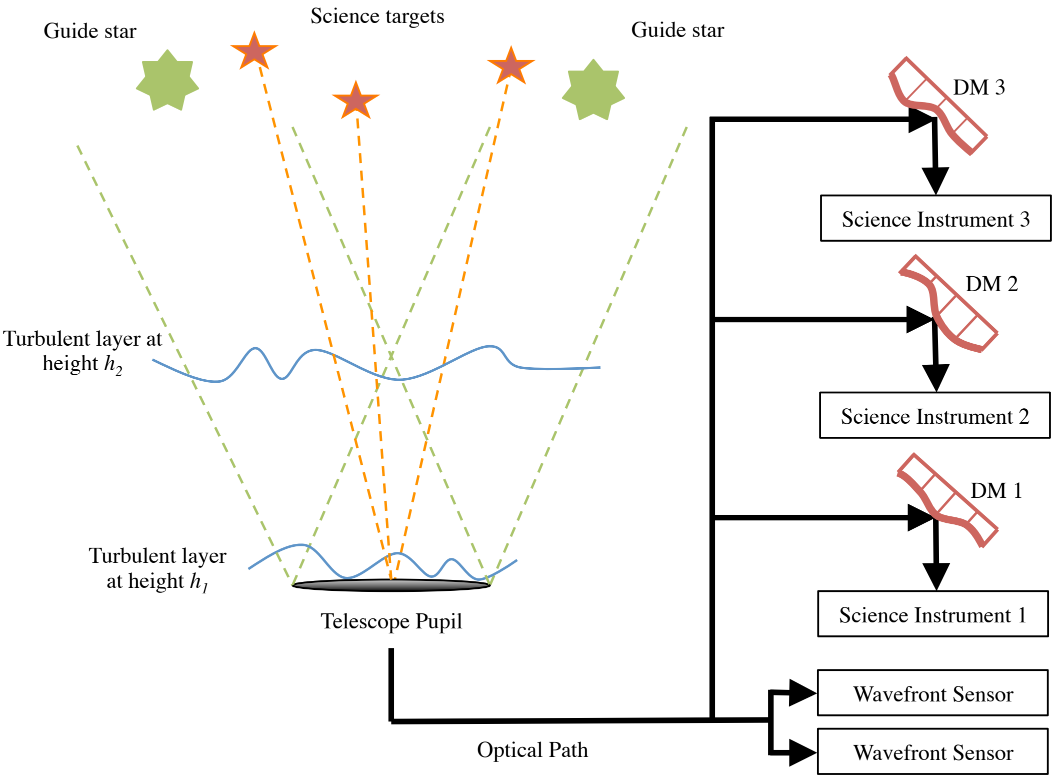

Figure 2.10: A diagram showing the configuration of an MOAO system. Multiple "open-loop" WFS observe directions amongst the desired field. This information is used to simultaneously correct individual science targets which are picked off optically. For clarity only the central light path to the science targets is shown.

multiple targets in one instrument exposure. It also increases the corrected sky-coverage compared to SCAO by allowing correction where there are multiple NGSs far from the science targets, rather than requiring a single one close by. MOAO is the mode of operation of the multi-object integral field spectrograph instrument for the European Extremely Large Telescope (E-ELT) (Cuby et al., 2010), and has been demonstrated on the CANARY demonstrator, hosted by the William Herschel Telescope (WHT) (Gendron et al., 2011). Fig. 2.10 demonstrates the optical setup for MOAO.

2.4.1.4 Laser Tomographic Adaptive Optics

LTAO is illustrated in Fig. 2.11, it is a mode of AO similar to MOAO, where multiple LGSs are used as guide stars, though usually only one direction is corrected for (Hart, 2010). This allows the WFSs to be again placed closed loop of the DM, with all the advantages of ease of calibration and increased WFS centroiding performance that this entails. "Pseudo open loop" measurements are still required, constructed using knowledge of the shape of the DM at any system iteration, to correct tomographically in a direction other than those of the

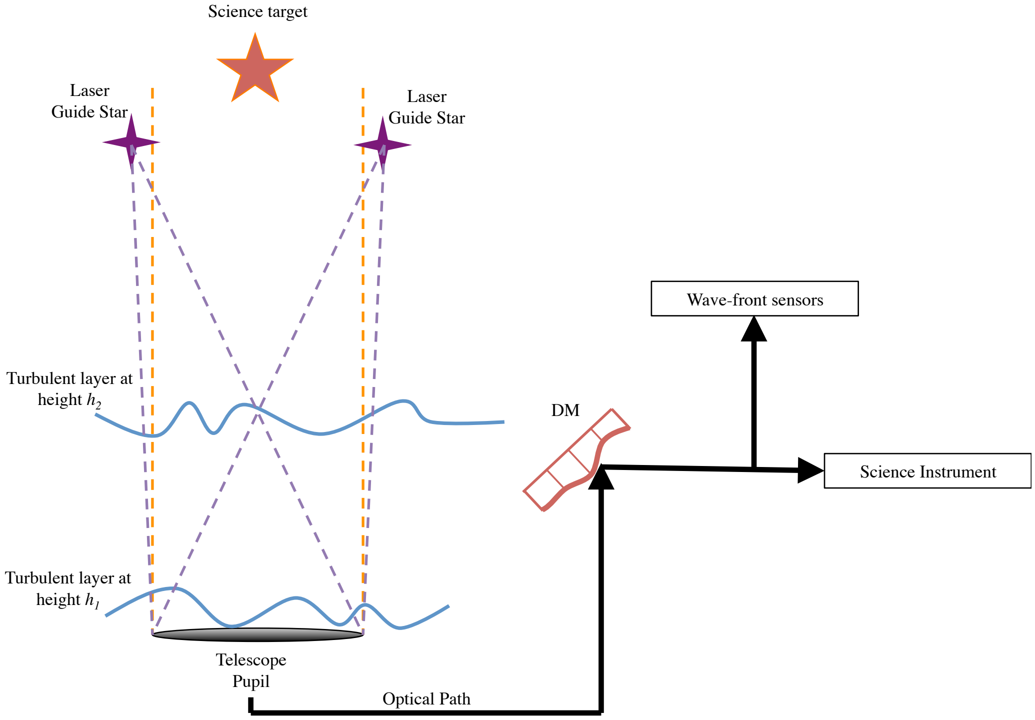

Figure 2.11: An illustration of an LTAO system. Multiple LGS are used, forming an asterism around the target science object. By combining the WFS information from the overlapping cones of turbulence observed by the WFS, Focus anisoplanatism is mitigated.

WFSs.

The use of multiple LGSs compensates for the the effects of focus anisoplanatism as the overlap of observed turbulence provide the entire cylinder observed by the science target. This improves performance of LGS AO systems and will be vital for ELT scale observatories as the cone effect becomes greater as telescope diameter increases.

2.4.2 Tomographic Adaptive Optics Reconstruction

2.4.2.1 Tomographic wavefront reconstruction

A tomographic reconstructor is one which accounts for the vertical C_N^2 profile of atmospheric turbulence in order to provide either improved sky coverage, corrected field of view, or performance compared to an equivalent SCAO system. This is achieved by accepting measurements from multiple WFSs observing in various directions and converting them to DM commands to correct in the direction of one or more science targets (Ragazzoni et al., 2000). A number of methods have been proposed for this purpose and all account for the vertical profile of the turbulence either explicitly, by recovering the phase at each layer, or implicitly, by creating a matrix which contains that information. This is possible by considering the different overlap of WFS meta-pupils, and hence sub-apertures, when projected to different altitudes, as demonstrated in Fig. 2.12. The meta-pupil describes the footprint of

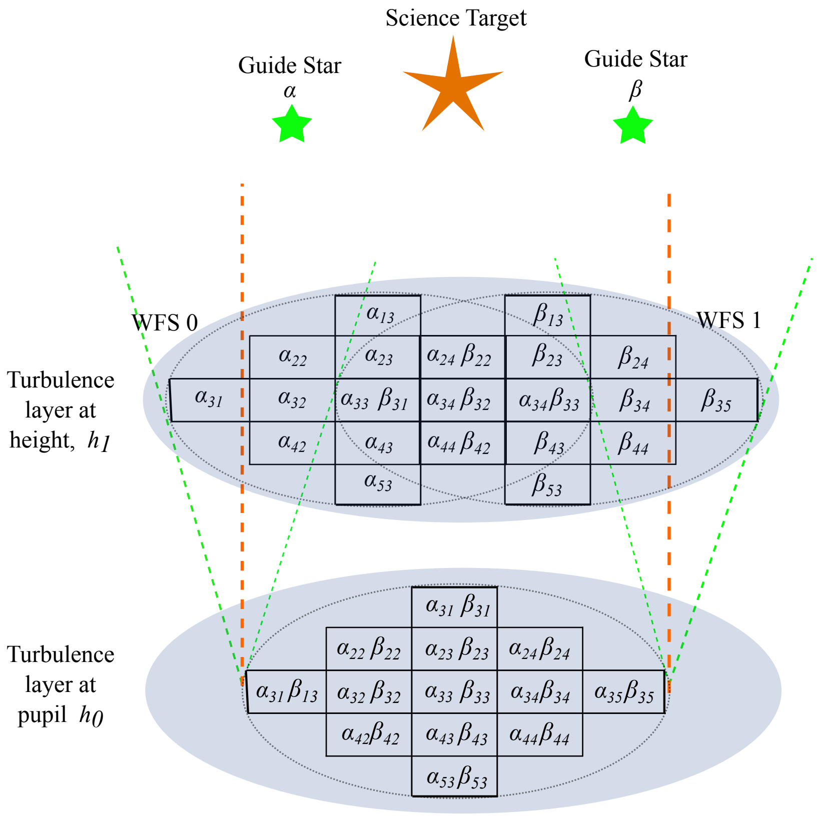

Figure 2.12: A simple demonstration of overlapping WFS meta-pupils at different altitudes, allowing tomographic wavefront reconstruction. At the telescope pupil, sub-apertures $\alpha_{i,j}$ from WFS α, overlap with their counterparts, $\beta_{i,j}$ from WFS β. At a turbulence layer at height h_1, sub-aperture $\alpha_{i,j}$ now overlaps with sub-aperture $\beta_{i-2,j}$. If the guide star observation directions are known, then this allows the profile to be determined through analysis of the two sets of WFS measurements.

a projected telescope pupil to an altitude, accounting for the direction of observation (and cone effect if the guide star is a laser). Methods of tomographic reconstruction have been suggested by Ragazzoni et al. (1999); Tokovinin et al. (2001); Gavel (2004); Neichel et al. (2009); Osborn et al. (2012) and Rosensteiner and Ramlau (2013), but in this work only the Learn and Apply method, proposed by Vidal et al. (2010), has been utilised.

2.4.2.2 Learn and Apply

The following analysis is the same as that undertaken by Vidal et al. (2010). Learn and Apply begins with the proposition that there is a linear relationship between the measurements taken from WFSs distributed around an astronomical science target and the required measurements which would have been recorded if a WFS was observing the target. A matrix can therefore be defined that converts these off-axis WFS measurements to a set of on-axis

WFS measurements. DM commands can then be calculated to correct for that direction using a conventional reconstructor.

If a specific set of measurements taken from a theoretical WFS observing on-axis in the direction of the science target is denoted as $\hat{M}_{\text{on}}$, and those taken from WFSs observing in directions off-axis from the science target as $\hat{M}_{\text{off}}$, then the measurements can be related using a matrix, $\hat{W}$, where

$$\hat{M}_{\text{on}} = \hat{W}\hat{M}_{\text{off}} \tag{2.40}$$

$\hat{M}_{\text{off}}$ has the dimensions of [number of off-axis measurements, number of WFS measurement iterations] and is rectangular so in general it cannot be directly inverted. The matrix $\hat{W}$ can instead be obtained by minimising ϵ^2, where ϵ^2 is

$$\epsilon^2 = ||\hat{W}\hat{M}_{\text{off}} - \hat{M}_{\text{on}}||^2 \tag{2.41}$$

by differentiating and minimising one obtains,

$$\hat{W} = (\hat{M}_{\text{on}}\hat{M}^t_{\text{off}})(\hat{M}_{\text{off}}\hat{M}^t_{\text{off}})^{-1} \tag{2.42}$$

This form of $\hat{W}$ will only be valid for the measurements taken in $\hat{M}_{\text{off}}$ and $\hat{M}_{\text{on}}$. However, as the number of iterations taken to form $\hat{M}_{\text{off}}$ and $\hat{M}_{\text{on}}$ tend towards infinity, the matrices $(\hat{M}_{\text{on}}\hat{M}^t_{\text{off}})$ and $(\hat{M}_{\text{off}}\hat{M}^t_{\text{off}})$ tend towards the covariance matrices of on and off-axis slopes and off and off-axis slopes, $\hat{C}_{\text{onoff}}$ and $\hat{C}_{\text{offoff}}$, respectively. In this case a general tomographic reconstructor, $\hat{W}_{\text{tomo}}$, relating off-axis measurements to those on-axis can be written as

$$\hat{W}_{\text{tomo}} = \hat{C}_{\text{onoff}}\hat{C}^{-1}_{\text{offoff}} \tag{2.43}$$

It is possible to construct these matrices from a knowledge of atmospheric turbulence statistics, the vertical turbulence profile and the relative positions of each of the WFSs. Vidal et al. (2010) explore the idea of making the reconstructor purely analytically, where the turbulence parameters such as r_0 and the vertical turbulence profile are obtained from an external profiling instrument but ultimately conclude that in practice it would not be sufficient.

The MOAO WFSs are open loop on the DM and so do not observe the wavefront correction. Because of this, the registration between the DM and WFS, usually accounted for in the system interaction matrix, will be unknown and any misalignments, rotations or static aberrations unaccounted for. It would also require that the positions of the open loop, off-axis WFSs are known perfectly, again not allowing for any misalignments or pointing errors. The profiling instrument used to supply atmospheric parameters would require an altitude resolution greater than that of the tomographic AO system and would also have to measure localised turbulence structure, such as “dome seeing”, around the AO corrected telescope.

Vidal et al. (2010) instead propose that a “truth” WFS be placed closed loop of each DM to calibrate the system. In a calibration stage, termed the “learn”, the system interaction matrix is recorded using the truth WFS, then WFS measurements taken using all off-axis WFSs and if the science object is bright enough, the truth WFS. If an infinite number of measurements were taken, then the matrices $\hat{C}_{\text{onoff}}$ and $\hat{C}_{\text{offoff}}$ could be obtained, but clearly

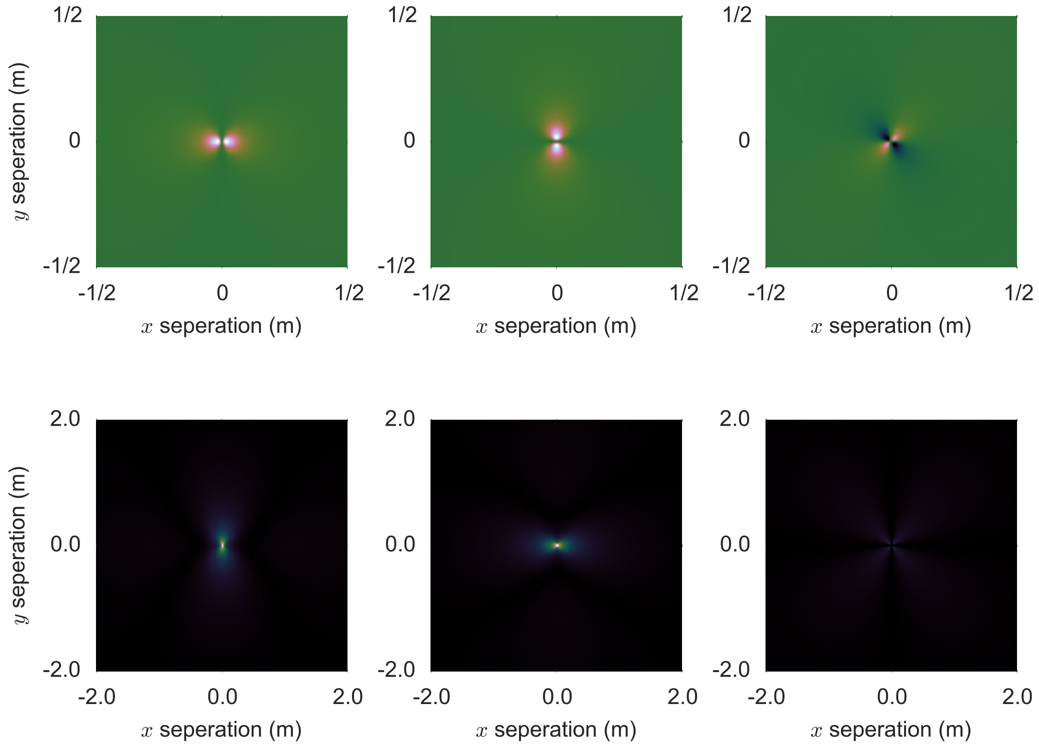

Figure 2.13: Covariance maps in Fourier (top row) and real space (bottom row) for Von Kármán turbulence. From left to right, these show the covariance with spatial separation between wavefront x-gradient and x-gradient, y-gradient and y-gradient, and finally x-gradient and y-gradient. It can be seen that there is a covariance of the slopes even when the separation is not completely zero (i.e., measurements from WFS sub-apertures observing closely separated sections of turbulence will be related). The right most covariance map shows that there is little correlation between x and y slopes at any separation.

this is not possible. Instead, a small number of measurements are taken, over a time of $\approx$ 5-10 minutes, dependant upon the telescope diameter and atmospheric turbulence conditions. These can be used to obtain generalised covariance matrices for the turbulence conditions by minimising

$$\begin{aligned}\epsilon = ||\hat{C}_{\text{onoffraw}} - \sum_{h=0}^{h_{\max}} \hat{C}_{\text{onoff}}(h, r_0(h), L_0(h), (\alpha_i, \beta_i)||^2 \\ + ||\hat{C}_{\text{offoffraw}} - \sum_{h=0}^{h_{\max}} \hat{C}_{\text{offoff}}(h, r_0(h), L_0(h), (\alpha_i, \beta_i)||^2 \quad (2.44)\end{aligned}$$

where $\hat{C}_{\text{onoffraw}}$ and $\hat{C}_{\text{offoffraw}}$ are the measured covariance matrices from the raw data taken from the system calibration. $\sum_{h=0}^{h_{\max}} \hat{C}_{\text{onoff}}(h, r_0(h), L_0(h), (\alpha_i, \beta_i)$ and $\sum_{h=0}^{h_{\max}} \hat{C}_{\text{offoff}}(h, r_0(h), L_0(h), (\alpha_i, \beta_i)$ are theoretical expressions for the covariance matrices,

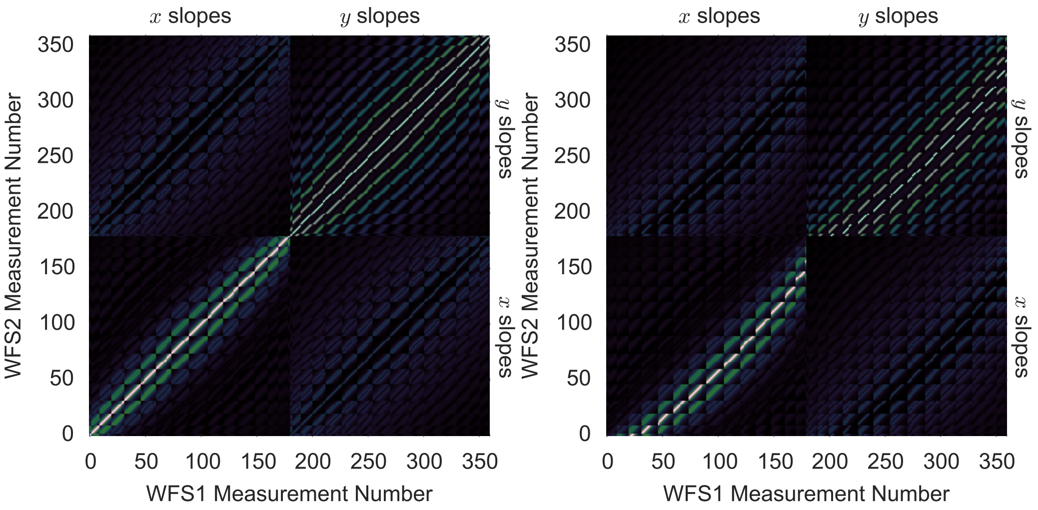

Figure 2.14: Computed covariance matrices between two WFSs. The left hand plot shows the covariance matrix when the WFSs are observing identical turbulence as would be the case when observing only ground layer turbulence. The right hand plot shows the covariance when the sections of turbulence the WFSs observe are separated, in this case by 6 sub-apertures from a 16×16 sub-aperture system. The peak covariance values are off-set for both the x and y slopes. The two gradient directions seem different because of the slope ordering of the WFS measurements when converting from a 2-dimensional image to a 1-dimensional vector of measurements.

expressed as a summation of the covariance matrices from each turbulence layer each with height h, strength, r_0 and outer scale, L_0. They are both also dependant on the position of each WFS, (α_i, β_i). Vidal et al. (2010) suggest the use of a Levenberg–Marquardt fitting algorithm to solve this problem. If the science target is not bright enough for truth sensor measurements to be recorded, then only $\hat{C}_{\text{offoff}}$ is fitted. $\hat{C}_{\text{offon}}$ can be created analytically using the parameters used to perform the fit.

The resulting covariance matrices contain information regarding the alignment of the system and the atmospheric turbulence profile. The covariance between the two sup-apertures in either the same, or different, WFSs in a system is dependant only on the separation of the patch of turbulence they observe at each turbulent layer. Vidal et al. (2010) compute this in the Fourier domain for the Kolmogorov turbulence power spectra, to produce a "covariance map", which shows the covariance for increasing separation. That approach can be easily extended to include the outer and inner scales by considering the modified Von Kármán spatial power spectra presented in Eq.(2.8). In the Fourier domain this is expressed as

$$\mathcal{F}(\langle s_x s'_x \rangle) \propto r_0^{(-5/3)} \xi_x^2 \exp(-|\tilde{\xi}|^2 l_0^2)(|\tilde{\xi}|^2 + 2\pi L_0^{-2})^{-11/6} \times \Pi(\tilde{\xi}) \tag{2.45}$$

where $\langle s_x s'_x \rangle$ is the covariance between two sub-aperture x-gradient slopes, ξ_x is the conjugate variable of the separation in x the position the field, $\tilde{\xi}$ the conjugate variable of the separation vector and $\Pi(\tilde{\xi})$, an expression describing the pupil function in Fourier space. The values r_0, L_0, and l_0 are the statistical parameters describing the turbulence Fried parameter, outer and inner scales respectively. An expression for y-gradient slopes is found by replacing ξ_x with ξ_y, the conjugate variable of y separation.

The covariance map in real space can be computed by taking the inverse Fourier transform of a computed Fourier space covariance map, an example is shown in Fig. 2.13. The analytical forms of the covariance matrices can be computed using the geometry of the WFSs and the covariance map computed for the relevant turbulence parameters. The wavefront deviation resulting from each turbulence layer is independent, hence the final computed covariance matrix is the sum of the covariance matrices for each turbulence layer altitude. Two example covariance matrices are illustrated in Fig. 2.14 showing those between two WFSs observing a single turbulence layer at the ground altitude and at a higher altitude.

2.5 Summary

In this chapter the theoretical considerations vital to understand the subsequent work in this thesis have been explained. This includes a statistical description of atmospheric turbulence and the impact of this on astronomical imaging. WFSs, DMs and reconstructors, common to all AO systems, are discussed before the atmospheric statistical theory is applied to derive the limitations and sources of error within AO systems.

LGSs are considered and the problems created by uplink turbulence for LGSs are described. To account for the uplink tip-tilt, tomographic AO a tomographic AO system will be required. Finally, the Learn and Apply algorithm, which will be used to correct for uplink tip-tilt, has been outlined.

Chapter 3

Current Adaptive Optics System Review

3.1 Introduction

Since Adaptive Optics (AO) was first introduced in the early 1990s there has been a rush to equip the leading observatories with the most advanced AO systems. It is useful to have a knowledge of the current state of the art technologies. In this chapter many of those AO systems are introduced and a particular focus is given to systems which use multiple Laser Guide Stars (LGSs) to perform tomographic correction.

3.2 Natural Guide Star Adaptive Optics Systems

Single Natural Guide Star (NGS) AO systems were the first to be put in to facility use. Table 3.2 details a selection of those systems, all of which are Single Conjugate Adaptive Optics (SCAO) systems using a single Wavefront Sensor (WFS) to observe a NGS.

After early AO systems such as COME-ON (Rousset et al., 1990) and MARTINI (Doel et al., 1991) had proven the potential for astronomical AO, large observatories were quick to begin the design of facility AO systems. The Keck telescopes were the first of the 8 m class observatories to be equipped with AO (Wizinowich et al., 2000a,b), though others such as Subaru, Gemini and the Very Large Telescope (VLT) were not far behind. Shack-Hartmann (SH) WFS technology became dominant, though some systems utilise curvature WFSs.

The Altitude Conjugate Adaptive Optics for the Infra-red (ALTAIR) system for the Gemini North 8 m telescope is an interesting case study. Early results from atmospheric site testing studies had suggested that the majority of turbulence above the telescope site was at an altitude of 6.5 km (Herriot et al., 2000). In order to maximise the isoplanatic patch size the primary deformable mirror was optically conjugated to this altitude also. After the installation of the system, it became apparent that this configuration was sub-optimal and in fact the main contributions to wavefront error were a dominant turbulence layer found at 3.5 km above sea level, the height of the telescope "ground layer", and seeing caused by the telescope structure (Stoesz et al., 2004). The optical train was later altered such that the

Deformable Mirror (DM) was optically conjugate to the telescope pupil, allowing increased AO performance. Subsequent to this experience, all major non-tomographic AO systems have featured a DM conjugated to the telescope pupil plane.

Recently, attention has turned from creating general purpose, multi-instrument NGS AO systems, to creating very high spatial order Extreme Adaptive Optics (XAO) systems. These are often designed for exoplanet studies where very high Strehl ratios are required. Palm 3000, SPHERE Adaptive Optics for eXoplanet Observation (SAXO) and the Gemini Planet Imager (GPI) are examples of such systems, all with greater than 40 sub-apertures across the telescope pupil. These systems are limited to using a bright NGS with magnitude < 9 for optimal performance. This is acceptable as they are intended to observe exoplanets which orbit bright stars so will have access to a bright NGS (Petit et al., 2008).

3.3 Laser Guide Star Adaptive Optics Systems

A number of facilities now also use LGS AO to increase the corrected sky coverage. LGSs are not as common as NGS only systems as they entail significant extra cost in equipment and in overheads as a dedicated laser operator must be employed. For major observatories though, the increased potential in scientific output due to increased AO corrected sky-coverage is well worth the cost. Current prominent LGS AO systems are listed in Table 3.3.

The Keck observatories were again the first of the major observatories to upgrade to LGS AO (Wizinowich et al., 2006), though earlier experiments with a sodium LGS had been performed at the Lick observatory on the 3 m Shane telescope (Max et al., 1997). The decision to mount the laser on the side of the Keck telescope has resulted in significant elongation in the sub-apertures furthest from the launch position, 12 m away. This is complicated by the rotation of the pupil with respect to the LGS WFS, requiring the reconstructor to be continually updated to account for the changing elongation pattern.

RoboAO is a recent, and in many ways exciting, development in the field of LGS AO (Baranec et al., 2012). Though not suitable for large observatories of the 4-10 m class, the entirely automated system can be retro-fitted to many small telescopes to provide correction over much of the sky. A pulsed ultraviolet Rayleigh LGS is used which is less expensive than alternative Sodium LGS schemes.

3.4 Tomographic Adaptive Optics Systems

All the AO systems described thus far have used only a single NGS or a single LGS paired with a low-order tip-tilt-focus NGS sensor. Recently, tomographic AO systems have begun be made available which account for the vertical turbulence profile to provide correction over a larger field of view with greater sky-coverage.

3.4.1 Advanced Rayleigh Ground Layer Adaptive Optics System

The Large Binocular Telescope (LBT) is a telescope with a novel design as it features two 8 m diameter primary mirrors side by side (Hill, 2010). Each of the primary mirrors of the LBT features its own separate AO system, both a high spatial order NGS AO system,

AO System	Telescope (diameter (m))	WFS	DM	First Light	Notes
Keck AO Facility (Wizinowich et al., 2000a,b)	Keck (10)	20×20 Shack-Hartmann	Xinetics 349 actuator	1999	
Cassegrain Adaptive Optics system (Takami et al., 2004)	Subaru (8.2)	36 Avalanche Photo-Diode (APD) sub-aperture curvature	CILAS 36 actuator	2000	
Nasmyth Adaptive Optics System (NAOS) (Rousset et al., 2000, 2003)	VLT, UT4 (8)	14×14 or 7×7 Shack-Hartmann	CILAS 185 actuator	2001	
ALTAIR (Herriot et al., 2000; Stoesz et al., 2004)	Gemini North (8.1)	12×12 Shack-Hartmann	Xinetics 177 actuator	2002	DM optically conjugate to altitude of 6.5 km. Later found to be non-optimal and altered to be conjugate to telescope pupil.
NAOMI (Myers et al., 2003)	William Herschel Telescope (WHT) (4.2)	8×8 Shack-Hartmann	Trex Enterprises 76 segment	2003	Uses uncommon segmented DM.
PALM-3000 (Roberts et al., 2012)	Palomar 200 " (5.1)	64×64 Shack-Hartmann	Xinetics 349 and Xinetics 3368 actuator	2011	Current highest spatial order system on sky.
SAXO (Beuzit et al., 2008; Fusco et al., 2014)	VLT, UT3 (8)	40×40 Shack-Hartmann	CILAS 41×41 actuator	2014	AO system for Spectro-Polarimetry High-contrast Exoplanet Research (SPHERE) planet imager
GPI (Macintosh et al., 2012, 2014)	Gemini South (8.1)	43×43 Shack-Hartmann	CILAS 9×9 and Boston 4096 actuator	2014	Uses “Woofer-Tweeter” correction arrangement, where correction is split between low and high spatial orders.

Table 3.1: A selection of currently operating NGS AO systems

AO System	Telescope (diameter (m))	Laser	First Light	Notes
Lick observatory AO system (Max et al., 1997)	Shane Telescope (3)	18 W sodium pulsed dye laser, 589 nm	1996	
Keck LGS AO system (Wizinowich et al., 2006)	Keck (10)	12 W Lawrence Livermore National Labs Nd:YAG CW, 589 nm, Sodium	2004	Side-launched LGS results in up to 3″ SH spot elongation
ALTAIR (Boccas et al., 2006)	Gemini North (8.1)	12 W Coherent Technologies, 589 nm CW, Sodium	2006	
Subaru LGS AO (Hayano et al., 2008)	Subaru (8.2)	4 W 589 nm CW (frequency summed 1064 nm and 1319 nm YAG) Sodium	2006	
ESO LGS facility (Bonaccini-Calia et al., 2003, 2006)	VLT, UT4	13 W PARSEC, 589 nm CW, Sodium, dye laser	2006	
RoboAO (Baranec et al., 2012)	Palomar 60 inch (1.5)	10 W Rayleigh, ultraviolet, pulsed	2012	Fully automated and portable LGS AO system for small telescopes.

Table 3.2: A selection of single LGS AO systems.

featuring 30×30 sub-aperture pyramid WFSs and a tomographic LGS AO system. Both AO modes use adaptive secondary mirrors, each with 672 voice coil actuators (Esposito et al., 2011). The Advanced Rayleigh Ground Layer Adaptive Optics System (ARGOS) is the LGS AO system at the LBT. It runs in a Ground Layer Adaptive Optics (GLAO) configuration where multiple LGS are used to correct only for the ground layer of turbulence.

ARGOS features three Rayleigh LGS per primary mirror which propagate to an altitude of 12 km at a wavelength of 532 nm (Rabien et al., 2010). As the system uses a tomographic reconstructor and only ground layer correction is required, performance is not degraded by focus anisoplanatism and the, relatively low altitude, Rayleigh LGSs are adequate. As of mid-2014, ARGOS is currently undergoing commissioning and is expected to become available for science soon. The system will bring great gains in sky-coverage for the telescope. Using ARGOS, 84% of the sky is available for AO correction providing a Strehl ratio 0.1 , compared to only 54% if only the NGS is used to provide the same Strehl ratio.

3.4.2 Gemini Multi-Conjugate Adaptive Optics System

The Gemini Multi-Conjugate Adaptive Optics System (GeMS) at the Gemini South telescope has been planned for a number of years and has recently become fully operational for science use (Ellerbroek et al., 2003; Rigaut et al., 2012). GeMS is a Multi-Conjugate Adaptive Optics (MCAO) system which uses a combination of NGSs and five sodium LGSs to correct for turbulence at a number of altitude layers. As MCAO systems correct for meta-pupils at altitude with diameter larger than the telescope pupil they correct for a larger field of view. The use of MCAO had been pioneered by the Multi-conjugate Adaptive optics Demonstrator (MAD) at the VLT which has since been decommissioned (Marchetti et al., 2003).

The GeMS laser is a 50 W GuideStar Lockheed Martin Coherent Technologies sodium laser system. The single 50 W is split into five $\approx$ 10 W beams and launched into the sky behind the telescope secondary mirror (d'Orgeville et al., 2012). Three DMs are used for correction, with 293, 416 and 208 actuators, which are optically conjugate to the telescope pupil and altitudes of 4.5 km and 9 km respectively (Bec et al., 2008). Three NGS tip-tilt WFSs are also present, using Avalanche Photo-Diodes (APDs). Each of the five LGS WFSs is a 16×16 sub-aperture, quad-cell, SH WFS, which run at frame rates up to 800 Hz (Rigaut et al., 2013). The tomographic reconstructor in this case is similar to a SCAO system and is created by calculating interaction matrices from the DMs, then uses a Minimum Mean Square Error (MMSE) method to obtain a control matrix. This is possible as the WFSs observe the wavefront corrected by the DMs and are observing points across the intended science field of view (Neichel et al., 2010).

3.4.3 CANARY

The WHT has an illustrious history of hosting AO systems. In addition to the Multiple Aperture Real Time Image Normalisation Instrument (MARTINI) and Nasmyth Adaptive Optics for Multi-purpose Instrumentation (NAOMI) AO systems, it was also home to the tomographic Ground Layer Adaptive Optics System (GLAS), a Rayleigh LGS, GLAO system (Doel et al., 1991; Myers et al., 2003; Benn et al., 2008). Since 2010, the WHT has also hosted CANARY, a Multi-Object Adaptive Optics (MOAO) demonstrator for European Extremely Large Telescope (ELT) instruments (Myers et al., 2008; Morris et al., 2010). MOAO is an AO configuration correcting for a number of individual lines of sight within a large "field of regard", using information from a number of WFSs which observe within that field. The aim of CANARY is to demonstrate that concept by correcting for on-axis turbulence using only information from a number of off-axis WFSs. As CANARY has no astronomical science requirements it has enormously flexibility and has been used to investigate many issues within AO, such as novel wavefront reconstructors and vibration mitigation techniques (Sivo et al., 2013; Osborn et al., 2014; Bitenc et al., 2015).

In its initial phase, CANARY used three 7×7 sub-aperture SH NGS WFSs open loop of an 8×8 actuator CILAS DM as well as a further 7×7 sub-aperture WFS closed loop of the DM acting as a "truth" sensor to analyse AO performance along the corrected line of sight. NGS MOAO was successfully demonstrated in this configuration in 2010 (Gendron et al., 2011) using the Learn and Apply tomographic algorithm (Vidal et al., 2010), described in Section 2.4.2.2.

Since then, CANARY has been upgraded with four 7×7 SH LGS WFSs open loop of

Figure 3.1: A photograph of the CANARY LGS during the LGS commissioning phase in 2011.

the DM. The author of this thesis has been involved in alignment, calibration and operation of the CANARY LGS systems, though it is not detailed in this work. Two lasers are used to create the LGSs. Light from both is combined, then split into four separate beams using a Diffractive Optical Element (DOE). These are then launched from behind the telescope's secondary mirror to a height between 10 km and 20 km depending on atmospheric conditions. A photograph of the CANARY LGS is shown in Fig. 3.1. MOAO has now been demonstrated successfully using a combination of NGS and LGS information (Morris et al., 2013).

The focus of the CANARY project has moved to demonstrating and investigating Laser Tomographic Adaptive Optics (LTAO). The requirements for LTAO are similar to those for MOAO, though the WFSs are closed loop of the DM relaxing requirements for calibration but increasing the complexity of tomographic reconstruction.

3.4.4 Raven

Raven is in many respects similar to CANARY as it is an MOAO demonstrator, present at the Subaru telescope. The main difference between the two systems is that it is intended that Raven will have two science channels which will feed a facility spectrograph instrument (Conan et al., 2010).

Three 10×10 sub-aperture NGS WFSs are used that patrol a $2'$ field of regard. These are placed in open loop of the two 11×11 actuator ALPAO DMs, one correcting for each science channel. A single LGS WFS is also present which uses the existing Subaru sodium

LGS (Andersen et al., 2012). Reconstruction is performed using a variant of the Learn and Apply algorithm, described by Jackson et al. (2012). Raven saw first light in early 2014 and is currently undergoing a commissioning process which should soon see it available for science (Lardière et al., 2014).

3.4.5 VLT Adaptive Optics Facility

UT4 at the VLT is in the process of an upgrade to turn it into a dedicated "adaptive telescope", called the Adaptive Optics Facility (AOF). After this process all instruments will feature AO correction with tomographic AO configurations available (Kuntschner et al., 2012). All correction is performed by an adaptive secondary mirror with 1170 voice coil actuators. The AOF contains four sodium LGSs, each of which is a 22 W fibre laser made by TOPTICA. These are launched from the side of the telescope (Arsenault et al., 2012).

Two AO systems will be installed, GRAAL and GALACSI. Both systems use four identically designed 40×40 sub-aperture SH LGS WFSs with a dedicated tip-tilt NGS WFS. GRAAL performs GLAO only and feeds HAWK-I, a wide-field imager whilst GALACSI can perform either GLAO or LTAO and feeds the MUSE visible light Integral Field Unit (IFU) spectrograph. In its GLAO mode GALACSI is expected to double flux per channel of the IFU and in LTAO mode to provide Strehl ratios up to 0.1 at a wavelength of 650 nm (Paufique et al., 2012; Ströbele et al., 2012).

Development for the AOF is well underway and commissioning is due to begin in 2015, lasting until 2017, at which point the system will be ready for science (Arsenault et al., 2014).

3.5 Review Summary

In this chapter, current facility NGS and LGS have been outlined. Currently operating tomographic AO systems, including CANARY, Raven, GeMS and ARGOS have been discussed in detail, and the upcoming upgrade to the VLT, AOF, has been considered.

Tomographic AO systems are now beginning to be made available, though in many respects, tomographic AO development is still in its infancy. The method for retrieving LGS uplink tip-tilt information described in § 6 does not place any additional requirements for equipment on AO systems, but does require that the LGSs are launched from within the pupil. This means it could be applicable for the GeMS, CANARY and ARGOS systems, as well as future LGS systems which feature centre launched LGSs.

Chapter 4

A Tomographic LGS Adaptive Optics Simulation

4.1 Introduction to Simulation in Adaptive Optics

Simulation plays a large role in the development of Adaptive Optics (AO) systems. AO systems are optically complex and require expensive components such as Deformable Mirrors (DMs), Wavefront Sensors (WFSs) and a Real-Time Control System (RTCS), which are non-trivial to setup and optimise. Simulations allow AO scientists to experiment with different optical layouts and components without needing to obtain and prepare them physically. Novel concepts can be explored quickly and performance gains estimated – allowing the AO scientist to decide whether such a concept will provide suitable gains.

Equally important, parameters for new or existing systems can be optimised in a systematic way as it is possible to replicate a configuration in simulation and alter only one variable at a time. This is not an option on facility systems due to time constraints and the random nature of atmospheric turbulence. Accurate simulation is used to tolerance an AO system, for example, finding the performance sensitivity to misalignments of optical components. All the simulated data on a system can be combined to form an error budget which evaluates all the expected contributions of error to give overall performance estimates.

All AO simulation packages must provide some common functions. First, an atmosphere with a number of turbulence layer is modeled. Many AO simulations generate random phase screens adhering to some theoretical atmospheric statistical description, and are hence described as being "Monte-Carlo" simulations. One or more guide stars must then be simulated and the phase distortion for a given direction found by propagating light through the corresponding section of the various atmospheric turbulence layers. It is usually adequate to approximate this light propagation using a geometrical approach (Hardy, 1998), so phase perturbations can simply be summed from one height layer to the next. If the guide star is a Laser Guide Star (LGS) then the cone effect and, if desired, uplink turbulence must also be considered.

Next, WFSs must be simulated. These take the propagated light from a guide star and then model the effects of the optics and detector. Often the WFS will be of the Shack-Hartmann (SH) type, as this is most commonly found in current AO systems. Information from the WFSs will be passed through a reconstructor and commands sent to a simulated DM. This will create a phase shape to be subtracted from a propagated target astronomical science object phase to finally give a corrected phase. This can then be used to model the corrected science Point Spread Function (PSF) and system performance can be evaluated.

Alternatively, analytical codes also exist which use mathematical descriptions of individual components to evaluate the expected performance of a system (Rigaut et al., 1998; Jolissaint et al., 2006b). These can be run in much less time than Monte-Carlo codes as they do not have to simulate individual iterations of the system to produce a performance estimate. They do not provide the accuracy of a Monte-Carlo code as it is difficult to create a purely mathematical description of all components of an AO system, including effects such as misalignments, and so various assumptions must be made. Typically, an analytical code is used to roughly estimate performance and a parameter window within which a Monte-Carlo code can investigate further.

In this chapter, existing AO simulations are discussed, limited to Monte-Carlo codes which are available free, open-source and distributed with access to source code. This is vital to be able to alter and extend the code to simulate new AO concepts, not built-in by the code's author. The suitability of these codes to be used to simulate the LGS uplink tip-tilt retrieval algorithm, where the uplink path of the LGS is accounted for to predict the tip-tilt signal for LGS alone, is discussed before requirements for a new code with which to perform the simulation is considered. A new AO simulation, the Python Adaptive Optics Simulation (PyAOS), written by the author of this thesis in the Python programming language and designed with flexibility and accurate simulation of LGSs as a priority, is introduced and described. Comparisons with an existing and mature code is performed and the data presented.

4.2 Existing Adaptive Optics Simulations

A number of adaptive optics simulations exist, providing a variety of functions and written in a number of different programming languages. Some of the most widely used are briefly discussed below.

4.2.1 Yorick Adaptive Optics

Yorick Adaptive Optics (YAO) is a widely used AO simulation tool. It has been in development since the early 2000s and has evolved into a relatively fast, flexible, multi-purpose Monte-Carlo simulation code. It has recently been altered to take advantage of many processing core machines, significantly increasing performance. YAO has been used to investigate a multitude of AO use-cases, including modelling the Multi-conjugate Adaptive optics Demonstrator (MAD) (Marchetti et al., 2008), Gemini Multi-Conjugate Adaptive Optics System (GeMS) on the 8m Gemini South telescope (Rigaut et al., 2010), the AO system on the Giant Magellan Telescope (van Dam et al., 2010), and early studies into the feasibility of Multi-Object Adaptive Optics (MOAO) (Vidal et al., 2010). Due to the large number of

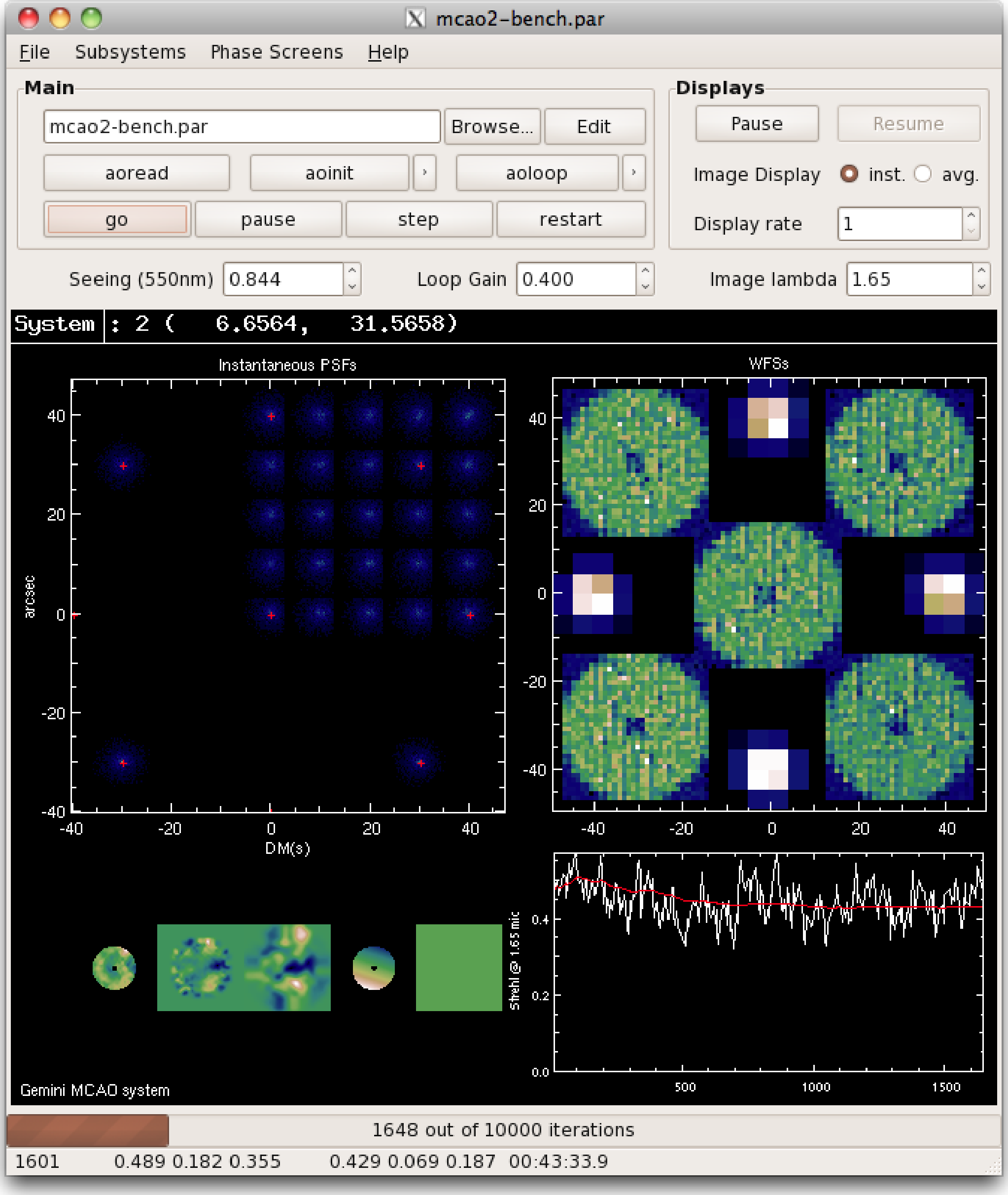

mcao2-bench.par

Seeing (550nm) 0.844

Loop Gain 0.400

Image lambda 1.65

Image Display ● inst. ○ avg.

Display rate 1

```
System : 2 (   6.6564,    31.5658)
```

```
1648 out of 10000 iterations
1601        0.489 0.182 0.355        0.429 0.069 0.187  00:43:33.9
```

Figure 4.1: The YAO GUI modelling the GeMS MCAO system, featuring multiple DMs, quad-cell Shack-Hartmann WFSs and many targets in a science field. It is possible to edit some simulation parameters from the GUI such as the seeing and loop gain whilst the system is running.

system which have been successfully investigated with YAO it can be regarded as a good benchmark for testing new simulations. The code is free, open source and available online*.

YAO is written in Yorick, a dynamic, interpreted programming language, with some accelerated routines written in C. Though not as fast as a purely compiled language, well written Yorick can still approach that speed as it provides explicit pointer access to C-style arrays and so avoids unnecessary creation of temporary arrays. Whilst the language has a strong following within the AO community, its usage outside of that is narrow. This severely limits the availability of third-party packages and support compared to other similar languages. For example, the YAO Graphical User Interface (GUI) uses a Yorick-Python compatibility layer to access PyGTK, as no GTK bindings are available in Yorick alone.

YAO can be quickly set-up to model a variety of AO systems through the creation of a configuration file where parameters such as WFS and DM type, reconstruction method and guide star position and magnitude are set. It is possible to model Shack-Hartmann WFSs either in full-diffractive or gradient estimate modes depending on the required accuracy. This allows YAO to be fast for large resolution systems for preliminary studies. A GUI is provided allowing the user to view the AO system, ensure is it working as expected and change parameters as the simulation is running. Fig. 4.1 shows an example system running in the YAO GUI.

To explore more novel systems, YAO must be extended by editing the provided source code. The lack of popularity of Yorick makes extending YAO a much harder task than if it was written in a more common programming language, as it unlikely the user will be familiar with Yorick syntax. Yorick does not feature any Object-Oriented capabilities, so YAO is written in a purely functional style. This can make extending more difficult, as the simulated components do not hold their own state or provide their own methods, and the user must be more familiar with the code than in the Object-Oriented case. These reasons make YAO unsuitable for simulating complex AO configurations where the user is not already familiar with Yorick. Investing effort into learning the Yorick syntax may not be time-effective as it is unlikely to be of use outside of YAO.

4.2.2 Durham Adaptive Optics Simulation Platform

The Durham Adaptive Optics Simulation Platform (DASP)† has been in existence since the late 1990s, though it underwent a large upgrade in 2007, extending the code to efficiently model Extremely Large Telescopes (Basden et al., 2007). Performance critical sections of DASP are written in the compiled C programming language and the rest, including user interfaces, are written in the Python programming language. Some algorithms have also been implemented in VHSIC Hardware Description Language (VHDL), used to provide further performance on some machines with Field Programmable Gate Array (FPGA) acceleration. Once a simulation has begun, it is controlled through either a Python based command line interface or a GUI, both of which are "connected" to a simulation externally over a network protocol.

---

[*] `http://frigaut.github.io/yao/`

[†] `https://www.dur.ac.uk/cfai/adaptiveoptics/dasp/`

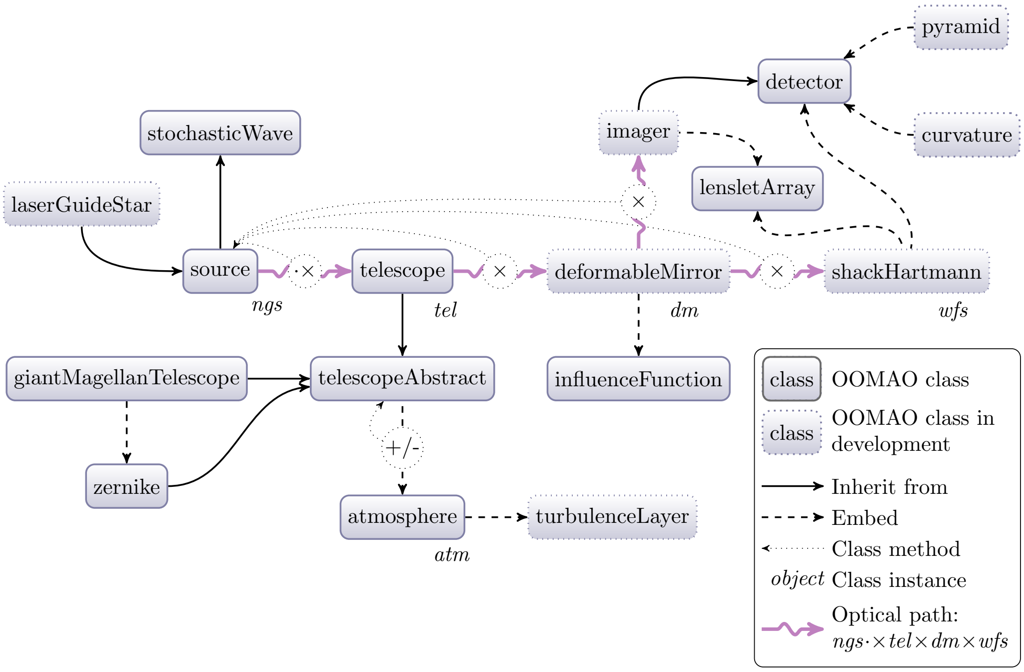

Figure 4.2: An example OOMAO class diagram which also indicates the development status of some classes as of 2014 (Conan and Correia, 2014). This illustrates a closed loop AO system on the Giant Magellan Telescope using either a pyramid, curvature or Shack-Hartmann WFS.

The simulation is heavily parallelised, where synchronisation signals are passed using the Message Passing Interface (MPI) library. Shared memory is used to allow parallelised components to safely access the same data at any one time. This approach allows large parameter spaces to be explored for Extremely Large Telescope (ELT) scale AO systems on manageable timescales of days or weeks, rather than months or years as in the other codes that were available in 2007. However, since then the development of more powerful processors has allowed less performance optimised codes to become more viable options for ELT scale investigations.

The high performance of DASP does not come without a price. A GUI is provided to set up a simulation, but a simulation still requires manual tuning as Python and XML configuration files must also be edited. As many components are written in the C programming language extending the code is not trivial as the extensions may also have to be written in C, increasing the development time in comparison to simulations written exclusively in a higher level language. This makes it difficult to investigate entirely new AO configurations using DASP as it is likely that compiled C code must be written and complex configuration files must be edited before it will be workable.

4.2.3 Object-Oriented, Matlab & Adaptive Optics

A more recent development in AO simulation is Object-Oriented, *Matlab*® & Adaptive Optics (OOMAO) (Conan and Correia, 2014). Work on the simulation was begun in 2010 and has been driven by modeling for the Raven MOAO system for the 8m Subaru Telescope on Mauna Kea, Hawaii (Andersen et al., 2012). OOMAO is written entirely in the *Matlab*® programming language, a proprietary, commercial, high level language and software suite designed by MathWorks for scientific computing, available for Linux, Mac OS X and Windows (MATLAB, 2014). OOMAO makes use of many algorithms built into *Matlab*®, which have been written and optimised in a compiled code. The *Matlab*® source code for OOMAO is open source and is available for download[*].

As its title suggests, the code is designed in an object-oriented fashion, where AO components are modeled as *Matlab*® objects. Extensive use of object inheritance is used to further abstract the user from the simulation code. An OOMAO class diagram illustrating a potential simulation design and development status as of 2014 is shown in Fig. 4.2. This design makes OOMAO very flexible, allowing a user to easily extend the code by inheriting existing classes and extending them as required.

Though OOMAO shows great promise as a powerful and flexible code for simulating novel AO configurations, it was not in a usable state at the beginning of this project.

4.2.4 Other simulation tools

Many other simulation packages exist which were not considered for the work presented in this thesis and some notable examples are listed below. The European Southern Observatory (ESO) has developed Octopus[†] (Le Louarn et al., 2004), a massively parallel simulation code designed to efficiently explore parameter spaces for ELT scale telescopes. Though a very powerful simulation package for this application, the code is not released publicly and is not designed for quickly modeling novel systems. Performance of Adaptive Optics for Large Apertures (PAOLA)[‡] is an analytic simulation tool, which does not generate Monte-Carlo phase screens, but calculates AO performance based on expressions of the power spectrum of corrected phase making the code run much faster for a given telescope diameter (Jolissaint et al., 2006a). This can be very useful for preliminary studies, to quickly explore large parameter spaces, but is not suitable for the AO configuration presented in this thesis, where more precise results are required. Finally, the COMputing Platform for Adaptive optics SystemS (COMPASS)[§], is a new project which aims to provide very high performance simulation capabilities for the purpose of ELT scale studies by making heavy use of Graphical Processing Units (GPUs) for acceleration (Gratadour et al., 2014). This is a promising development for the future, but would not yet feature the required flexibility to quickly model novel systems.

---

[*] `https://github.com/rconan/OOMAO/`

[†] `http://www.eso.org/sci/facilities/develop/ao/tecno/octopus.html`

[‡] `http://cfao.ucolick.org/software/paola.php`

[§] `http://lesia.obspm.fr/compass/`

4.3 The Python Adaptive Optics Simulation

The simulation packages discussed above are all either well established and trusted or show great promise for the future, though all would require a great deal of development before they were suitable for the tasks required in this thesis.

To successfully simulate the LGS tip-tilt retrieval, it is vital that the uplink path of the LGS is accurately modeled. Though uplink effects are included in some of the above codes, they compute an average signal to add to the final WFS measurement, rather than computing and convolving with an LGS PSF, using a physical propagation method. The method of LGS propagation is discussed in section 4.3.3.4. It is also desired that the simulation be as flexible as possible, to allow fast implementations of new reconstructors, or wavefront sensing and DM correction regimes. A further wish for the code is that it can be used as a learning tool for those new to the subject of AO, who can easily observe the effects of changing parameters or even make new configurations without huge experience of programming or AO.

Due to the other simulation package's chosen programming language or programming style it was deemed that it would be more effort to perform this extension than simply creating a new simulation tailored for allowing rapid development of new AO configuration concepts. The result of this work is the Python Adaptive Optics Simulation (PyAOS), an object-oriented, Python based toolkit which can be quickly reconfigured or extended. This code is described in more detail below; it is currently in a beta state and the source code is publicly hosted on Github with an open-source license[*].

4.3.1 The Python Programming Language

Python is a high-level, dynamic and interpreted language which is fast becoming the de-facto standard in scientific computing, as well as an extremely popular general purpose language. For example, the Tiobe index of programming languages cites it as the 7th[†] most used language and in terms of Github projects it is the 3rd[‡]. This compares very well with another high-level interpreted language, *Matlab®* , which is ranked 19th and 24th respectively.

It features an unusual syntax which uses only indentation to delimit code blocks, rather than any type of brace or bracket. Built-in data containers such as lists, dictionaries and tuples can contain any combination of data type or object. Python is object-oriented, supporting multiple inheritance and almost all data types, including integers and floats, are Python objects with methods and attributes. Due to the way this is implemented an object-oriented approach is not enforced on the programmer and it is possible to write complete Python applications in a purely functional manner. It is weakly typed, meaning that variables types do not have to be declared and their type can change at any time. Finally, Python includes a powerful documentation system where modules, classes and functions are documented in the source code allowing for interactive help from the Python interpreter or

---

[*] `https://github.com/andrewpaulreeves/pyAOS`

[†] `http://www.tiobe.com/`

[‡] `http://githut.info/`

easy compilation of a traditional documentation set. A small example of some Python code highlighting these features is given in Listing 1. These features make the typical development cycle for a flexible, stable and well documented Python program very fast in comparison to other languages.

```python
"""
Module Description Doc-string
"""

#Define a class, inheriting from a base class
class AO_Object(parentClass):
    """
    Class Description Doc-string
    """
    def AO_Method(self, arg1=None): #Define a method of a class
        """
        Method Description Doc-string

        This will be included in interactive help,
        and in compiled documentation
        """
        if arg1:
            print("Hello Python!")
        else:
            print("Goodbye Python")

AO = AO_Object()    #Make an instance of the class
result = AO.AO_Method()     #Use a method of the class
```

Listing 1: A simple example of Python code, showing the unconventional indentation based delimiting of code blocks, dedicated documentation string syntax and the ability to define objects or simply use Python as a scripting language.

As a dynamic, interpreted language, Python does not show the performance required for many applications in science. To address this shortcoming libraries for mathematical and scientific computing have been developed, the most notable being NumPy and SciPy. NumPy provides a multi-dimensional interface to C-style arrays, including operations which act on the entire array with one line of Python code. As these functions are implemented entirely in the C programming language, they are not limited by Python's slow, dynamic nature. To this end, Python can be used as a glue which holds together a multitude of accelerated libraries, ferrying pointers to and from highly optimised C or FORTRAN scientific libraries.

Due to the open source nature of the reference CPython interpreter, it has been possible for developers to create alternative run-time environments for differing purposes. A number of projects exist with the aim of developing a Python run-time environment which is faster than the de-facto standard CPython interpreter. These can take the form of alternative interpreters with optimisation using a Just-In-Time (JIT), such as Pypy[*], Pyston[†] and

---

[*] `http://pypy.org/index.html`

[†] `https://github.com/dropbox/pyston`

Numba[*]. A JIT works by compiling the code directly from an interpreted language to machine code immediately before it is run. Though incurring an overhead for the first run, the result can be cached and the same machine code used again. This can hugely increase the speed of a weakly typed, dynamic language such as Python by applying optimisations using information only known at run-time, such as the type of variables.

Alternatively, projects exist to convert Python to C code, with possible optimisations implemented, and then compiled. Examples of such an approach are Cython[†] and Nuitka[‡]. Both of the above methods can provide a significant speed-up for scientific Python code. Currently Cython and Nuitka are fully compliant with the CPython standard, PyPy is only lacking support for some external libraries, Numba supports a sub-set of Python features and Pyston development is in a very early stage. These projects hold the potential to vastly speed up pure Python code with little or no work by the programmer. Thus far, the Numba JIT compiler has been used to obtain simulation performance increases of up to 100 % versus standard CPython. These tools will be explored more in future to obtain greater speed-ups without resorting to lower-level languages.

Due to Python's very wide adoption, there are an enormous number of libraries available for use. These include popular scientific libraries, such as the Fastest Fourier Transform in the West (FFTW), whilst a variety of implementations of Basic Linear Algebra Subprograms (BLAS) and the FITPACK interpolation routines are wrapped within SciPy. Heavy use of these routines is made with the PyAOS avoiding the need to write and compile dedicated accelerated routines in a low-level language. Popular bindings to most GUI toolkits, such as Qt, GTK, WX and TK are available and actively supported, making it comparatively simple to create a user-friendly interface for novice users of the simulation. A variety of plotting libraries exist for different use cases, allowing easy presentation of data. In PyAOS, the matplotlib[§] library is used for slowly updated plots and the pyqtgraph[¶] library for plots which may be updated multiple times per second.

4.3.2 Simulation design

PyAOS has been developed with very clear goals in mind – to be extremely flexible and easy to use to enable rapid development of new AO concepts, with a particular focus on accurate and comprehensive simulation of LGSs. Every effort has been made to make the code as efficient as possible, though optimisations have not been carried out if they adversely impact the complexity of the simulation for the user.

Clear and complete documentation is a vital aspect of an easy to use software package. To this end full advantage has been taken of Python's advanced documentation system, with descriptions and stand-alone use examples given for each object doc-string, and method arguments and return types clearly indicated. The Sphinx library[‖] has been used to compile

---

[*] `http://numba.pydata.org/`

[†] `http://cython.org/`

[‡] `http://nuitka.net/`

[§] `http://matplotlib.org/`

[¶] `http://www.pyqtgraph.org/`

[‖] `http://sphinx-doc.org/`

an html version of the documentation which is hosted online*. As the majority of the documentation is contained in source code documentation strings, they can also be accessed through Python's built-in "help" system.

The simulation is arranged into objects which represent individual AO components. For most components, a base class is used which deals with most initialisation and interfacing with the rest of the simulation. These are intended to be inherited by more complex components which can add functionality, without needing to recreate interaction with the rest of the simulation, so long as some simple requirements in return type for some common methods are met.

A "master" module is provided which collates all the AO objects into standard AO configurations, allowing either open or closed loop control with multiple WFSs and DMs and the use of a variety of reconstructors. The parameters of the system are set in an external configuration file. This can be used in conjunction with a GUI coded in the PyQt4 toolkit, which plots all WFS detector images, DM shapes, science camera PSFs and allows a command line interface to edit parameters and view data whilst a simulation is running. This GUI is shown running a tomographic LGS AO system in Fig. 4.3. Interfaces to the master file and GUI are provided by the component object's base classes, allowing new, user created objects to be controlled by the master and viewed on the GUI, without requiring alterations to the core simulation code.

4.3.3 Simulation Objects

All components in the simulation are modeled as independent Python objects and can be used with or without the master module. Novel optical configurations, which may only contain some elements from a traditional AO system, can be taken and fitted together very easily in a small script. An example of such a script is shown in Listing 2, which shows how two WFSs parameterised by an external configuration file can be run. The most significant simulation objects are detailed below and a class diagram showing the relationship between objects given in Fig. 4.4.

4.3.3.1 Configuration

Any AO system is characterised by a plethora of different parameters which can have varying effects on AO performance. Development of a simulation quickly becomes unwieldy if all relevant parameters must be passed on every function call to a routine. In common with other simulation codes, PyAOS initialises the AO object with required parameters at the beginning of the simulation to avoid this. If the simulation objects are to be initialised and run by the user in a configuration other than the master, even passing the large set of parameters once is not ideal.

To simplify the initialisation of AO components, PyAOS uses configuration objects, created by a configuration module which reads the user defined configuration file. A configuration object for each AO component defined in the configuration file will be created containing all the parameters to describe that particular component. The user can include

---

[*] `http://pyaos.readthedocs.org/en/latest/index.html`

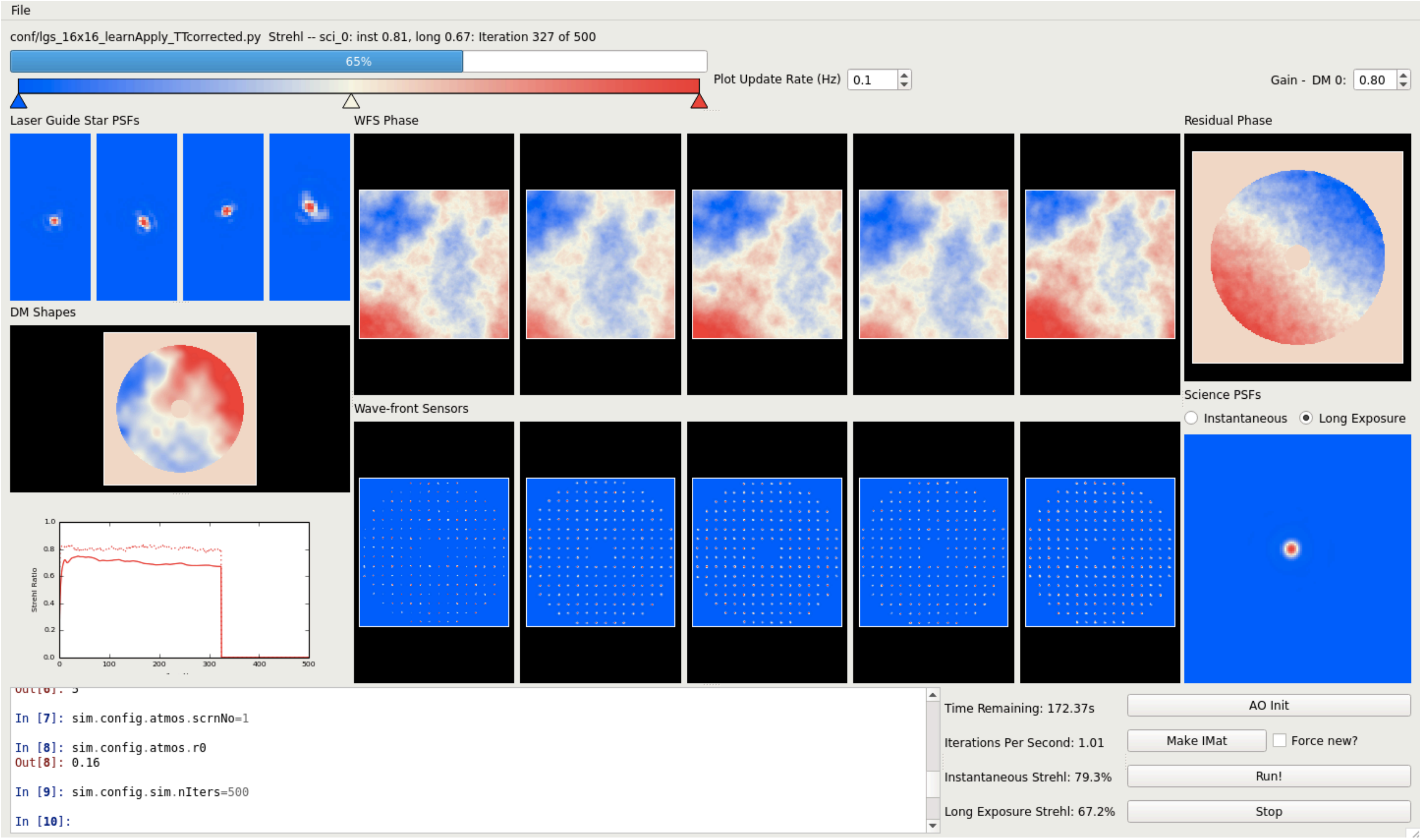

conf/lgs_16x16_learnApply_TTcorrected.py Strehl -- sci_0: inst 0.81, long 0.67: Iteration 327 of 500

65%

Plot Update Rate (Hz) 0.1

Gain - DM 0: 0.80

```
In [7]: sim.config.atmos.scrnNo=1

In [8]: sim.config.atmos.r0
Out[8]: 0.16

In [9]: sim.config.sim.nIters=500

In [10]:
```

Time Remaining: 172.37s

Iterations Per Second: 1.01

Instantaneous Strehl: 79.3%

Long Exposure Strehl: 67.2%

Figure 4.3: The pyAOS GUI. Simple use of the simulation is provided by the GUI which shows WFS images as well as the phase observed by each WFS, DM shapes, residual phase across the science target, the science PSF and, if LGS are present, the LGS PSF formed in the atmosphere. The console in the bottom left of the GUI provides an interface to set parameters or observe data while the simulation is running.

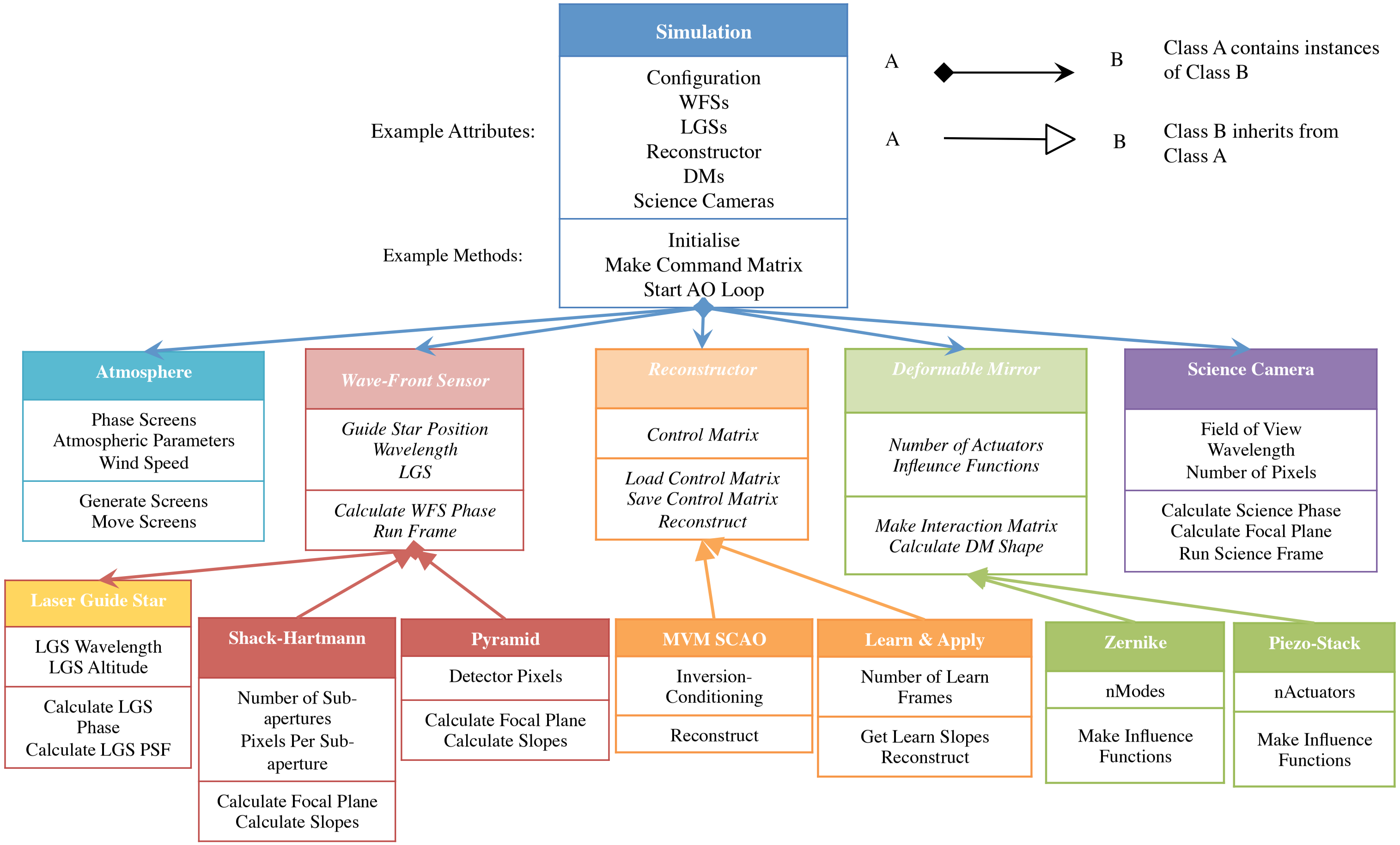

Figure 4.4: A class diagram representing the different components and inheritance trees in the PyAOS simulation. For each class some example attributes and methods are given. Base classes which are only intended to be inherited are represented in italics.

```python
#Import required modules from PyAOS
from pyAOS import WFS, atmosphere, confParse

#Initialise configuration object and read configuration file
config = confParse.Configurator("sim_configuration.py")
config.loadSimParams()

#Initialise the atmosphere
atmos = atmosphere.atmos(config.sim, config.atmos)

#Initialise two wavefront sensors, passing relevant config objects
wfs1 =  WFS.ShackHartmann(config.sim, config.wfs[0], config.atmos)
wfs2 =  WFS.ShackHartmann(config.sim, config.wfs[1], config.atmos)

#Initialise a data structure to hold results
data = numpy.empty((2, 100, wfs1.activeSubaps*2))

#Now run a loop, moving the atmosphere, then taking WFS frames
for i in range(100):
    phase_screens = atmos.moveScrns()
    data[0, i] = wfs1.frame(phase_screens)
    data[1, i] = wfs2.frame(phase_screens)
```

Listing 2: An example AO loop to run two wavefront sensors. The parameters for each WFS and the atmosphere are defined in the file "sim_configuration.py". In only a few lines of Python code, AO components can be run individually, or joined together in new and interesting configurations.

parameters required for newly created components by appending to a list in the configuration module. The new parameter will be read from the configuration file and be present in the configuration object relevant to that component. This method of configuration allows the creation and integration of new simulated components without the need to alter core simulation code and greatly increases the simulation's flexibility.

4.3.3.2 Atmosphere

The typical approximation used within AO simulations to model the atmospheric turbulence is using a number of infinitesimally thin phase screens. Within PyAOS, screens are generated using a method ported from code written in *Matlab*® and derived from Schmidt (2010), with Von Kármán statistics dependant upon the simulation configuration. The simulated phase screens are created using a Fast Fourier Transform (FFT) method which result in a screen that is periodic and continuous across its opposite edges.

The periodicity does imply an altered power spectrum from the theoretical Von Karman spectrum as there is less power than expected in low spatial modes. This can be visualised by considering a tilt across the entire phase screen – as the screen is continuous across the edges, such a global tilt is impossible. For large phase screens this is not a major issue as, in comparison to the telescope diameter, they will have a power spectrum very close to the theoretical. Schmidt (2010) details a method for creating small phase screens which still show statistics consistent with theoretical predictions. By adding "sub-harmonics" with an altered power spectrum to the usual FFT created phase screen, low-order spatial modes are created and the theoretical statistical prediction is achieved.

This is very useful for tasks where a large number of independent phase screens are required, for example, for quickly creating a tomographic reconstructor. As the phase screens can be created with smaller dimensions than those with no sub-harmonics, they can be created much faster, speeding up the simulation without compromising the accuracy of the atmospheric statistics.

For a standard simulation, large phase screens will likely be used. A window large enough to provide phase across the asterism of WFSs and science targets from each atmospheric layer is copied and returned for each simulation iteration. The window is moved across the large phase screen with a speed and direction dependent on the wind speed and direction. This is analogous to the Taylor hypothesis described in § 2.1.2 (Taylor, 1938). If the window is not placed on an integer number of phase pixels, the phase is interpolated so the wind speed and direction is consistent. As the large phase screens with no sub-harmonics added are continuous across the edges, when the window reaches the edge of the phase screen, the screen can be "rolled" around to continue the simulation, though some turbulence may be repeated. Using multiple phase screens at different heights and with different wind speeds and directions mitigates this potential problem, making it extremely unlikely that the same integrated turbulence will ever appear twice in a simulation integration.

4.3.3.3 Wavefront Sensors

Many new WFS designs continue to emerge for different purposes in AO (Ragazzoni, 1996; Gendron et al., 2010). Simulating new WFSs is critical for assessing any improvement in AO performance. For this reason, the simulation makes it as easy as possible to add and test new WFSs. All WFSs must view a Natural Guide Star (NGS) or LGS in a certain direction and an inheritable base class is provided to deal with this. It also provides interfaces to the master module and GUI. New WFS types can inherit the base class then provide methods to propagate the phase further and take a measurement. Shack-Hartmann and an experimental Pyramid WFSs have already been coded as these are the most common WFSs on existing instruments.

Using multiple WFSs for tomographic AO system is made simple by the modular nature of the simulations design. All the simulated WFSs are held in a list data structure and iterated over for each simulation frame. Currently, WFS detector noise is not modeled but will soon be added to the simulation using fast random number generation functions provided by NumPy. An approximation to noise is currently available which simply adds a random quantity onto the output measurements. This mode can be used to quickly determine a reconstructor's stability.

4.3.3.4 Laser Guide Stars

One of the main motivations for developing PyAOS was investigations into novel LGS configurations and consequently many aspects of LGS operation are accurately simulated.

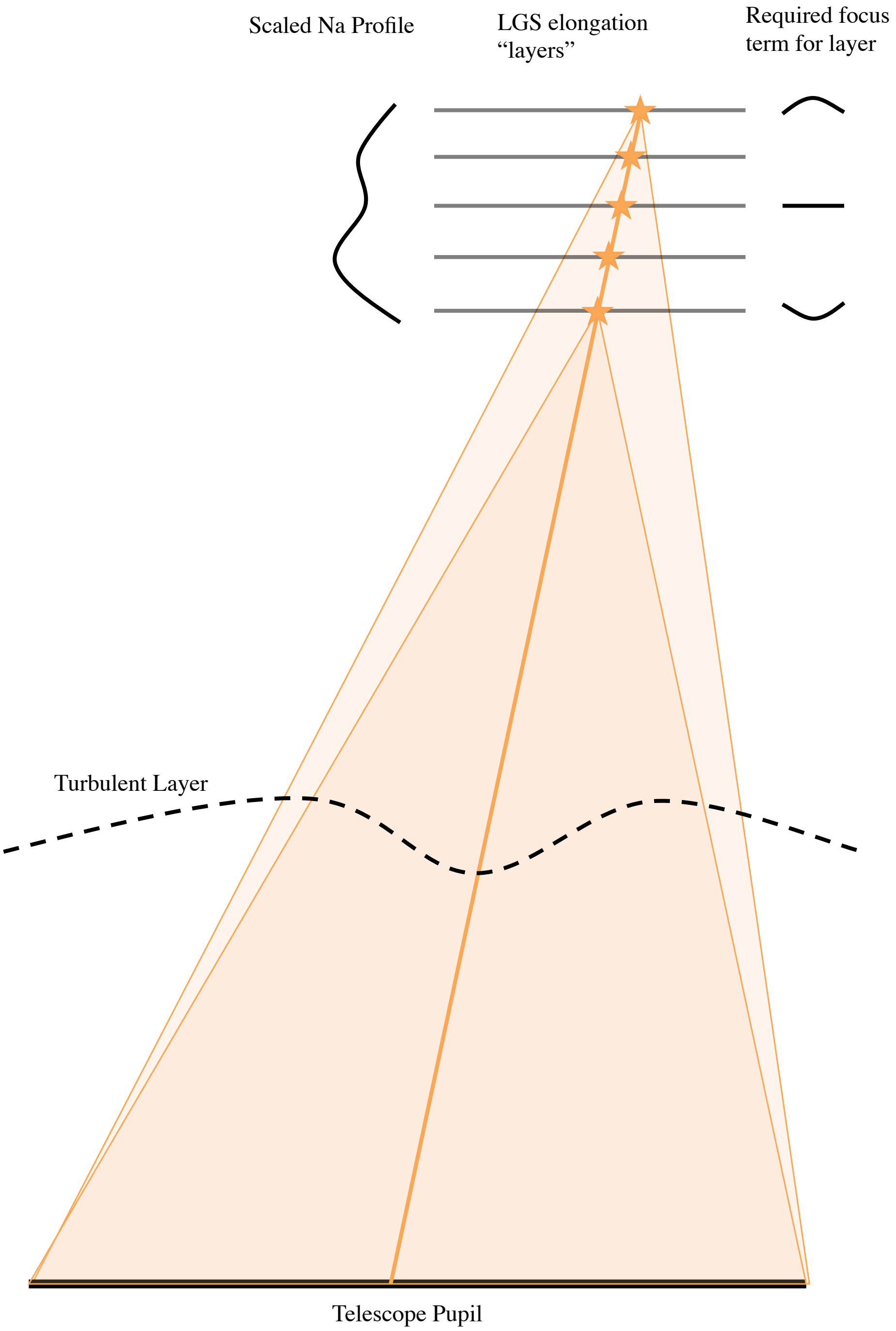

Figure 4.5: An illustration of the method of simulating LGS spot elongation in PyAOS. A number of LGS layers from different heights are propagated through the atmosphere and the result summed onto a common focal plane. The phase of each LGS layer is summed with a focus term to account for the effective defocus of the WFS for that layer, then it is scaled by a parameter representing the sodium layer profile from that height. Differential cone effect is also illustrated, where the lowest layer will observe a different cone of atmosphere to the highest.

LGS uplink is caused by the laser passing up through turbulence before forming a guide star. The turbulence causes movement of the LGS which is observed as spurious tip-tilt spatial modes on the LGS WFSs, rendering tip-tilt information from these WFSs useless. LGS uplink effects are reproduced in PyAOS by propagating the LGS light up through the atmosphere in a manner similar to light propagated down from guide stars.

An analysis by Holzlöhner et al. (2008) of the Fresnel number of typical LGS beams shows that a geometric optical approximation is not adequate for their simulation. Consequently, an angular spectrum propagation code is used to perform diffractive propagation of laser light from the laser launch telescope pupil, to each atmospheric turbulent layer, and then to the guide star height. The algorithm for this was taken from Schmidt (2010). Once propagated to the height of the guide star, the PSF formed by the laser is recorded, and is later convolved with each PSF formed in the WFS focal plane. This method accurately simulates the uplink tip-tilt observed on an LGS WFS caused by the laser's passage up through the atmosphere. It also accurately simulates other WFS errors which are present due to the finite size of the LGS PSF formed in the atmosphere.

Another potential large source of error when dealing with sodium LGS WFSs is the effect of the finite depth of the guide star due to the depth of the mesospheric sodium layer. On a SH WFS, this causes each sub-aperture spot to be elongated away from the launch position and effectively lowers sensitivity for sub-aperture centroiding in the direction of the elongation. As the extent of the elongation is dependent upon the diameter of the telescope primary, LGS spot elongation only marginally lowers AO performance on current telescopes. For the next generation of ELT scale telescopes it is expected that it will significantly impact performance and mitigation techniques must be investigated (Le Louarn et al., 2013).

To simulate the effect of LGS SH spot elongation, most commonly a SH WFS sub-aperture PSF is convolved with some "elongation kernel", dependent upon the position of the sub-aperture with respect to the LGS launch position. This method is computationally inexpensive as it only requires one operation to add the elongation to a standard WFS simulation, however there are disadvantages. Differential cone effect, where light from the highest point of the LGS beacon will pass through a slightly different cone of light than the lowest point is not simulated. As the spots are convolved with an artificial elongation kernel, it may also result in optimistic performance predictions for correlation based centroiding algorithms. In this scheme, a correlation is performed with the sub-aperture image and a predicted elongation shape, and the result used to obtain a centroid. As the simulated sub-aperture has been convolved with a known theoretical kernel to begin with, it is likely that removing a theoretical kernel will be more effective than if the elongation was formed by the sodium layer, which may have an unknown vertical profile.

In PyAOS, elongation is simulated in a different manner. The elongated LGS beacon is assumed to be a number of individual point sources along the laser path with differing heights. The WFS is focussed at the mid point of the beacon, but for higher or lower points a focus term is calculated corresponding to the defocus caused by the distance from best focus. Each point is propagated down to the telescope pupil with the usual method and before a focal plane is calculated, the defocus term added. The intensity from each LGS elongation layer is scaled to create a user-defined sodium layer intensity profile, then summed onto a common detector image before centroiding is performed. The process is illustrated in Fig. 4.5. Due to the multiple optical propagations required for each WFS frame, this method is not as fast as the convolution method but because of the reasons described above provides higher simulation fidelity.

4.3.3.5 Deformable Mirrors

In common with other simulated components in PyAOS, a base deformable mirror class is provided which deals with initialisation, the making of interaction matrices and interaction with the AO loop. Different DMs are defined by creating a method which constructs the DM influence functions. Zernike, Piezo stack-array, Gaussian stack-array and tip-tilt DMs are currently available in PyAOS. For the Zernike DM, influence functions are simply Zernike modes; this is useful for comparing with theoretical predictions but little use for assessing real-world systems. The stack-array DMs influence functions are a grid of "actuators" where each influence function is the shape of the DM where only one actuator is activated. In the case of the Gaussian DM, the actuators are modeled by 2-dimensional Gaussian functions. The Piezo DM is modeled by interpolating up to the simulation size from a grid of zero set actuators with only the relevant element set to one. This simulates a thin mirror surface when pushed or pulled from behind by an actuator. Inter-actuator coupling is not simulated explicitly, though individual influence functions may extend into the adjacent actuator space. Finally, a tip-tilt mirror is modeled as a Zernike DM but with only the tip-tilt modes as influence functions.

4.3.3.6 Reconstructors

The AO reconstructor in the simulation is modeled as another Python object which uses WFS and DM objects to create a command matrix then during the loop is passed WFS data and returns DM commands. Once again, the infrastructure around this functionality such as loading and saving of DM interaction matrices and the system command matrix, is handled by the base reconstructor class. Each reconstructor must provide methods to make the control matrix and a reconstruct method to actually calculate DM commands from WFS data. An example of the definition of a new AO reconstructor is given in listing 3, where a reconstructor using an Artificial Neural Network (ANN) is shown. This has been used for early investigation into using ANNs for tomographic AO that may be robust against changing atmospheric vertical profile (Osborn et al., 2012).

4.3.4 Computational Performance

Though the code hasn't been written with computational performance as a main motivation, every effort has been made to make the code as efficient as possible without compromising simulation fidelity or ease of use. Wherever possible, NumPy or SciPy is used to perform computationally intensive algorithms. FFTs are used extensively in the simulation and physical propagation of LGSs in particular uses a number of FFTs per iteration. To mitigate the impact of the FFTs on simulation speed, the FFTW library is used for all FFTs in the simulation. Circular memory buffers are allocated at initialisation for WFSs, DMs and the

```python
class ANN(Reconstructor):
    """
    Reconstructs using an Artificial Neural Network
    Assumes on axis slopes are WFS 0
    """
    def makeCMat(self, net):
        """
        Defines the reconstruction Network
        Args:
            net: The pre-made neural network object.
        """
        self.net = net

    def reconstruct(self, slopes):
        """
        Determine DM commands using Artificial Neural Network.
        Args:
            slopes (ndarray): array of slopes to reconstruct from
        Returns:
            ndarray: array to commands to be sent to DM
        """
        offSlopes = slopes[self.wfsSlopes:]
        onSlopes = self.net.run(offSlopes)
        dmCommands = self.controlMatrix.T.dot(onSlopes)

        return dmCommands
```

Listing 3: A simple example of the definition of a new reconstructor within the code. The inherited “Reconstructor” base class deals with most simulation interaction, and the user must only define a couple of new methods for the new reconstructor class. This example shows the definition of an Artificial Neural Network (ANN) reconstructor which is currently under investigation for tomographic AO purposes, where the ANN has been pre-computed using using previously recorded WFS data.

reconstructor to avoid unnecessary re-initialisation of memory during simulation run time. There is also rudimentary multi-core support for multi-WFS AO configurations, where each WFS is run in a separate process, significantly reducing computation time for such systems. Timings from the comparison data presenting in § 4.4 suggest that PyAOS currently runs at roughly a fifth of the speed of YAO for single WFS AO configurations.

There is still much potential for optimising the code, and this will be necessary for the code to be viably used for ELT scale studies. Performance profiling has been undertaken, demonstrating that the WFSs and DMs are the most computationally intensive components. The porting of some parts of the code using the Open Compute Library (OpenCL) based Python package to run with Graphical Processing Unit (GPU) acceleration has begun, and shows significant speed-ups. If porting the entire code is successful, this could allow ELT scale operation of the simulation on time-scales competitive with performance optimised codes.

Parameter	Value
Simulation Phase Elements	128
Number of Turbulence Layers	4
Integrated Seeing Strength, r_0 (cm)	18.6
Fractional Layer Strength	0.5, 0.3, 0.1, 0.1
Layer Wind Speeds ($\mathrm{m\,s^{-1}}$)	10, 10, 15, 20
Frame Rate (Hz)	400
Exposure Time (s)	12.5
Whole Phase Screen Diameter (m)	256
Telescope Primary Diameter (m)	8
Number of Sub-apertures	8×8
Pixels Per Sub-aperture	10
Number DM Actuators	9×9
Guide Star Position	On-axis
Science Target Wavelength (µm)	1.65

Table 4.1: The parameters used in the comparison simulations, unless otherwise stated.

4.4 Simulation Comparisons

It is important that when a new AO simulation is introduced, it is tested against a current and accepted code to ensure that the results from the new code are accurate. Here, PyAOS is compared with YAO, a mature AO code in a number of AO configurations. The YAO configurations are either taken directly from the YAO example directory supplied with the code, or are only slightly altered from these files. This ensures that YAO is not used in a sub-optimal fashion.

For the purposes of simulating the LGS uplink tip-tilt retrieval method, it is vital that simple effects such as fitting error, guide star geometry and turbulence strength scaling are modeled. Comparison are presented below which present this. The parameters for the simulations are listed in Table 4.1, except where otherwise stated.

4.4.1 Adaptive optics performance with number of sub-apertures

A comparison between YAO and PyAOS of AO performance with increasing SH WFS sub-apertures is shown in Fig. 4.6. This comparison test confirms that the simulation is correctly reproducing the fitting error expected when a DM with a finite spatial resolution is used to correct optical aberrations with high spatial orders present. As absolute performance for a given atmospheric profile is very close between the two codes, it also indicates that the creation and scaling of atmospheric turbulence in the new code is correct.

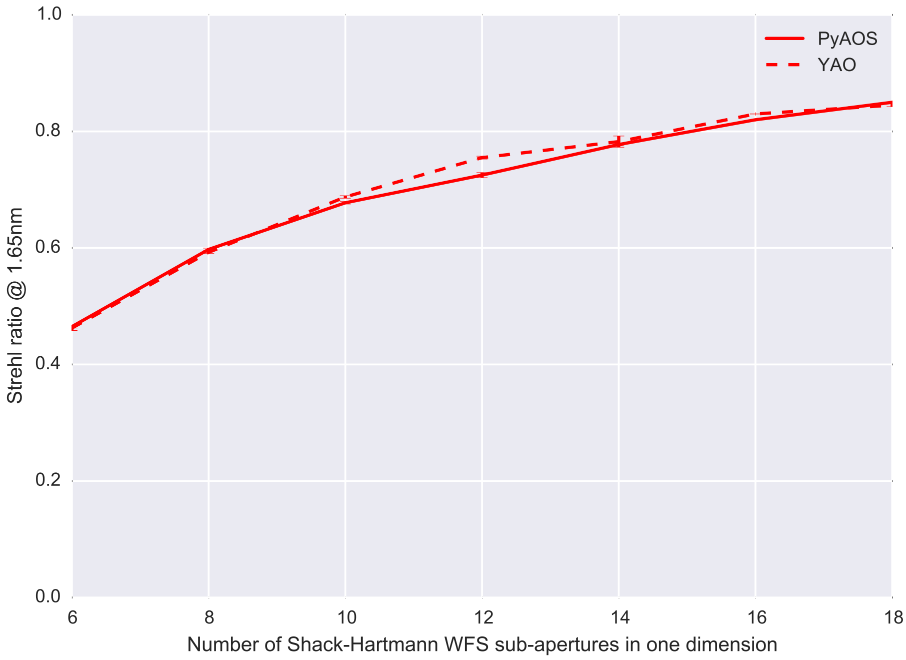

Figure 4.6: A comparison of AO performance between PyAOS and YAO with an increasing number of SH WFS sub-apertures. Each data point is the result of running a simulation 4 times with the same parameters but different randomly generated phase screens.

4.4.2 Adaptive Optics Performance with Increasing Angular Anisoplanatism

Next, data is presented comparing YAO and PyAOS when the angle between the science target and the guide star is increased. For simplicity, the atmosphere is modeled as a single turbulence layer at a height of 5 km. This is simulated for three values of integrated seeing strength, with r_0 values of 10 cm, 15 cm and 20 cm. The results are shown in Fig. 4.7.

The simulations are again closely matched, demonstrating the validity of the simulation of guide star geometry within PyAOS. The performance for differing seeing strengths is also close, verifying the scaling of turbulence within PyAOS.

4.4.3 Adaptive Optics Performance for Increasing Focus Anisoplanatism

Finally, the AO performance of a single LGS AO system if uplink turbulence is ignored is compared between PyAOS and YAO. The results of this comparison are shown in Fig. 4.8. Three altitudes of LGS are simulated, with 15 km and 25 km being typical values for Rayleigh LGSs, and 90 km as the mean altitude of a sodium LGS. A single NGS system is also simulated for control purposes.

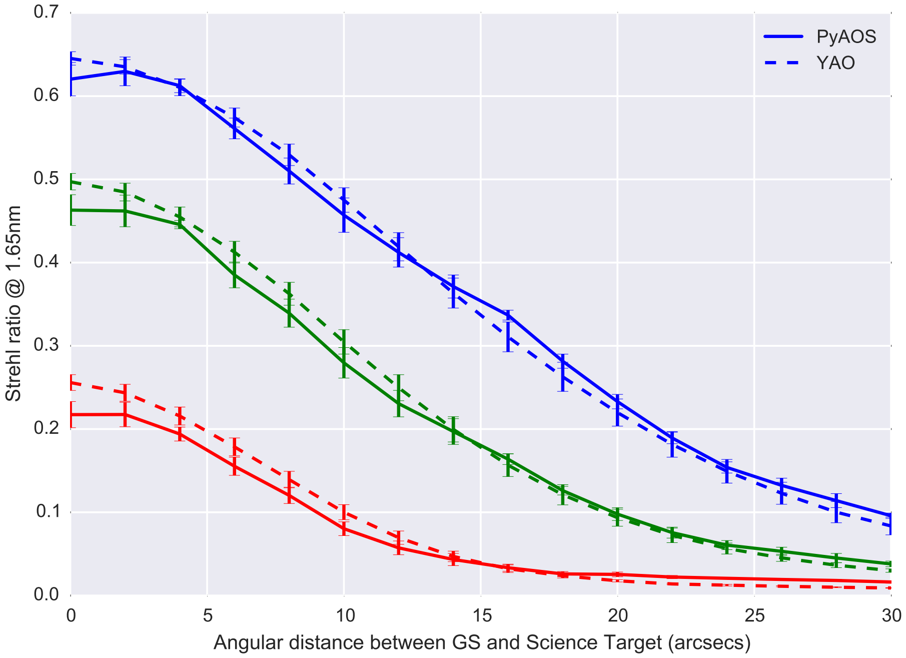

Figure 4.7: A comparison of AO performance between PyAOS and YAO with increasing separation between the NGS and a science target. Three values of r_0 are modeled, the lowest curve, 10 cm, the middle, 15 cm and the highest, 20 cm. Each data point and its associated error is the result of running a simulation 4 times with the same parameters but different randomly generated phase screens.

For each guide star configuration, a single turbulence layer is simulated, and its height increased. When the layer is at low altitudes, focus anisoplanatism, described in § 2.3.6.2, is low, hence good correction is performed for all guide star altitudes. As the layer increases, both simulations show that performance reduces, with the reduction dependant upon the altitude of the guide star. For both simulations, the NGS system retains constant performance, as expected.

There is a discrepancy between the absolute performance predicted by the simulations. The YAO simulation shows performance dropping more quickly for a given turbulence layer altitude than PyAOS. This discrepancy is currently under investigation. It is not deemed significant for the simulations carried out in this thesis as only tomographic LGS AO systems are performed, where focus anisoplanatism is mitigated.

4.5 Summary

This chapter has discussed the currently available options for simulation of new AO systems, and the reasons and requirements for a new simulation. PyAOS, a tomographic, LGS enabled AO simulation, written in the Python programming language is introduced, which is aimed for rapid development of complex AO concepts.

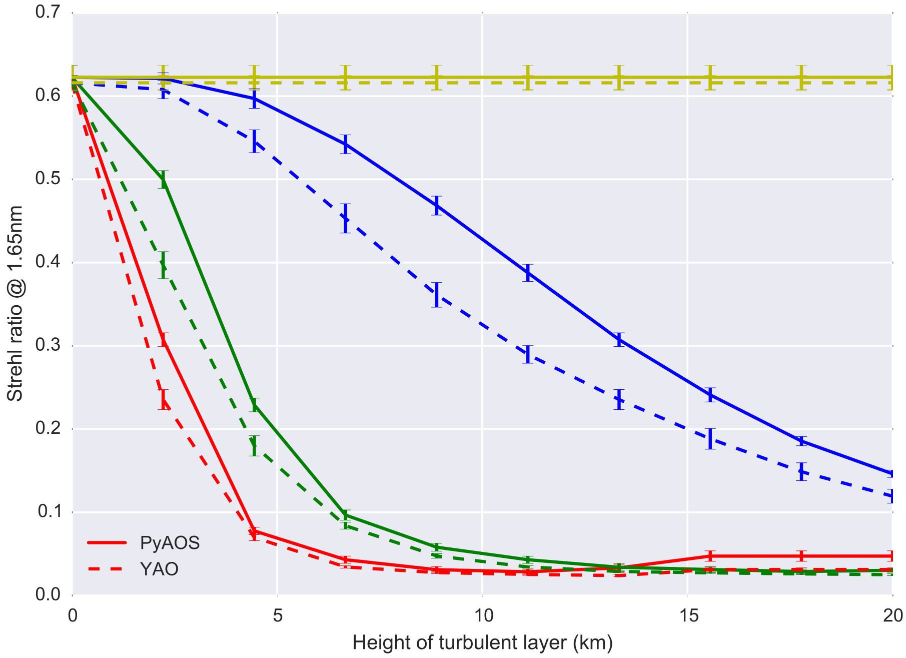

Figure 4.8: A comparison of AO performance between PyAOS and YAO using a single LGS, with varying height of a single turbulence layer. Three LGS altitudes, 15 km, 25 km and 90 km, and a NGS are modeled, represented by the lowest to highest performing curves respectively. Whilst both simulations exhibit the same trend, they have different absolute performance estimates. Research is underway as to the cause of this discrepancy.

PyAOS is described, including a discussion into the simulation of LGSs by PyAOS and other codes. Finally, results from PyAOS are compared to a mature AO simulation code, YAO, which validate the new simulation, though discrepancies regarding focus anisoplanatism have been identified. These are currently under investigation but are not regarded significant for using the simulation in the remainder of this thesis. The PyAOS simulation will be used subsequently to investigate the LGS uplink tip-tilt retrieval method described in § 6, with results presented in § 7.

Chapter 5

The Durham Real-Time Adaptive Optics Generalised Optical Nexus

5.1 Introduction to DRAGON

The Durham Real-Time Adaptive Optics Generalised Optical Nexus (DRAGON) is a new laboratory test bench which has been under construction since 2010 at the Centre for Advanced Instrumentation (CfAI), Durham University. It has been designed to emulate tomographic adaptive optics systems and to accurately replicate the atmosphere and Laser Guide Stars (LGSs) (Reeves et al., 2012). The author of this thesis has been heavily involved in all stages of design, construction and integration of the system including systems engineering, optical and mechanical design of a number of components and overall system integration. In particular, the author responsible for overall project management, designed the Wavefront Sensor (WFS) and laser launch optics and mechanics, lead integration and testing and has played a significant role in the development of control and analysis software.

In this chapter Adaptive Optics (AO) laboratory test benches in general are discussed before the motivation and requirements for DRAGON are explained, with particular emphasis given to the unique features it possesses which aid the investigation into methods of LGS up-link retrieval. Finally, results from the DRAGON system integration are presented.

5.1.1 Adaptive Optics Laboratory Test Benches

Though in use in a number of facility instruments at observatories across the world, as described in § 1, AO is still a relatively recent technology. § 3 describes how the vast majority of current facility systems are almost all Single Conjugate Adaptive Optics (SCAO) systems, where one Natural Guide Star (NGS) or LGS within the isoplanatic patch size around the science target is observed in order to predict the atmospheric phase distortions in that direction.

Tomographic AO configurations have been proposed which increase sky coverage, overcome focus anisoplanatism and increase the corrected field of view. There a very few tomographic systems currently operating – CANARY, the Gemini Multi-Conjugate Adaptive Optics System (GeMS) and Raven are the only AO systems which perform tomographic wavefront reconstruction more complex than Ground Layer Adaptive Optics (GLAO) (Myers et al., 2008; Conan et al., 2010; Rigaut et al., 2012). CANARY and Raven are Multi-Object Adaptive Optics (MOAO) demonstrators, CANARY on the 4.2 m William Herschel Telescope (WHT), and Raven on the 8.2 m Subaru telescope, and GeMS is a facility Multi-Conjugate Adaptive Optics (MCAO) system at the 8.1 m Gemini South observatory.

The development of these systems has taught AO scientists a great deal about tomographic AO systems. One fact that has been made clear by current systems is that there is still much to learn before it is possible to achieve robust, optimal correction or to create a tomographic AO system of the scale required for an Extremely Large Telescope (ELT) (Gendron et al., 2011; Vidal et al., 2013; Lardière et al., 2014). As the above systems are based on working facilities commissioning time is extremely limited. Laboratory benches, on the other hand, offer almost unlimited time to test and optimise tomographic AO on systems which can be built to approximate real telescopes.

5.1.2 Review of Adaptive Optics Laboratory Test Benches

Many other laboratory AO experiments have been used to explore various new concepts. These can take the form of dedicated AO test benches used by an institution for a variety of investigations or small experimental optical trains for fast development of a particular idea. In this Section, some prominent examples of the former are described.

5.1.2.1 The Hartmann Oriented Multi-conjugate Experimental Resource

The Hartmann Oriented Multi-conjugate Experimental Resource (HOMER) is the AO test bench at the Office National d'études et de Recherches Aérospatiales (ONERA), which was integrated in 2007 (Costille et al., 2010). It has been designed to investigate tomographic wide field AO modes, such as MCAO, GLAO and Laser Tomographic Adaptive Optics (LTAO). A single, 7×7 sub-aperture Shack-Hartmann (SH) WFS is used which is designed with many pixels per sub-aperture and a small plate scale. This allows multiple guide stars to be observe on the same WFS.

A 52 actuator (8×8) ALPAO Deformable Mirror (DM) is optically conjugate to the telescope pupil and a 88 actuator (10×10) ALPAO DM conjugate to altitude, where the altitude can be reconfigured. Turbulence is generated either by using rotating phase screens, or using the DMs. Real time control of the system is handled by a Central Processing Unit (CPU) based system, created by Shakti Solutions. The system runs at a frame rate of 10 Hz.

5.1.2.2 The High Order Test Bench

Before the creation of facility Extreme Adaptive Optics (XAO) systems, such as the SPHERE Adaptive Optics for eXoplanet Observation (SAXO), the Gemini Planet Imager (GPI) and Palm 3000, the European Southern Observatory (ESO) were keen to investigate optimal wavefront sensing and control schemes for high-order AO in the laboratory. The result is the High Order Test-bench (HOT), an extension of their existing Multi-Application Curvature Adaptive Optics (MACAO) bench (Vernet et al., 2006; Aller-Carpentier et al., 2008). Both a

SH WFS and a Pyramid WFS are used for the purposes of comparison, with both observing on axis. The SH WFS has 31×31 sub-apertures and the Pyramid either has 31×31 or 48×48 sub-apertures.

Turbulence is generated using three sets of two reflective turbulence screens with integrated seeing of $0.5''$, $0.65''$ or $0.85''$. Only the screens with seeing $0.65''$ show Kolmogorov statistics, whilst the other sets show reduced low order aberration. In addition to the MACAO 60 element bi-morph DM, HOT features a 32×32 Boston Micro-Electro-Mechanical System (MEMS) device for high-order correction. The SPARTA Real-Time Control System (RTCS), the same as that which runs AO systems at the Very Large Telescope (VLT), controls the system at rates up to 100 Hz.

5.1.2.3 SESAME

SESAME is the laboratory AO test bench at the Paris-Meudon Observatory. It emulates an 8 m telescope with a $2'$ unobstructed field of view. It features multiple 14× 14 sub-aperture WFSs. It has been used for a number of purposes including initial tests of tomographic reconstruction for MOAO (Vidal et al., 2010) and investigations into open loop DM control for different DM technologies (Kellerer et al., 2012).

5.1.2.4 The Victoria High Order Test-bench

The Victoria Open Loop Test-bench (VOLT) is not strictly speaking a laboratory test bench as it is based at a 1.2 m telescope at the Dominion Astrophysical Observatory in Victoria, Canada. It is classed here as such as it is not designed for science, but purely as an AO bench to test open loop DM control (Andersen et al., 2008). The seeing at the site is relatively strong, where r_0 is between 4 cm and 6 cm. VOLT saw first light on-sky in 2008.

The VOLT features three 7×7 SH WFSs. WFS 1 is open loop of the 52 actuator ALPAO DM and is used to provide the wavefront information to corrected for the atmospheric turbulence. WFS 2 acts as a “truth” sensor, closed loop on the DM. This can be used to run the system in closed loop to give a performance reference or to measure the residual wavefront error when running in open loop. Finally, WFS 3 is a “figure” sensor, which uses an external reference source to monitor the shape of the DM.

5.1.2.5 Discussion of Existing Laboratory Adaptive Optics Benches

None of the systems mentioned previously feature realistic emulation of LGSs, either, only considering NGSs, or treating LGSs as a point source optically conjugate to a finite altitude. This method accounts for focus anisoplanatism, but does not for either spot elongation or uplink turbulence. A point source can be made to exhibit SH spot elongation by using a DM to scan through focus for each iteration, but this slows down the frame rate of the system and doesn’t allow for real time operation (Turri et al., 2014).

Multiple WFSs and high spatial order correction have been investigated separately in a number of the mentioned test benches, but they are not found together. Wide field, visible light AO correction requires that multiple, high-order WFSs are combined to provide tomographic reconstruction. All the aforementioned benches feature some form of turbulence generation, but none can deterministically alter the vertical turbulence profile in real time.

5.1.3 DRAGON Research Goals and Requirements

Unlike simulation codes, it is difficult to share the use of laboratory facilities between institutions. For this reason, an AO test bench is a useful asset for the Centre for Advanced Instrumentation whatever its capabilities. None-the-less, there are requirements for DRAGON which are not found in existing laboratory experiments.

DRAGON has been created with a number of clear research goals in mind. These are based around LGSs, tomographic AO configurations, challenges for ELT scale AO systems, and development of RTCSs. In the following section, these are discussed in greater detail, and the requirements for the DRAGON bench considered for each.

5.1.3.1 Robustness of Tomographic Reconstruction

Tomographic AO systems rely on a wavefront reconstructor which accounts for the vertical optical turbulence profile of the atmosphere to determine the required correction in the direction of an astronomical science target. The reconstructor can be built explicitly, with knowledge of the atmosphere from external atmospheric profilers or from data obtained by the AO system itself. The is described in greater detail in § 2.4.

It is known that the vertical profile of the turbulence can change on short time scales, and this will adversely effect the performance of the tomographic reconstructor (Shepherd et al., 2014). This has begun to be investigated and Gendron et al. (2014) have developed an analytic form of the wavefront reconstruction error due to a sub-optimal vertical profile for the tomographic reconstructor. It is likely that the reconstructor will have to be continually updated as the vertical profile changes or that for some turbulence conditions GLAO may give better performance than MOAO. DRAGON can fill a vital gap between simulation and on-sky experiments with CANARY in assessing these proposals and in developing solutions.

DRAGON is suitable for such investigations as the system features multiple guide stars to build and use the tomographic reconstructor. As all WFS feature a relatively large number of sub-apertures, high tomographic altitude resolution is possible. Multiple turbulence layers are provided, which can dynamically change in height to emulate an evolving vertical turbulence profile.

5.1.3.2 Tomographic Laser Guide Star Adaptive Optics

Current AO systems cannot retrieve all the required correction from LGS alone and use NGS to provide at least tip-tilt information. Tomographic LGS AO systems return more information from WFSs observing in different directions which has the potential to provide tip-tilt information using only LGSs. To allow bench investigations of this concept DRAGON will emulate LGS up-link turbulence with a laser beam launched up through the same multi-layer turbulence emulator that provides turbulence for the LGS WFSs.

LGS WFS sub-apertures far from the launch point observe the LGS beacon from an off-axis position, and the sub-aperture spot is therefore elongated. This effect can degrade performance on existing 8-10 m class telescopes, but the problem is vastly greater for ELTs. DRAGON will emulate LGS elongation in real-time, so that centroiding algorithms to mitigate the effect can be investigated.

5.1.3.3 Visible Wavelength, High Order Adaptive Optics

Visible AO has long been a goal of the AO community. With the exception of some recent systems such as SAXO, GPI and Palm 3000, AO correction has almost exclusively been limited to correcting infra-red wavelengths, where light is less degraded by atmospheric turbulence (Davies and Kasper, 2012). In order for optical aberrations to be corrected, higher spatial resolution wavefront sensors and correction devices are required and must be run at higher frame rates. Vibration mitigation techniques and predictive control schemes are also required to achieve the highest possible Strehl ratios (Sivo et al., 2013). Although these concepts have already been investigated for NGS SCAO systems, DRAGON can combine them with tomographic LGS wavefront sensing, running at relatively fast, real-time rates. DRAGON features two deformable mirrors in a Woofer-Tweeter arrangement, providing low-order, large stroke and high-order, low-stroke correction separately, allowing it to correct for visible wavelengths.

5.1.3.4 "Push-button" Adaptive Optics

AO systems have evolved from single WFS and DM SCAO arrangements with Matrix Vector Multiplication (MVM) based reconstructors to multi-WFS, multi-DM tomographic AO systems with complex reconstructors. With the increase in complexity systems have become increasingly difficult to initialise and run. It is now usual practice for a tomographic AO equipped observatory to employ one or more AO operators in addition to the telescope operator during an observing run. The Robo-AO project has admirably simplified the operation of LGS SCAO schemes (Baranec et al., 2012), though doing the same for tomographic AO may be more difficult. DRAGON will be used to develop AO control software for tomographic AO which is robust and simple to operate in an attempt to reduce the cost and time overhead of complex AO systems in a similar manner.

5.1.3.5 Extremely Large Telescope scale Real-Time Control

Tomographic AO systems require many WFSs which each contain many sub-apertures to provide adequate spatial resolution across a very large aperture. A computational problem which is easily handled for current telescope diameters becomes very difficult for ELTs, even with the projected power of computational hardware in the near future. DRAGON is designed to provide a comparable data load to a small ELT instrument and so stress test algorithms and hardware, such as Graphical Processing Unit (GPU) or Field Programmable Gate Array (FPGA) acceleration, which can be used for ELT scale systems.

5.2 DRAGON Description

5.2.1 System Overview

DRAGON is designed to emulate a 4.2 m telescope aperture with $3'$ field of view analogous to the WHT. This allows modules developed and built for DRAGON to be used on the CANARY MOAO demonstrator which is present on the WHT. With minor modifications DRAGON can also be switched to emulate an 8 m telescope.

The system is modular and has been designed to be easily reconfigured. Each module accepts and outputs an 18 mm diameter beam optically conjugate to the telescope pupil, allowing the modules to be reconfigured into a variety of arrangements. For instance, the WFSs can be be moved from open to closed loop with respect to each DM without significant re-alignment. As well as the modules described below, several pupil to pupil relays are used to relay light between modules where additional physical bench space is required. These relays have been designed to preserve image quality across the systems $3'$ field of view and also provide several intermediate focal plane where alignment or calibration aids can be inserted. In its initial layout all WFSs will be closed loop on the low-order DM and be open-loop with respect to the high-order DM. This arrangement can be used to run SCAO, MOAO, GLAO or LTAO modes, and is illustrated in Fig. 5.1.

The system has be designed to run at close to on-sky rates so that RTCS issues can be investigated. At present the limiting factor on system frame rate is the WFS cameras, which have a maximum frame rate of 200 Hz.

5.2.2 Source Emulation

DRAGON requires natural guide stars, laser guide stars and a science source to be emulated. Four NGS are simulated, one in the centre of the field to be used by a truth WFS and three off-axis sources are mounted in an arrangement of polar coordinate stages, which can be placed in any asterism inside a $3'$ field of view, with stars having a minimum separation of $10''$.

Light sources are generated for each NGS by coupling Light Emitting Diodes (LEDs) to multi-mode optical fibres. The fibre output is then clamped in the required NGS position. Ten sources such as these have been manufactured for this use, as auxiliary sources for alignment purposes and to provide redundancy in case of failure. A science source is emulated in a similar fashion though it is generated by an infra-red laser which is coupled to a single mode fibre, providing a diffraction limited source placed directly adjacent to the on-axis NGS. Fig. 5.2(a) shows a photograph of the NGS and science sources in position.

LGS are emulated in a different manner as the method described above does not give the effects of SH WFS spot elongation and LGS uplink turbulence as required. Instead, LGSs are created in a way analogous to LGS on real observatories. A 532 nm diode laser resides in a dedicated laser launch module, where the beam is formatted to the correct diameter of 1.5 mm, analogous to a beam of 35 cm on a 4.2 m telescope. The beam is split into four independent beams using a Diffractive Optical Element (DOE), which is placed at an optical plane conjugate to the pupil. The beam is then introduced into the system down-stream of

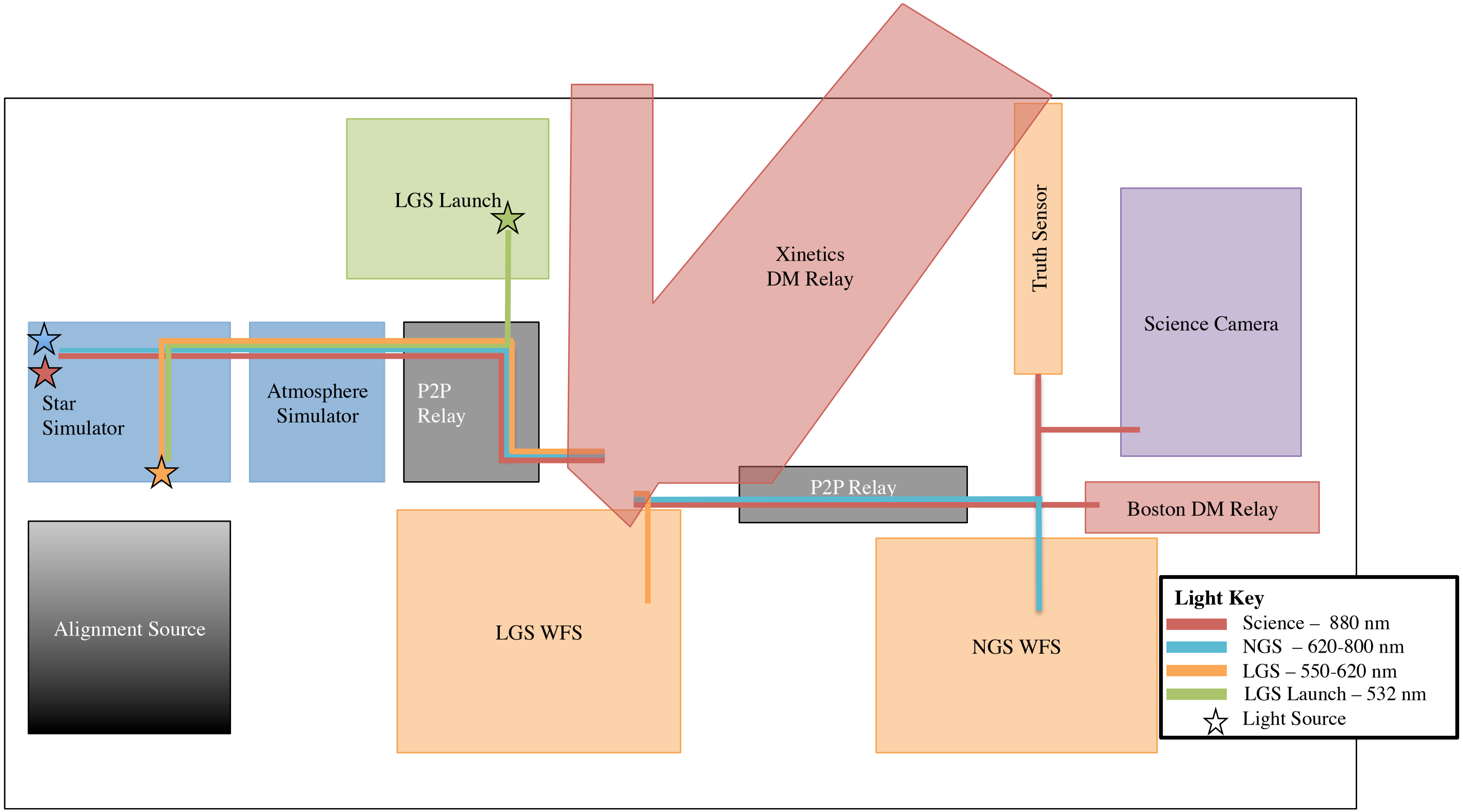

Figure 5.1: The initial DRAGON layout in block diagram form where every block represents a DRAGON module. The lines connecting blocks represent light travelling through the system and are colour coded by wavelength.

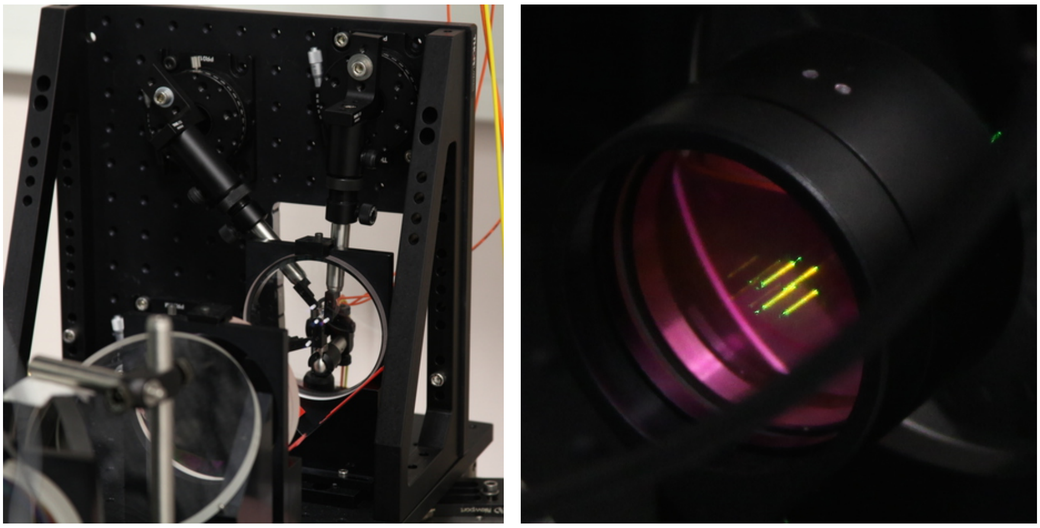

(a) NGS sources (b) LGS dye cell

Figure 5.2: The DRAGON NGS (a) and LGS (b) sources. The NGS are manually configured to create any three star asterism within a $3'$ field. Light is fed from white LEDs into multimode optical fibres which are held in an optical plane conjugate to infinity. The central source is a NIR laser fed single mode fibre to provide a diffraction limited science target, closely positioned next to a multimode, LED fed multimode fibre acting as an on-axis NGS. The LGS are created by projecting the light from a diode laser with a wavelength of 532nm. The beam is split into four by a diffractive optical element before the light propagates up through the turbulence simulation, emulating LGS uplink turbulence. The depth of the cell results in SH WFS spot elongation being built into the system.

the turbulence simulator through a low wavelength pass optical filter. A photograph of the laser launch module is shown in Fig. 5.3.

The 532 nm light propagates upwards through the turbulence and is picked off by an intensity beam-splitter, into a cylindrical cell filled with fluorescent Rhodamine B dye, shown in Fig. 5.2(b). When excited by light at 532nm, the dye fluoresces with a spectrum illustrated in Fig. 5.4. This distribution is centred on a similar wavelength to light emitted by the atmospheric sodium layer when excited by a sodium laser, 589nm. As the distribution is wide, it encroaches into the NGS wavelength band. However, the returned intensity from LGS dye cell is small in comparison to the NGSs and the LGS is defocussed at the NGS WFS focal plane so it does not contaminate the NGS WFS measurements.

The light emitted from the fluorescent cell is used as a guide star for the LGS WFSs. As the cell has a finite depth of dye, the off-axis WFSs will observe an elongated source, as with on-sky sodium LGSs. The depth of the cell defines the depth of the extent of the observed SH spot elongation. Uplink turbulence will also be observed as the beam must propagate up through the turbulence before it encounters the fluorescent cell. A schematic diagram illustrating the LGS configuration is given in Fig. 5.5.

Separation of different light sources is achieved by using different wavelength bands for NGS, LGS and science light. The LGS light wavelength band is defined by the response of the fluorescent dye used in LGS emulation. Peak output is at 590 nm hence the wavelength

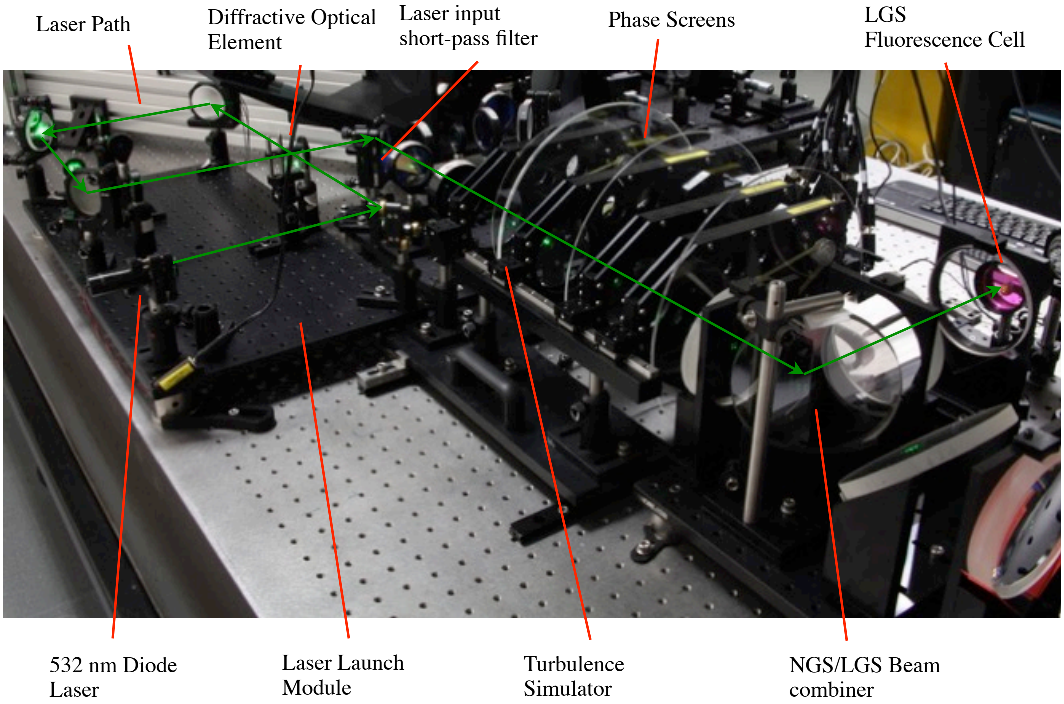

Figure 5.3: An image of the LGS excitation laser propagating up into the LGS dye cell. The laser launch system is on the left of the image where the laser beam is split into 4 beams using a diffractive optical element and is re-imaged to the correction optical conjugate plane for the system. It is injected into the system through a 550 nm cut-off, low-wavelength pass filter placed at a 45° angle which is used as a fold mirror for the down-stream system. Laser light then passes up through the turbulence layers, is picked off by a beamsplitter and enters the LGS dye cell on the right of the image.

band of 550-620 nm is reserved for LGS WFS light. The NGS light is created by white light LEDs and the band used for NGS light is 620-800 nm. The science source is created by a Near Infra-Red (NIR) laser outputting light at 880 nm. Finally, because of the method of generating LGSs, a further narrow band of 532 m exists which the LGS excitation laser inhabits. This laser must be $\approx$ 5 mW to create enough return LGS light and can cause significant backscatter and ghost images throughout the system. To avoid the 532 nm light contaminating other modules, a notch filter removes this scattered light downstream of the launch position. Fig. 5.1 shows how light of each wavelength is picked off throughout the system.

5.2.3 Turbulence Emulation

The turbulence emulator for DRAGON consists of four plastic phase screens, each with phase distortions imprinted. Each screen can rotate independently with variable speed. The lowest altitude screen, corresponding to the ground layer of turbulence, is fixed in altitude but the upper three can translate in height between 2 km and 20 km. Both rotation and altitude translation are driven by stepper motors and controlled remotely. This will be used

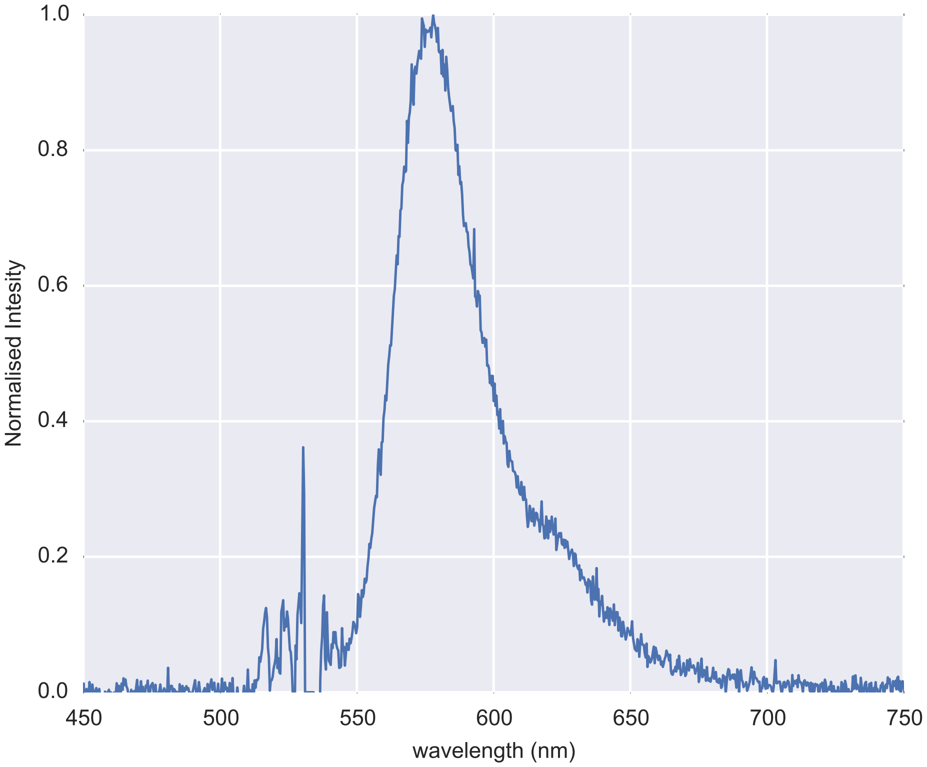

Figure 5.4: The spectrum of light emitted from the Rhodamine dye when excited by light at 532 mn. The peak around 532 nm is caused by some residual light from the excitation laser contaminating the spectrograph.

to emulate turbulent layers in the atmosphere changing altitude during AO operation which will affect tomographic wavefront reconstruction (Gendron et al., 2014).

The ground layer phase screen was purchased from the University of California, Santa Cruz and created using a method pioneered by Rampy et al. (2012). A series of aerosols are sprayed onto a plastic screen in such a way as to create optical phase distortions with statistics approaching that of the atmosphere. A phase plate of diameter 20 cm, with r_0 value measured to be 0.75 mm (17.5 cm "on-sky" when emulating a 4.2 m telescope) has been purchased from the University of California, Santa Cruz for use in DRAGON. This screen is ideal as ground layer turbulence, as is it relatively strong, with a low value or r_0. It is not possible to use it for high layer turbulence, as the diameter is not sufficient to cover the entire field of view.

For upper layer phase screens a novel technique has been utilised to create phase distortions onto a plastic plate. A clear plastic, optical quality plate has been precisely machined to exhibit turbulence by Durham Precision Optics (DPO), a company associated with the CfAI. DPO have previously used a similar technique to create other astronomical optical pieces, such as the image slicers for the KMOS integral field spectrograph (Dubbeldam et al.,

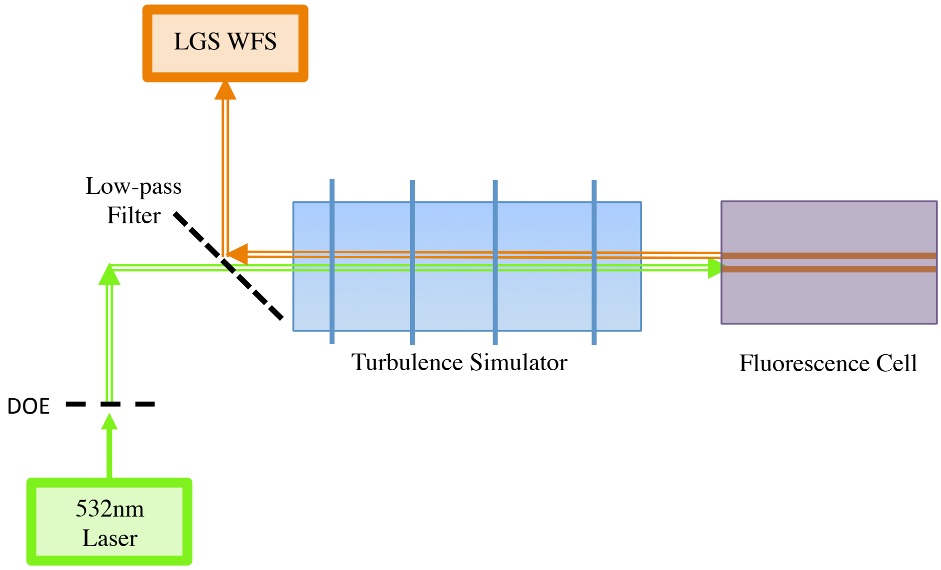

Figure 5.5: A schematic diagram of the LGS emulation system. The laser is split into multiple beams by a DOE, then injected into the system through a wavelength low-pass filter. The beams pass up through the turbulence simulator and into the fluorescence cell, creating four LGSs. Light from these propagates back through the turbulence, and is reflected off the low-pass filter, through DRAGON and eventually to the LGS WFSs.

2012) and NIRSPEC, a spectrograph for the James Webb Space Telescope (JWST) (Purll et al., 2010). Simulated phase data with the required atmospheric statistics was supplied to the diamond machining laboratory, who then used precision machining to cut the phase profile. This is a similar technique to that used by Hippler et al. (2006), where phase distortions are etched onto glass plate, though by diamond machining into plastic, higher phase resolution is possible and the process is significantly less expensive. Initial results from this method of phase screen generation are presented in § 5.4.2.

5.2.4 Wave-Front Sensing

As DRAGON is intended to investigate issues surrounding tomographic AO systems it requires multiple off-axis WFSs. DRAGON features three NGS WFSs, and four LGS WFSs which can be either closed or open loop with respect to each DM. A “Truth Sensor” is also present, which is an on-axis WFS intended to remain closed loop on all DMs and provide analysis of system performance, as well as allowing a SCAO mode of operation. Each WFS is a SH WFS with 31×31 sub-apertures, adhering to the so-called “Fried geometry”, with respect to the 32×32 actuator Boston MEMS DM.

The three NGS WFSs reside in a Target Acquisition System (TAS) which is able to move each WFS to pick-off an NGS anywhere within the DRAGON $3'$ field of view. The NGS and Truth WFSs use Imperx Bobcat 640×480 pixel detectors capable of frame rates up to 200 Hz, only 434×434 pixels are used resulting in 14×14 pixels per sub-aperture. In practice

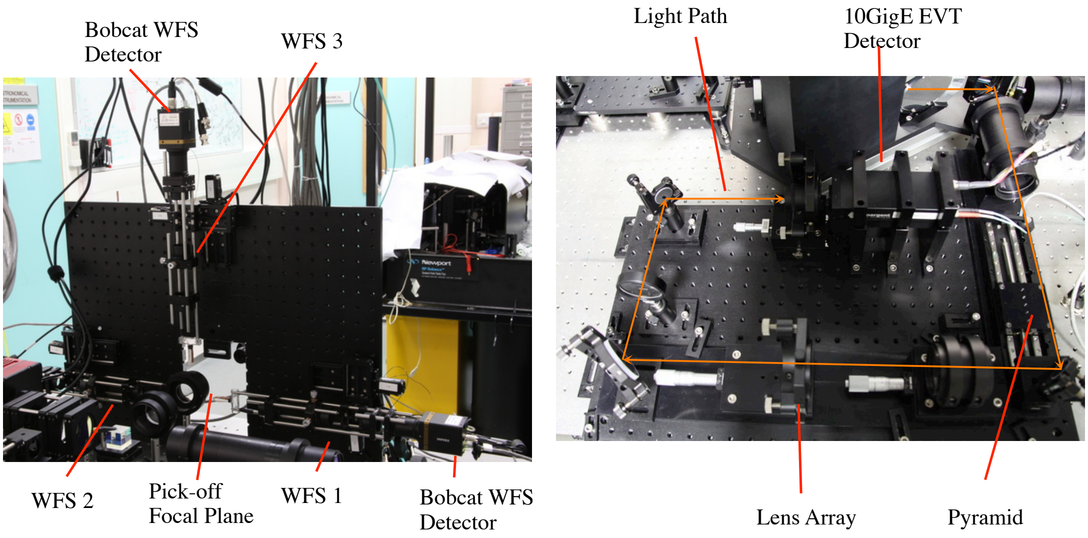

(a) NGS WFSs

(b) LGS WFS

Figure 5.6: The NGS and LGS WFSs are shown in (a) and (b) respectively. NGS WFSs can be moved anywhere in the 3′ diameter field of view to pick off a guide star. The LGSs are formatted such only a single detector is required. The pyramid which alters the LGS separation is not shown in this photograph and will be placed after the lens tube on the top right of the figure.

this can be reduced depending on the AO configuration and turbulence strength, with the remaining pixels acting as "guard" pixels. An image of the completed NGS TAS, with WFSs attached is shown in Fig. 5.6(a), and the SH spot pattern observed on the detector of a NGS WFS shown in Fig 5.7.

Light from the four LGSs is reformatted such that all WFS can be present on one large detector. This is achieved optically through the use of a transmissive optical pyramid to alter the angular separation of the LGSs, a method first implemented on CANARY (Morris et al., 2011). The LGS WFS uses an Emergent Vision Technologies HS-2000, 2048×1088 pixel detector, though a 1024×1024 pixel window is used for the four WFSs. This detector is notable as it features a 10GigE interface which can support extremely high data rates, allowing high speed operation at over 300 Hz, even in full-frame mode with 2048×1088 pixels. The LGS WFS optical system is shown in Fig. 5.6(b) and the four SH spot patterns recorded on the detector shown in Fig 5.8, each sub-aperture contains 8×8 pixels.

5.2.5 Wavefront Correctors

DRAGON features three active elements providing AO correction, the specifications for each is given in Table 5.1. Tip tilt aberration are removed by a PI, high speed, three actuator tip tilt platform. The actuators are arranged in a tripod setup, though for ease of control these are mapped to a more simple x and y scheme in the RTCS. Low order correction is provided by a Xinetics 97 actuator mirror, with a 77.5 mm pupil diameter. The high-order

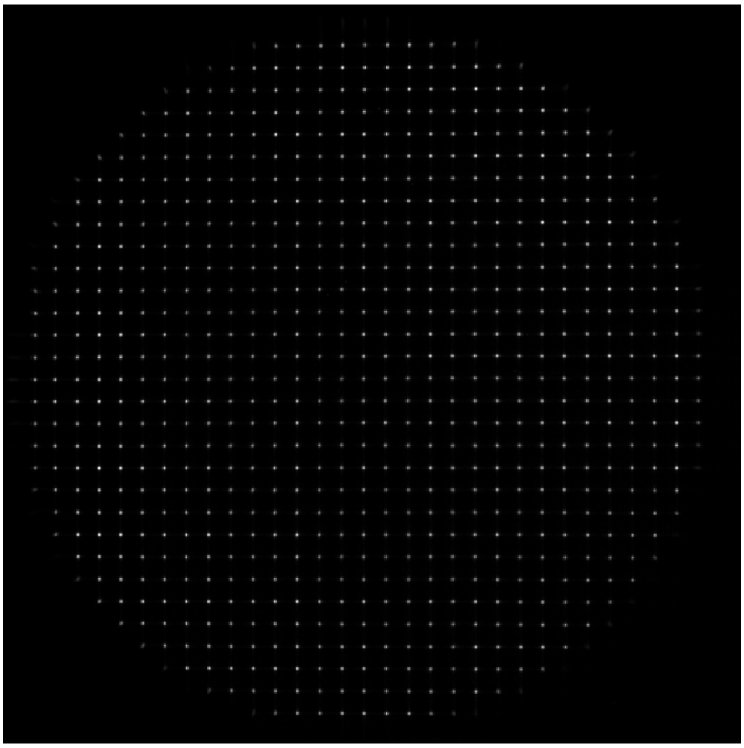

Figure 5.7: 31×31 sub-aperture SH spot pattern recorded on a NGS WFS.

DM is a 1024 actuator Boston MEMS DM, with a 9.3 mm pupil diameter. Both DMs are placed in planes optically conjugate to the system pupil.

To preserve optical quality while magnifying and demagnifying the pupil to the size of the Xinetics DM, a 3-dimensional optical relay has been designed. This approach has been chosen over using a pair of custom manufactured off-axis parabola mirrors for reasons of cost – the current design uses only off-the-shelf optical components making it inexpensive compared to acquiring custom optics. The optical design is shown in Fig. 5.9(a), along with a photograph of the mechanical structure containing it in Fig. 5.9(b). The optical relay for the Boston DM is an on-axis design which uses a polarising beamsplitter and quarter wave plate combination to avoid excessive loss of throughput. The DM is shown in Fig. 5.10(b).

In its initial configuration, DRAGON will implement a Woofer-Tweeter correction system, where the Xinetics DM is used to correct for powerful, low spatial order optical aberrations and the Boston DM corrects for weaker high-order residual aberrations. This is required as MEMS DMs do not have a high enough maximum stroke to correct for low order aberrations.

Correction from the tip-tilt and low-order DM is observed by the NGS, LGS and truth

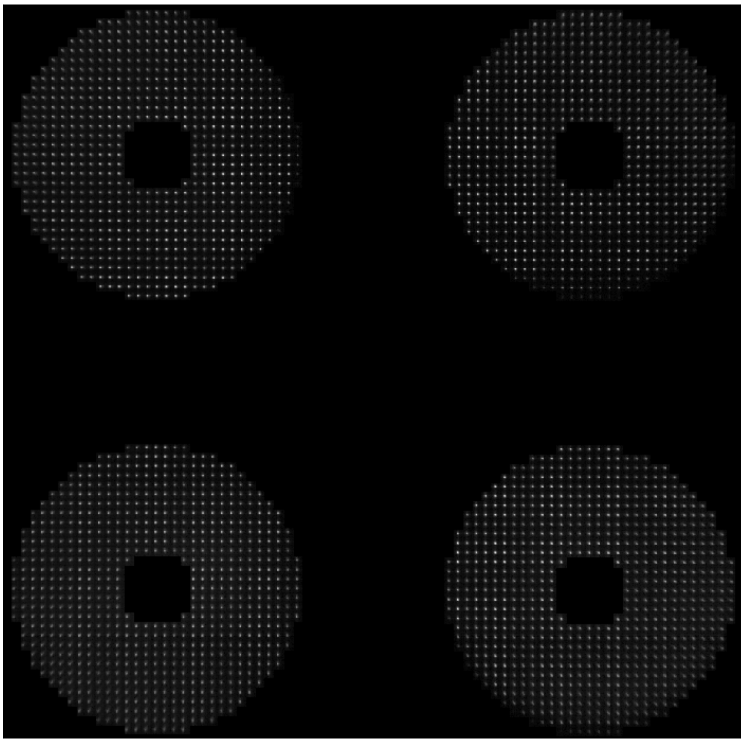

Figure 5.8: The four 31×31 sub-aperture SH spot patterns on the LGS WFS detector.

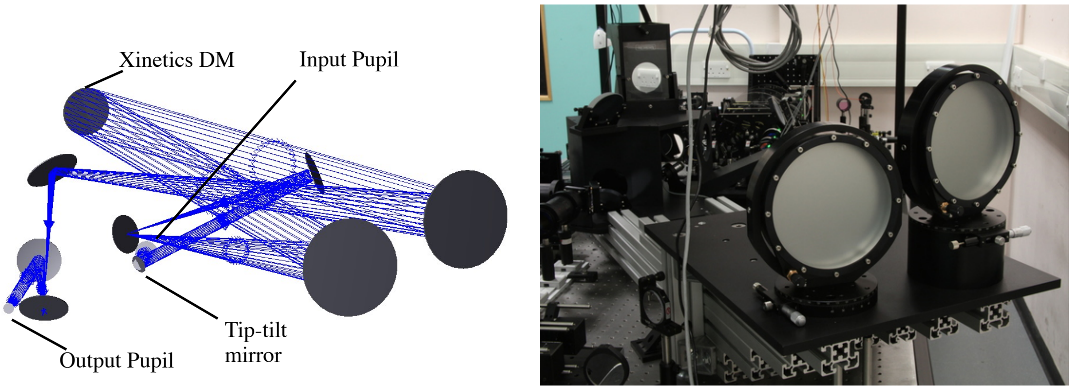

(a) Xinetics DM optical relay design

(b) Xinetics DM Mechanics

Figure 5.9: The Xinetics DM relay optical design, (a), and mechanical construction, (b). To ensure wavefront quality is preserved without requiring expensive custom off-axis parabola, a 3-dimensional pupil to pupil magnification and de-magnification relay has been designed and constructed. The tip-tilt mirror also resides in the Xinetics relay mechanical train at an optical plane conjugate to the system pupil.

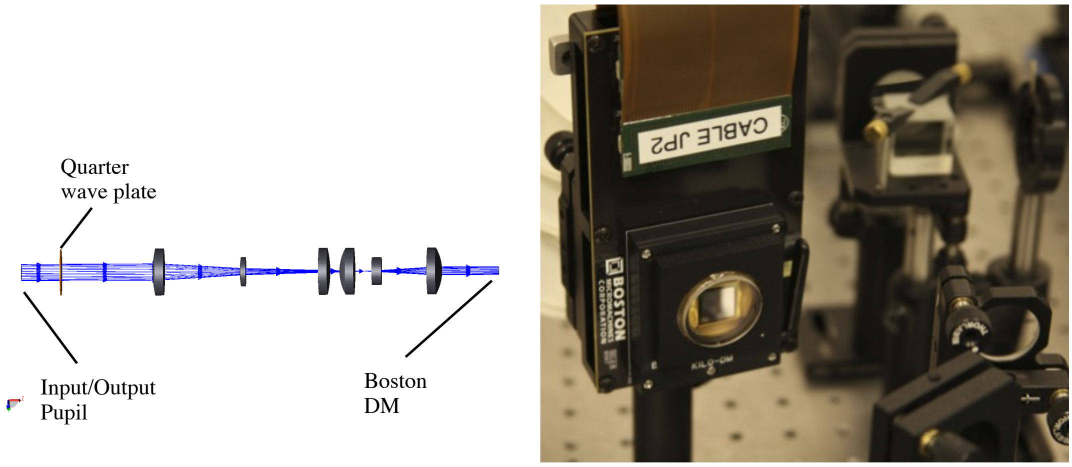

(a) Boston Optical Relay (b) Boston DM

Figure 5.10: The Boston DM optical relay (a) and the Boston DM (b). A reflective relay is used to format light onto the DM. It is on-axis and uses a polarising beam splitting cube (not shown) to pick-off and then merge light to and from the DM. Polarisation is exploited to reduce loss of throughput using a quarter wave plate.

	Tip-tilt	Low order	High Order
Actuators	3 (mapped in software to 2)	97 (11×11)	1024 (32×32)
Manufacturer	Physikinstrument	Xinetics	Boston
Actuator technology	Piezo electric	Piezo electric	MEMS
Aperture diameter (mm)	25	77.5	9.3
Max stroke (µm)	30	4	1.5
Resolution (nm)	0.5	0.122	0.09
Max frame rate (kHz)	1	5	34
Inter-actuator coupling	0	<10%	15%
Actuator hysteresis	Unknown	1%	0%

Table 5.1: Key specifications of the DRAGON wavefront correctors.

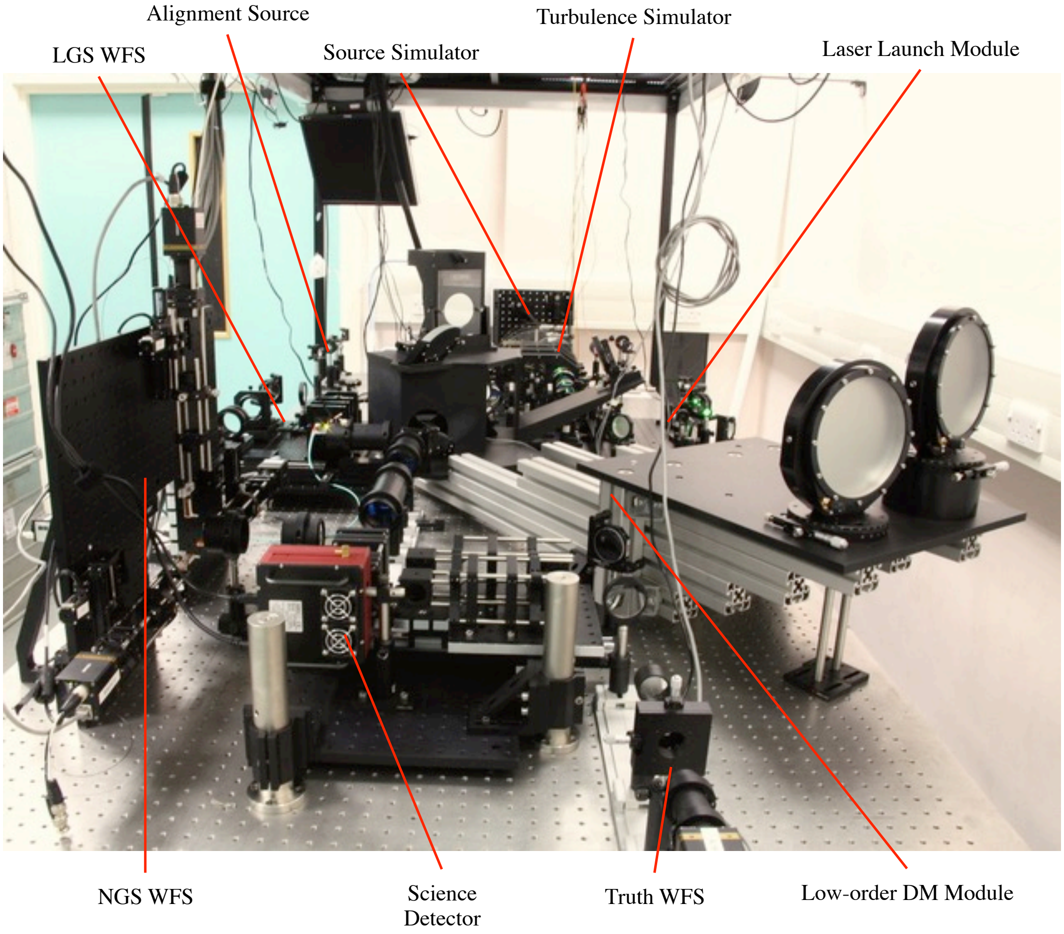

Figure 5.11: A view of DRAGON with all currently constructed modules in place. The source and turbulence generation are at the far end of the image, and science and truth sensor in the foreground.

WFSs, whilst the correction from the high-order DM is only observed on the truth sensor. This arrangement of DMs is similar to that which could be used on telescope featuring a deformable secondary mirror, such as the VLT AO facility or the European Extremely Large Telescope (E-ELT) (Manetti et al., 2014; Tamai and Spyromilio, 2014). The deformable secondary mirror may be used to perform low order or GLAO correction. The other DM(s) later in the optical train provide high-order or direction specific correction (Cuby et al., 2008).

5.2.6 Science Imager

A science imager is present in DRAGON in order to analyse the corrected Point Spread Function (PSF). For this analysis, a telephoto system has been designed which samples the on-axis PSF at four times the Nyqvist sampling ratio. The science imager also has a wide-field mode which can be used for acquisition and a basic assessment of wide-field performance, though resolution is not high enough for PSFs to be Nyquist sampled. The science detector used is an SBIG STF-8300 detector, which has 3326x×2504 pixels, with a minimum exposure time of 0.1 s. The science detector and its two optical paths corresponding to wide and narrow field modes of operation are shown at the bottom of Fig. 5.11.

5.3 Software

5.3.1 Real-time Control System

DRAGON uses the Durham Adaptive optics Real-time Controller (DARC) RTCS, described in detail by Basden et al. (2010). The core of DARC is CPU based and is highly parallelised for high performance. As it is not tied to specific hardware, it is very flexible and portable and GPU based algorithms are currently under development for ELT scale operation (Dipper et al., 2013). Once complete, these can be tested on DRAGON to ensure the provide the expected performance.

DARC currently runs on a server class computer, with dual, six core, Intel Xeon E5645 processors, giving a total of 12 physical processing cores. Using this system, DARC is capable of running all eight DRAGON WFSs at a frame rate of 200 Hz, including application of camera calibration frames, WFS centroiding, and wavefront reconstruction for all three wave front correctors. This represents a control matrix of size 11264 WFS measurements × 1122 DM commands.

The computational load is comparable to the current highest spatial order systems. Palm 3000 for example, computes a control matrix of size 8192×3388. However, pixel processing is far more taxing in DRAGON, as each sub-aperture is composed of up to 14×14 pixels, whereas Palm 3K uses quad-cells (Truong et al., 2012). This makes DRAGON by far the most computationally intensive AO system built to date. Future ELT scale systems will be larger. The E-ELT WFSs will be of order 84×84 sub-apertures, and DMs of order 85×85, so a computational load similar to ELT scale SCAO can begin to be approached using DRAGON (Basden et al., 2010). Unfortunately, ELT scale tomographic real-time control demonstrations, which require many WFSs and DMs of this size, are still out of reach.

5.3.2 Control Software

Whilst DARC provides a low-level interface to some DRAGON components and the RTCS, one goal of DRAGON is to simplify control software for tomographic AO systems. To this end, an Application Programming Interface (API) has been created using the Python programming language for control of the entire bench. Control for each component is represented as a Python object, with associated methods and attributes, for instance a WFS object contains a method to set the centroiding algorithm. This presents an intuitive interface to set low-level commands. Higher level functions for processes, such as measuring the interaction matrix, make use of these objects, making code all through the project simple and quickly understandable. Further to this, Graphical User Interfaces (GUIs) are planned which will make use of these higher level functions.

Standards for the project, such as coding style and documentation, have been enforced at all levels making the software equally usable for experienced AO scientists, who may make use of the low-level interface and AO beginners, who may prefer to use the high layer functions and GUIs. For processes which take place on remote machines, such as mechanical control, the relevant Python objects are served over Python Remote Objects (Pyro)*. Pyro is a tool which allows a python object to appear on a local machine with access to its methods and attributes, though code is executed on the remote machine.

As of March 2015, the low-level interface is close to complete and planning has begun for the GUIs. The author of this thesis has been closely involved with the design of this project and has contributed code to all sections of the software.

5.4 Integration Results

5.4.1 Current State of DRAGON

As of spring 2015, DRAGON is approaching completion. All sources are now in place including the novel form of LGS emulation. NGS, LGS and the truth WFSs have been constructed as well as the low-order DM relay, containing the tip-tilt mirror. The science imager has also been aligned and integrated into the system. The only remaining mechanical module yet to be completed is the high-order DM which is currently being assembled. Though the WFSs and low-order DM are in place, correction in either tomographic or SCAO modes is yet to be perfected. Consequently, integration results given in this section use only uncorrected WFS data.

5.4.2 Precision Machined Phase Screen Analysis

Two prototype machined phase screens have thus far been created using the method described in § 5.2.3. The initial prototype suffered from excessive vibration during the machining process, causing large tooling marks to be present on the screen surface and was hence deemed unsuitable for use in DRAGON. These issues have been mitigated for the creation of the second screen and investigations into its use as an optical turbulence emulation are presented here.

The measured temporal power spectra of the turbulence is a good gauge of its statistical properties, as theoretical spectra are well known. Conan et al. (1995) determined the theoretical temporal power spectrum of measurements of atmospheric turbulence when using a variety of instruments, including the SH WFS. It is shown that if Kolmogorov turbulence statistics are assumed then the temporal power spectra of the gradients measured by the WFS in the same direction as the movement of the turbulent layer will show a power law with a gradient of $-11/3$.

The temporal power spectrum of the machined phase plate as measured by the DRAGON on-axis truth WFS is plotted in Fig. 5.12. The gradient of the spectrum has been measured using only data in the linear region observed for low temporal frequencies using a chi squared

---

[*] `http://pythonhosted.org//Pyro/`

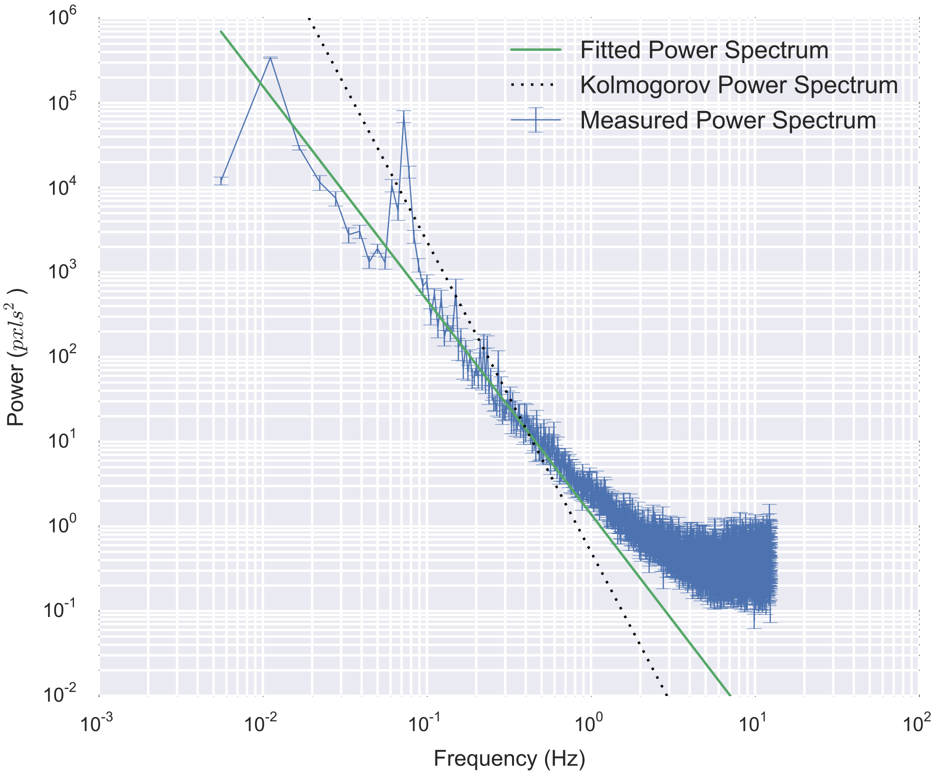

Figure 5.12: The WFS slope temporal power spectrum of the diamond machined phase screen measured from the DRAGON truth WFS. The blue curve showing error bars is the measured power spectra, the green solid line is the fitted theoretical power spectra, and the dotted black line the Kolmogorov power spectra with gradient 11/3.

analysis. The flattening out of the spectrum at high frequencies is due to the noise floor of the detector, these values are ignored when fitting the spectrum gradient.

The measured power law does not adhere to that predicted for Kolmogorov turbulence, as it shows a gradient of (-2.53 ± 0.18), or approximately $-7.6/3$. Instead, it shows a shallower gradient, resulting in more power in high-spatial modes, and less in low modes. Though the screen does not show Kolmogorov statistics, a shallower power spectrum is not inconsistent with measured power spectra from real AO systems observing atmospheric turbulence (Rampy et al., 2012).

Aside from the measured power spectra, very large scale, powerful tip-tilt modes have been noticed to be present on the phase screen. It is thought that these are a result of warps in the plastic from the machining process and their reduction will be sought in subsequent phase screen prototypes. Unfortunately, these make the phase screen unsuited for experiments sensitive to tip-tilt, such as the LGS uplink retrieval method described in this thesis.

Given that the temporal power spectrum has been measured to be consistent with real at-

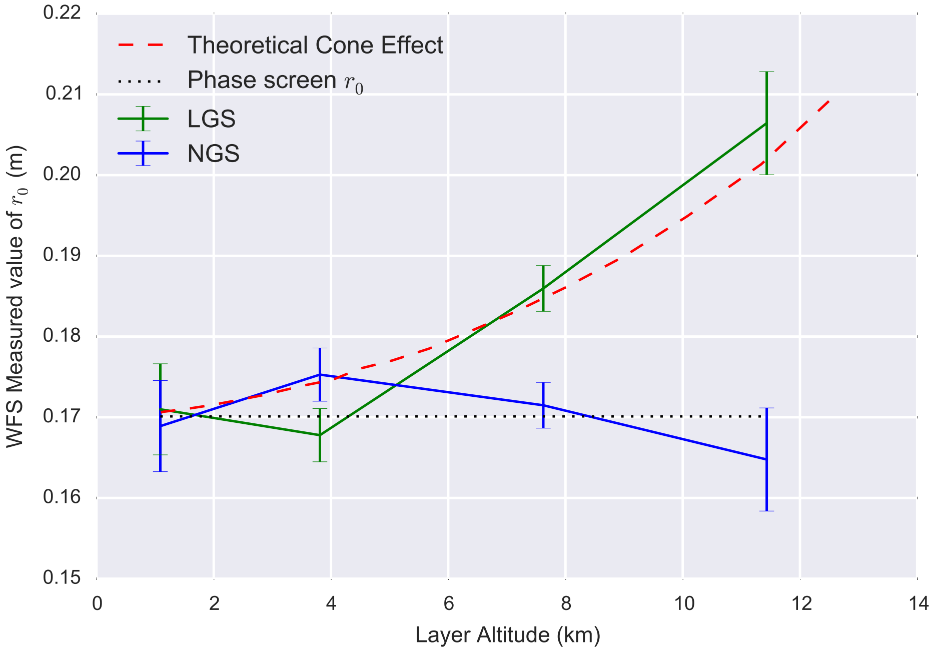

Figure 5.13: The integrated seeing strength in terms of the Fried parameter, r_0, observed by a NGS WFS (lower, green curve) and a LGS WFS (upper blue curve). The dashed red curve illustrates the value of r_0 predicted by a theoretical analysis performed by Tyler (1994), and the dotted is the mean measured value of r_0 by the NGS.

mospheric turbulence, the screen is deemed suitable for further experiments with DRAGON for which accurate tip-tilt emulation is not required. Work will continue to create further phase screen prototypes with a power spectra closer to that predicted by Kolmogorov for use in DRAGON as well as other applications within AO.

5.4.3 Laser Guide Star Emulation

DRAGON will be used for a variety of studies involving LGS AO, so it is important to ensure that they are emulated accurately. Focus anisoplanatism, or cone effect, describes how a LGS incompletely senses turbulence at altitudes higher than the ground layer, and has been described in § 2.3.6.2. In DRAGON, cone effect has been investigated by measuring the observed strength of a single turbulence layer, positioned at a number altitudes, by both an NGS WFS and a LGS WFS. When the layer is at high altitudes, the LGS WFS only observes a sub-pupil, smaller than the telescope pupil, which is effectively expanded to the telescope pupil size. It is expected that this will result in a smaller value of the integrated seeing strength on the LGS WFS.

The measured seeing strength for a NGS WFS and a LGS WFS with increasing turbulence altitude is plotted in Fig. 5.13. The NGS WFS measures approximately the same value of r_0 for each phase screen altitude, this mean value NGS is plotted as the dotted black line.

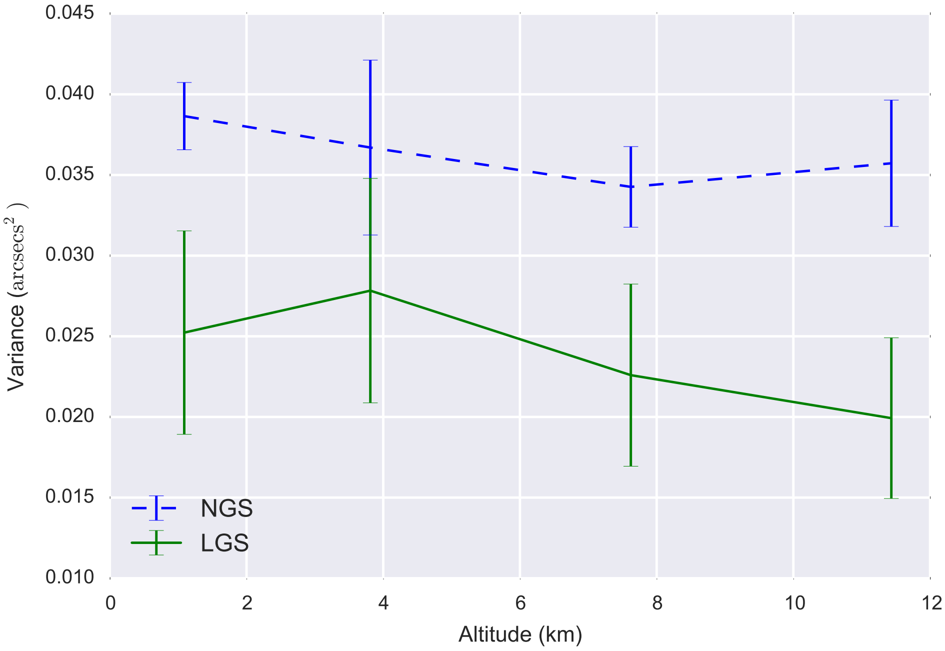

Figure 5.14: The variance of measured tip tilt on an on-axis DRAGON LGS WFS and the DRAGON truth WFS. The discrepancy between the observed values is a result of the laser passing up through the turbulence before forming a guide star.

The seeing strength measured by the LGS reduces (i.e. r_0 increases) with increasing phase screen altitude as predicted by Fried and Belsher (1994), due to the cone effect. These early data sets are in agreement with theoretically derived values, illustrated by the red dashed curve (Tyler, 1994).

The effect of the LGS travelling up through the turbulence is manifested by global tip-tilt measurements on the LGS WFS as the LGS beacon jitters. Fig. 5.14 plots the tip-tilt variance across both the NGS WFS and the LGS WFS observing on-axis, with increasing phase screen altitude. For all altitudes, the variance of the LGS is different to that of the NGS. This effect increases with increasing altitude due to a combination of cone effect and the reduced uplink propagation distance between the turbulence layer and the emulated sodium layer. The discrepancy between the measured tip-tilt variance shows that the LGS emulation is performing as expected.

The fact that the LGS shows lower variance than the NGS was not expected. It is shown in §6.2 that the tip-tilt across the LGS launch path is almost uncorrelated with that across the telescope aperture, so it was predicted that including uplink tip-tilt would increase the measured variance. It is likely that the deviation from this prediction is due to the large tip-tilt modes which have been observed on the machined phase screen.

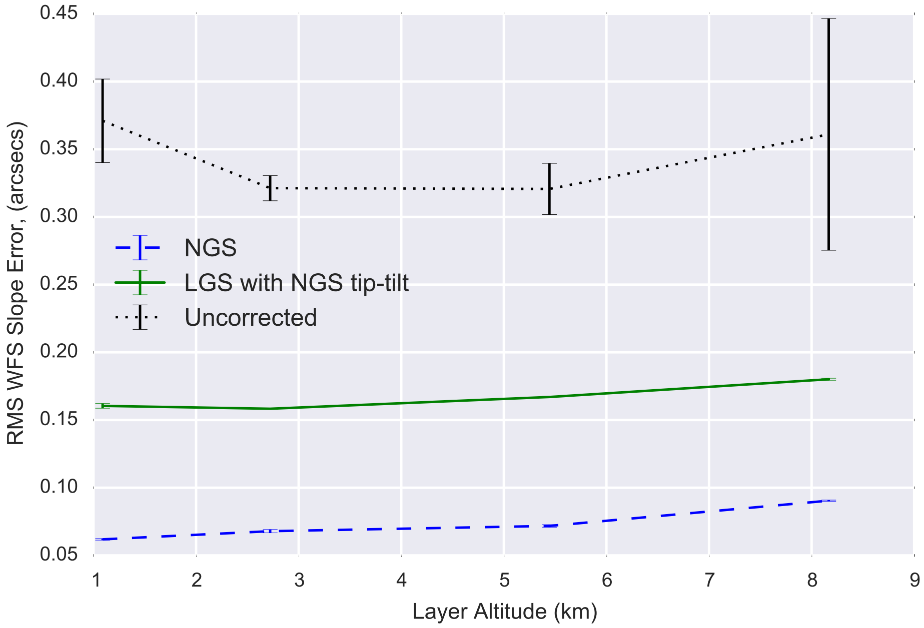

Figure 5.15: Results from tomographic reconstruction from DRAGON, showing the error in reconstructed on-axis slopes compared to the truth sensor measurements against the altitude of a single turbulence layer.

5.4.4 Tomography

Early results demonstrating the tomographic capabilities of DRAGON are plotted in Fig. 5.15. NGS and LGS tomographic reconstructors have been created using the Learn and Apply method described in § 2.4.2.2, though fitting to analytically derived covariance matrices has not yet been performed so they are created using only the raw "learn" slopes. This will not give optimal performance, however they can be used to prove that some tomographic reconstruction is taking place.

After the tomographic reconstructor has been created, off-axis WFS measurements are used to predict the on-axis truth sensor WFS measurements, and the error compared to the measured truth sensor measurement is calculated. Results are quoted as WFS slope error to reduce the impact of any reconstruction error and can be compared to the uncorrected truth sensor slopes measurements. This analysis has been performed with a single turbulence layer placed at different altitudes.

Fig. 5.15 shows that both the NGS and LGS based tomographic reconstruction has been successful in predicting the on-axis slope measurements. The quality of tomographic on-axis slope prediction decreases as the layers altitude increases. This is expected as tomographic reconstruction error increases as less WFS sub-apertures overlap. The NGS performs noticeably better than the LGS. This is likely due to different noise levels on the two WFS types. Each NGS has a maximum flux level of ≈ 800 counts, with a noise floor of ≈ 20. On the other hand, the LGS has a maximum flux of ≈ 50 counts, and the detector a noise floor of ≈ 20. The possibilities of using a more powerful laser to illuminate the LGS dye cell is currently under consideration to increase the LGS flux.

5.5 Summary

This chapter has described DRAGON, an AO laboratory test bench with many novel features. DRAGON can use up to three off-axis NGS WFSs, four LGS WFSs and a single on-axis truth WFS to perform a variety of AO correction modes, including LTAO, MOAO and SCAO. Correction is performed by three wavefront correctors, a tip-tilt mirror, a low-order DM and a high-order DM which can be arranged open or closed loop of the WFSs. All of these components are capable of running at real-time frame rates comparable to on-sky AO systems.

The laboratory bench possesses a unique method of emulating LGS. This makes it the ideal test bed for exploring the potential of the LGS uplink tip-tilt retrieval method which is presented in § 6. Data from the integration of DRAGON has been presented, including initial data using a new method of phase screen manufacture. The method of LGS generation has also been investigated and shown to be appropriate for emulating on-sky LGS.

Chapter 6

LGS Uplink Tip-Tilt Prediction

6.1 Introduction

For the reason discussed in § 2, the use of Laser Guide Stars (LGSs) in Adaptive Optics (AO) has greatly increased the area of the sky available for consistent AO correction. This has led to a vast increase in the number of astronomical science targets which can be observed using AO.

Unfortunately, the laser experiences turbulence whilst traveling upwards to form an artificial guide star so its position will jitter in the sky unpredictably. It is thought that this effect renders all "tip-tilt" information gained from a LGS Wavefront Sensor (WFS) useless, as it is a function of LGS uplink jitter and the desired "downlink" tip-tilt which are entangled irretrievably. It has even been suggested that the tip-tilt the laser acquires on the uplink is the same as the global tip-tilt on the downlink path, hence little tip-tilt will be observed on the WFS at all (Johnston and Welsh, 1994). To correctly obtain the science path tip-tilt, a Natural Guide Star (NGS) must still be used, limiting the sky-coverage of a LGS AO system

In this chapter a method is described to retrieve LGS uplink information, which can be fed back into the reconstruction providing higher correction performance with either LGSs alone or NGSs further from the science target. By reducing requirements on a NGS or eliminating the need for it completely, it is aimed that AO corrected sky coverage can be increased or full sky coverage is achieved for some astronomical applications.

If the tip-tilt modes measured across the full aperture are the same as those across the beam launch aperture, it is clear that the tip-tilt signal would indeed be irretrievable from LGS WFS, as they would be fully reciprocal and no atmospheric tip-tilt would be observed. In § 6.2, it is shown that this is not the case. The tip-tilt modes across the beam launch telescope are uncorrelated with those over the whole aperture, opening the possibility of LGS uplink tip-tilt determination. The algorithm for uplink tip-tilt prediction is derived in § 6.3 and an adaptation to the Learn and Apply algorithm, proposed by Vidal et al. (2010) for Multi-Object Adaptive Optics (MOAO), is suggested as a practical method for its use. Finally, the applications and limitations of such an AO system are discussed in § 6.5.

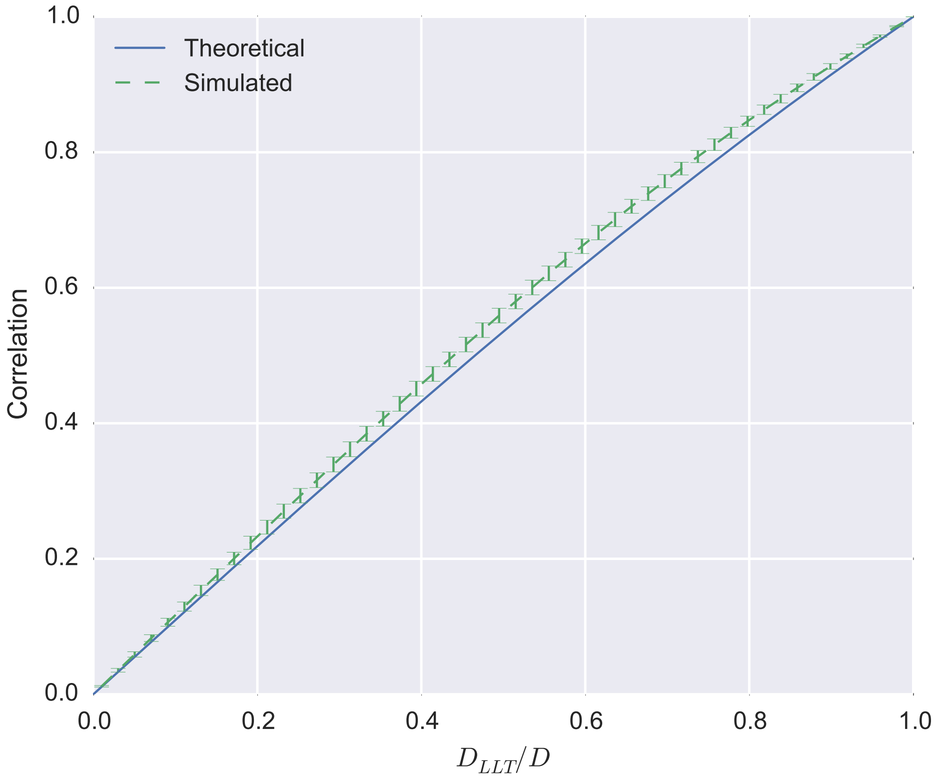

Figure 6.1: Theoretical correlation of phase perturbations in Kolmogorov turbulence between concentric tip-tilt modes as a function LLT diameter, D_{LLT}, as a fraction of the telescope diameter, D. The correlation is also shown within simulated Von Kármán phase screens.

6.2 Correlation of Tip-Tilt Between Telescope and Beam-Launch Apertures

If the global tip-tilt across the telescope aperture is identical to that over the beam launch telescope, any tip-tilt encountered by the LGS uplink path will have an equal but opposite effect on the return path. Consequently no tip-tilt would be observed on the LGS WFS and the tip-tilt component of the science path could not be determined by that WFS. This is referred to as tip-tilt "reciprocity" and is certainly the case if the laser is launched from the full aperture of the telescope, as was suggested for early LGS AO systems (Belen'kii, 1994). However, all current facility LGS AO systems use a separate Laser Launch Telescope (LLT) and on these telescopes and those planned for the future, $D_{LLT} << 0.1D$, where D_{LLT} denotes the diameter of the LLT and D is the size of the telescope aperture.

Prediction of LGS uplink tip-tilt can only be possible if the uplink and downlink tip-tilt components are uncorrelated or it will not be fully observed by the WFS. The covariance between two concentric Zernike modes of different radii in Kolmogorov turbulence is shown in Eq. 6.1 (Wilson and Jenkins, 1996).

$$\mathrm{C_{ij}} = 0.0145786 e^{\frac{1}{2} i\pi(n-p)} \sqrt{(n+1)(p+1)} \left(\frac{R}{\mathrm{r_0}}\right)^{5/3} \times \int_0^\infty dk \frac{J_{n+1}(2\pi k) J_{p+1}(2\pi\gamma k)}{\gamma k^{14/3}} \tag{6.1}$$

where γ represents the fractional size relationship between the two apertures, n and p are the radial orders of the two Zernike polynomials, R is the radius of the telescope and r_0 is the atmospheric Fried parameter (Fried, 1966). This relationship is plotted for concentric tip-tilt modes ($n, p = 1$) of different radii in Fig. 6.1. The correlation of tip-tilt modes in many simulated random Von Kármán phase screens is also plotted. These simulated screens are produced using an identical algorithm to those used for the simulation described in § 4.

It is evident that the correlation of tip-tilt modes between small and large apertures in the regime where $D_{LLT}/D < 0.1$ is less than 0.1 and are hence almost uncorrelated. This result means that tip-tilt modes will not be reciprocal and will be visible on a LGS WFS. Measured tip-tilt will be some function of the turbulence encountered by the laser as it propagates up to form an artificial guide star and the global tip-tilt across the telescope aperture as it propagates down.

6.3 Tomographic Laser Guide Star Tip-Tilt Prediction

6.3.1 Retrieving downlink Turbulence Induced Slopes

As shown in the previous section, the measurement from a LGS WFS is a function of the atmospheric turbulence the laser propagates through on the way up to form a guide star and the turbulence the return light propagates through as it travels back down to the telescope. For AO correction of a natural astronomical science target the two components must be separated and only the latter is required. If using a Shack-Hartmann (SH) WFS, measurements will be in the form of slopes representing the gradients of the measured phase within any given sub-aperture, the use of a SH WFS is assumed in the following derivations. The slopes measured by a LGS WFS can be expressed as the sum of the laser uplink induced slopes and the downlink turbulence induced slopes,

$$\mathbf{\tilde{s}} = \mathbf{\tilde{s}_l} + \mathbf{\tilde{s}_t} \tag{6.2}$$

where $\mathbf{\tilde{s}}$ is a vector representing the slopes measured on a WFS, $\mathbf{\tilde{s}_l}$ is a vector representing the component of the slopes caused by LGS uplink turbulence and $\mathbf{\tilde{s}_t}$ is a vector representing component of the slopes caused by downlink turbulence. For AO correction of a natural astronomical science target it is $\mathbf{\tilde{s}_t}$ that must be obtained. Note that we assume that the LGS uplink turbulence results exclusively in tip-tilt modes being observed on the WFS and no higher order spatial modes, so $\mathbf{\tilde{s}_l}$ will be homogeneous for x and y-gradients. For an AO system with a single LGS and no external reference, determining $\mathbf{\tilde{s}_t}$ is not possible as there is not enough information to determine $\mathbf{\tilde{s}_l}$. In a multi-WFS system, there is more information about the turbulence sampled by the LGSs on the uplink, and $\mathbf{\tilde{s}_t}$ can be computed.

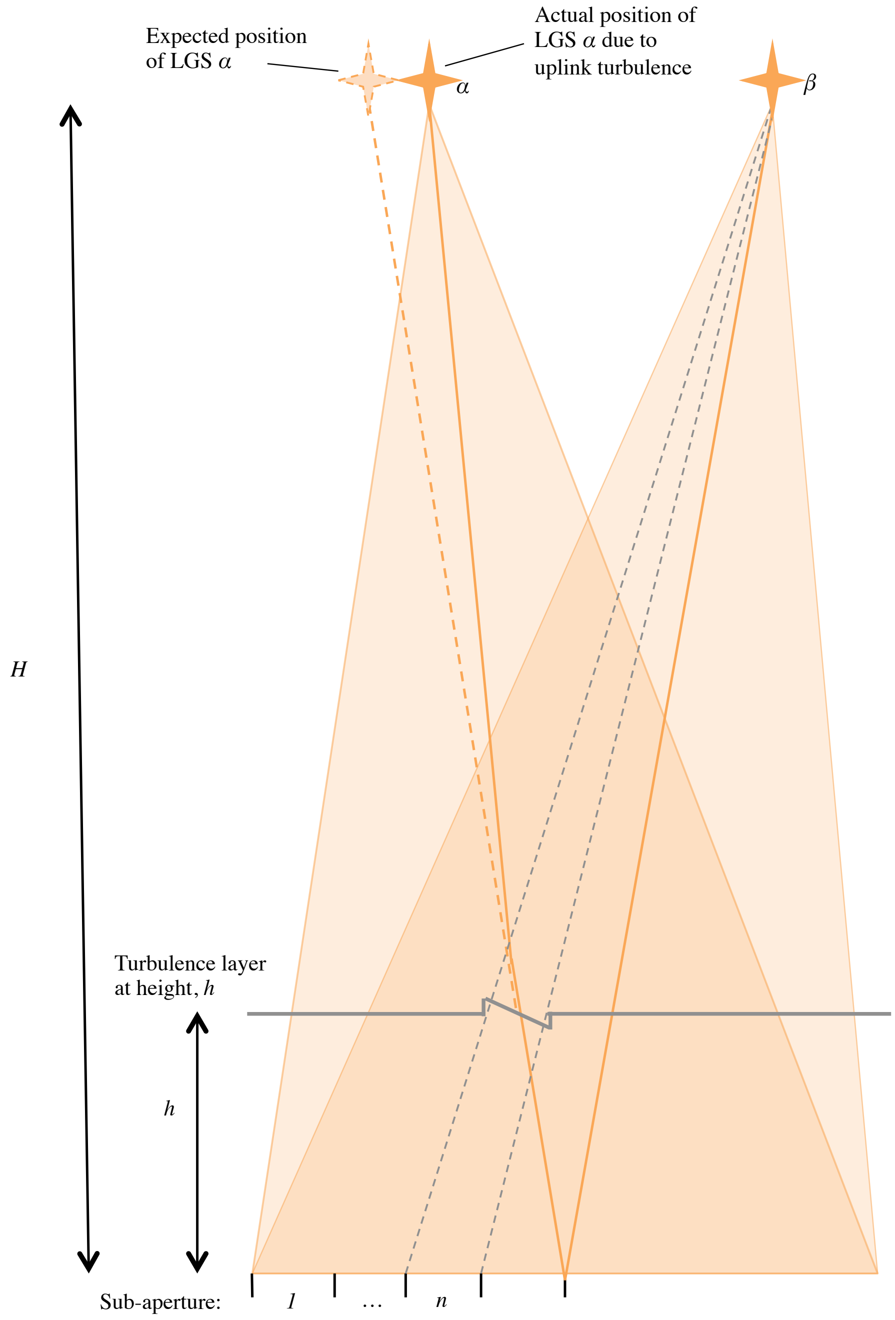

Figure 6.2: The geometry of LGS system under consideration. One turbulent layer is shown, which shows only a tilt at the point that LGS α overlaps with the field of view of sub-aperture n on WFS β.

A trivial 2-dimensional tomographic two LGS AO geometry, where both LGSs are centre-launched is considered, and is illustrated in Fig. 6.2. The following approach can be scaled to many more centre launched LGSs, though the mathematics quickly becomes cumbersome with three or more LGSs. The LGSs are labeled LGS α and LGS β and the observing WFSs as WFS α and WFS β respectively. The slopes measured on WFSs are denoted as $\tilde{\mathbf{s}}_\alpha$ and $\tilde{\mathbf{s}}_\beta$.

WFS β observes the area of turbulence which causes the uplink tilt on WFS α, hence we postulate that there is a transform $\hat{\mathbf{T}}_{\alpha\beta}$ which relates the downlink turbulence induced slopes, $\tilde{\mathbf{s}}_{\beta\mathbf{t}}$, to uplink induced tip-tilt measured on WFS α, $\tilde{\mathbf{s}}_{\alpha\mathbf{l}}$,

$$\tilde{\mathbf{s}}_{\alpha\mathbf{l}} = \hat{\mathbf{T}}_{\alpha\beta}\tilde{\mathbf{s}}_{\beta\mathbf{t}} \tag{6.3}$$

Initially, only a single turbulence layer at a height h is considered which features only a tilt in the section where LGS α overlaps with the field of view of sub-aperture n on the WFS observing LGS β. For this simple case, illustrated in Fig. 6.2, WFS β is unaffected by uplink turbulence so $\tilde{\mathbf{s}}_{\beta\mathbf{l}} = 0$, and $\tilde{\mathbf{s}}_\beta = \tilde{\mathbf{s}}_{\beta\mathbf{t}}$ hence $\tilde{\mathbf{s}}_{\alpha\mathbf{l}} = \hat{\mathbf{T}}_{\alpha\beta}\tilde{\mathbf{s}}_\beta$. The transform $\hat{\mathbf{T}}_{\alpha\beta}$ can easily be determined geometrically by considering the altitude of the turbulence layer, and the positions of the LGSs.

In general however $\tilde{\mathbf{s}}_{\beta\mathbf{t}}$ will not be known, as such a simple turbulent layer is unlikely, so LGS β will also experience uplink tip-tilt motion. For this general case, the transform $\hat{\mathbf{T}}_{\alpha\beta}$ can be applied to the measured slopes, $\tilde{\mathbf{s}}_\beta$

$$\hat{\mathbf{T}}_{\alpha\beta}\tilde{\mathbf{s}}_\beta = \hat{\mathbf{T}}_{\alpha\beta}(\tilde{\mathbf{s}}_{\beta\mathbf{t}} + \tilde{\mathbf{s}}_{\beta\mathbf{l}})$$

recalling the definition of $\hat{\mathbf{T}}_{\alpha\beta}$ in Eq.(6.3),

$$\hat{\mathbf{T}}_{\alpha\beta}\tilde{\mathbf{s}}_\beta = \tilde{\mathbf{s}}_{\alpha\mathbf{l}} + \hat{\mathbf{T}}_{\alpha\beta}\tilde{\mathbf{s}}_{\beta\mathbf{l}} \tag{6.4}$$

The same operation can be applied for the other WFS,

$$\hat{\mathbf{T}}_{\beta\alpha}\tilde{\mathbf{s}}_\alpha = \tilde{\mathbf{s}}_{\beta\mathbf{l}} + \hat{\mathbf{T}}_{\beta\alpha}\tilde{\mathrm{s}}_{\alpha\mathrm{l}} \tag{6.5}$$

We now have two equations, Eq. (6.4) and Eq. (6.5), to solve for two unknowns, $\tilde{\mathbf{s}}_{\alpha\mathbf{l}}$ and $\tilde{\mathbf{s}}_{\beta\mathbf{l}}$. Re-arranging (6.5),

$$\tilde{\mathbf{s}}_{\alpha\mathbf{l}} = \hat{\mathbf{T}}^{\mathbf{-1}}_{\beta\alpha}(\hat{\mathbf{T}}_{\beta\alpha}\tilde{\mathbf{s}}_\alpha - \tilde{\mathrm{s}}_{\beta\mathrm{l}}) \tag{6.6}$$

and substituting into (6.4),

$$\begin{aligned}\hat{\mathbf{T}}_{\alpha\beta}\tilde{\mathbf{s}}_\beta &= \hat{\mathbf{T}}^{\mathbf{-1}}_{\beta\alpha}(\hat{\mathbf{T}}_{\beta\alpha}\tilde{\mathbf{s}}_\alpha - \tilde{\mathrm{s}}_{\beta\mathrm{l}}) + \hat{\mathbf{T}}_{\alpha\beta}\tilde{\mathrm{s}}_{\beta\mathrm{l}} \\ &= \tilde{\mathbf{s}}_\alpha + (\hat{\mathbf{T}}_{\alpha\beta} - \hat{\mathbf{T}}^{-1}_{\beta\alpha})\tilde{\mathrm{s}}_{\beta\mathrm{l}} \end{aligned} \tag{6.7}$$

Finally, re-arranging for $\tilde{\mathbf{s}}_{\beta\mathbf{l}}$,

$$\tilde{\mathbf{s}}_{\beta\mathbf{l}} = (\hat{\mathbf{T}}_{\alpha\beta} - \hat{\mathbf{T}}^{-1}_{\beta\alpha})^{-1}(\hat{\mathbf{T}}_{\alpha\beta}\tilde{\mathbf{s}}_\beta - \tilde{\mathbf{s}}_\alpha) \tag{6.8}$$

Similarly for $\tilde{\mathbf{s}}_{\alpha\mathbf{l}}$

$$\tilde{\mathbf{s}}_{\alpha\mathbf{l}} = (\hat{\mathbf{T}}_{\beta\alpha} - \hat{\mathbf{T}}^{-1}_{\alpha\beta})^{-1}(\hat{\mathbf{T}}_{\beta\alpha}\tilde{\mathbf{s}}_\alpha - \tilde{\mathbf{s}}_\beta) \tag{6.9}$$

$\tilde{\mathbf{s}}_\alpha$ and $\tilde{\mathbf{s}}_\beta$ are the WFS measurements and the $\hat{\mathbf{T}}$ transforms can be obtained by considering the geometry of the system i.e., where sub-apertures from a WFS observe the uplink path on the other laser(s). Information from the vertical turbulence profile can be used to optimise these matrices.

It is now possible to calculate the turbulence induced slopes, as $\tilde{\mathbf{s}}_\mathbf{t} = \tilde{\mathbf{s}} - \tilde{\mathbf{s}}_\mathbf{l}$. These are the slopes which would have been measured from a guide star with no uplink tip-tilt effects, and can be used to perform the wavefront reconstruction without the requirement of an NGS for tip-tilt measurement. The above analysis can be performed for more complex LGS AO systems with many LGSs in other geometries.

In general there will be more than one discreet turbulent layer in the atmosphere, hence the measurement of a particular element in $\tilde{\mathrm{s}}_{\beta\mathrm{t}}$ which overlaps with LGS α will not just represent the turbulence at height h, but will be the sum of the wavefront deviation acquired at all turbulent layers by that element. This results in some noise in the measurement of $\tilde{\mathrm{s}}_{\alpha\mathrm{l}}$. The noise is mitigated by increasing the number of LGSs, such that other layers from non-overlapping heights average to zero, leaving only the common measurement of the slope at the point LGS α overlaps with the layer at h.

For the centre launched case the slopes due to downlink turbulence, $\mathbf{s}_\mathbf{t}$, cannot be determined for a turbulent layer at the ground. For a layer at this height, $\tilde{\mathbf{s}}_{\alpha\mathbf{t}} = \tilde{\mathbf{s}}_{\beta\mathbf{t}}$, $\tilde{\mathbf{s}}_{\alpha\mathbf{l}} = \tilde{\mathbf{s}}_{\beta\mathbf{l}}$, $\tilde{\mathbf{s}}_\alpha = \tilde{\mathbf{s}}_\beta$, and so is no longer more than one independent equation from which to determine $\tilde{\mathbf{s}}_{\alpha\mathbf{l}}$ and $\tilde{\mathbf{s}}_{\beta\mathbf{l}}$. In practice there will be a secondary obscuration which hides the path of the lasers at low altitudes, further limiting the method's performance to determine uplink tip-tilt resulting from low altitude turbulence.

An AO system which launches the LGSs from different point within the telescope aperture could potentially better predict low altitude uplink tip-tilt as $\tilde{\mathbf{s}}_{\alpha\mathbf{l}} \neq \tilde{\mathbf{s}}_{\beta\mathbf{l}}$, so they again may be determined. A system with LGSs launched from outside the telescope aperture (side launched) is unsuitable for this method of LGS uplink tip-tilt correction as a LGS's launch path is not in the field of view of other LGS WFSs at all.

6.3.2 Obtaining LGS Uplink Transforms

The LGS uplink matrices describing the response of LGS motion to WFS measurements are defined in Eq. (6.3), they relate measurements from a WFS due to downlink turbulence to the predicted uplink path of another LGS. They can be calculated by considering the geometry illustrated in Fig. 6.2, and the effect of a turbulence layer at a height h with a small region of turbulence where the field of view of sub-aperture n overlaps with LGS α. H is the altitude of the LGS beacon.

For a given sub-aperture, $s_{\alpha l}$ is the slope measured due to uplink tip-tilt on WFS α. It is related to the slope measured due to downlink turbulence on a corresponding sub-aperture on WFS β, which views LGS α at height h, $s_{\beta t}$. It is shown in Appendix A that

$$s_{\alpha l} = \left(1 - \frac{h}{H}\right) s_{\beta t} \tag{6.10}$$

The system has only a finite vertical resolution (defined by the number of sub-apertures and LGS asterism separation) to correct for turbulent layers. Sub-aperture n will observe the integrated turbulence between where the LGS enters its field of view and where is exits its field of view. Different groups of sub-apertures on a WFS will correspond to different turbulent layer heights for which they can predict uplink tip-tilt on other LGS WFSs. Recalling that $\mathbf{s}_{\alpha l}$ is homogeneous for the x and y-gradients, $\hat{\mathbf{T}}_{\alpha\beta}$ for the simple two dimensional system described above is

$$\hat{\mathbf{T}}_{\alpha\beta} = \begin{pmatrix} 1-\frac{h_1}{H} & 1-\frac{h_2}{H} & \cdots & 1-\frac{h_N}{H} \\ 1-\frac{h_1}{H} & 1-\frac{h_2}{H} & \cdots & 1-\frac{h_N}{H} \\ \vdots & \vdots & \ddots & \vdots \\ 1-\frac{h_1}{H} & 1-\frac{h_2}{H} & \cdots & 1-\frac{h_N}{H} \end{pmatrix} \tag{6.11}$$

where h_n denotes the centre of the vertical height 'bin' resolvable by the sub-aperture n. By considering the system geometry, including the launch position and angle of LGS α and β, θ_α and θ_β respectively, it is shown in Appendix B that h_n can be expressed as

$$h_n = \frac{H(D-(2n-1)d)}{D-(2n-1)d+2H(\theta_\beta+\theta_\alpha)} \tag{6.12}$$

for the centre launched case.

The final step in creating an LGS uplink interaction matrix is to tailor the matrix to the required atmospheric turbulence profile. Each column in the matrix shown in Eq. (6.11) represents a vertical height bin resolvable by the tomographic LGS AO system. If a turbulence profile is known, then columns which represent heights where there is negligible turbulence can be set to 0. This step will reduce the noise contributed by 'false layers' which could otherwise be detected, where random perturbations from real turbulent layers could seem like turbulence at a height where no turbulence is present.

6.4 A Learn and Apply Approach

6.4.1 Learn and Apply Formulation

The geometric approach described in the previous section proves the possibility of the estimation and recovery of LGS tip-tilt modes, but is clearly highly idealised. It requires an accurate knowledge of the turbulence $\mathrm{C_n^2}$ vertical profile and that all LGS WFSs are perfectly aligned to each other with perfect pointing of the LGSs. Though these challenges could be overcome through use of accurate external turbulence profilers and careful alignment and calibration procedures, it also does not make use of all available information. For this reason, it is not pursued further, other than to note that Eq.(6.8) and Eq.(6.9) are both linear expressions, dependant on the measured slopes from all system WFS measurements.

Whilst the correlation of tip-tilt modes between small and large apertures is small, correlation between adjacent sub-apertures can be significant (Wilson and Jenkins, 1996). This implies that information from sub-apertures other than those which have the LGS uplink turbulence of another WFS in their field of view can be used to improve the estimation of uplink tip-tilt of that LGS. Instead of the purely geometric approach, the Learn and Apply method can be used to make full advantage of our understanding of the turbulence statistics, and thus improve the estimation of uplink tip-tilt.

Learn and Apply is a method used in tomographic AO systems such as MOAO for open-loop tomographic reconstruction (Vidal et al., 2010), and has been described in more detail in § 2.4.2.2. In summary, a reconstructor, $\hat{\mathbf{W}}$, which converts a set off-axis measurements to the measurements which would be recorded by a WFS observing in the science target direction, is created through the relationship

$$\hat{\mathbf{W}} = (\hat{\mathbf{M}}_{\text{on}}\hat{\mathbf{M}}_{\text{off}}{}^{t})(\hat{\mathbf{M}}_{\text{off}}\hat{\mathbf{M}}_{\text{off}}{}^{t})^{-1} \tag{6.13}$$

where $\hat{M}_{\text{on}}$ and $\hat{M}_{\text{off}}$ are sets of measurements from an on-axis WFS, observing in the science directions, and measurements for the systems off-axis WFSs, respectively. For an infinite set of measurements, the general tomographic reconstructor is found,

$$\hat{\mathbf{W}}_{\text{tomo}} = \hat{\mathbf{C}}_{\text{onoff}}\hat{\mathbf{C}}^{\mathbf{-1}}_{\text{offoff}} \tag{6.14}$$

where $\hat{\mathbf{C}}_{\text{onoff}}$ is the covariance matrix between on and off-axis measurements, and $\hat{\mathbf{C}}_{\text{offoff}}$ the auto-covariance matrix between off-axis measurements. These covariance matrices can be computed analytically, when the system calibration and vertical turbulence profile is well known, but in practice, a “learn” data set is recorded, used to tune an analytical model of the covariance matrices. The “learn” data set accounts for the system alignment and the fitting to the analytical model creates a generic reconstructor which can be applied to any set of turbulence with the same statistical parameters.

The Learn and Apply algorithm is applicable for LGS tip-tilt prediction as § 6.3 proves that the required on-axis science direction slopes are a linear function of the off-axis LGS measurements. The advantages of using Learn and Apply are many fold. LGS tip-tilt prediction is no longer so reliant on perfect knowledge of system alignment and LGS pointing. The mathematics shown in § 6.3 do not have to be repeated for higher numbers of LGSs, which quickly becomes cumbersome. The turbulence profile does not have to be externally measured to a very high vertical resolution because it is acquired during the “learn” phase. Finally and perhaps most importantly, the use of covariance matrices derived for the known atmospheric statistics includes information about LGS uplink from sub-apertures near to those which have an overlapping field of view with a LGS beam path, hence use of all available information is made.

6.4.2 Slope Covariance Matrices for Multi-Laser Guide Star Tomographic Adaptive Optics Systems

The covariance matrix when considering two NGSs can be calculated using the method given in § 2.4.2.2, which utilises the covariance map describing the covariance of two wavefront gradient measurements with increasing separation. For traditional tomographic LGS AO where tip-tilt is ignored, covariance matrices are constructed by first discarding all tip-tilt information from LGS WFSs and then adjusting the separation values at each turbulence altitude to account for cone effect.

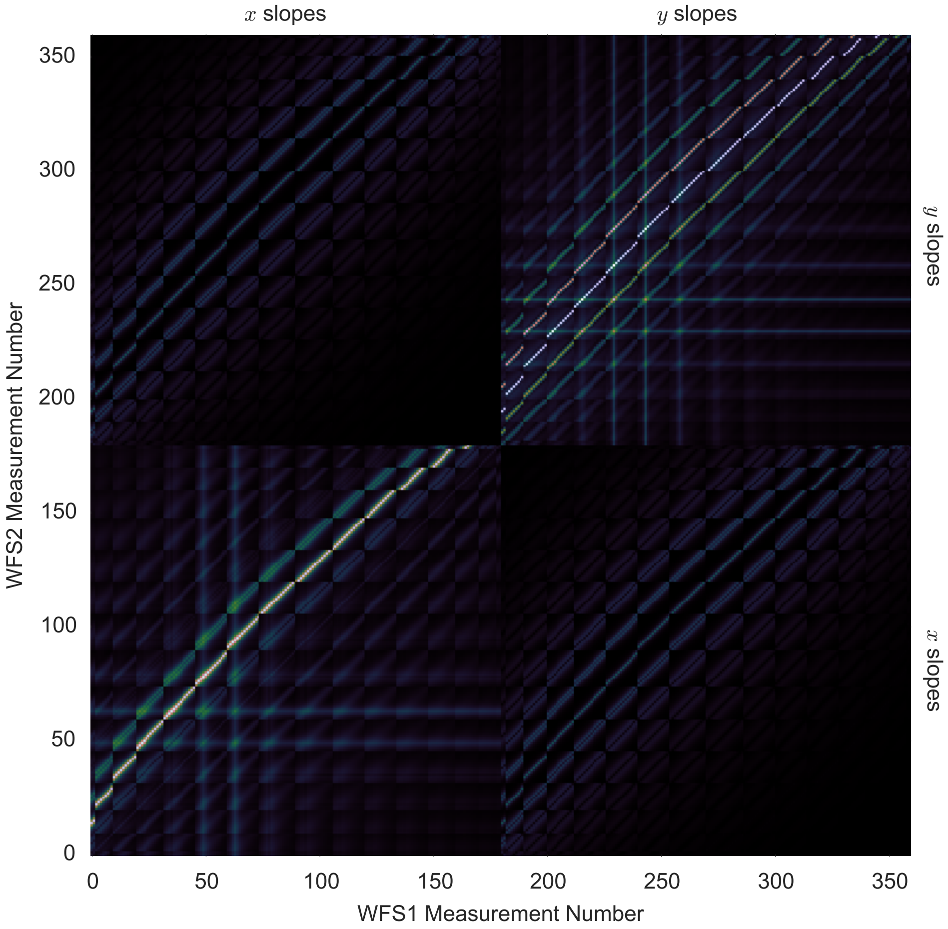

Figure 6.3: A computed covariance matrix between two off-axis LGS WFSs, with the tip-tilt information included. The vertical and horizontal lines which can be observed are a result of the correlation between certain sub-apertures on one WFS, with the LGS movement, and hence global tip-tilt measurement on the other WFS.

For uplink tip-tilt prediction, a similar process must be followed, but with no removal of the global tip-tilt signal measured by the LGS WFSs. This complicates matters somewhat, as the covariance between two slope measurements from LGS WFSs, s_α and s_β, now becomes

$$\langle s_\alpha s_\beta \rangle = \langle (s_{\alpha t} + s_{\alpha l})(s_{\beta t} + s_{\beta l}) \rangle \tag{6.15}$$

where s_l and s_t are again the components of the measurement due to uplink tip-tilt and downlink turbulence respectively.

Eq.(6.15) can be expanded into

$$\langle s_\alpha s_\beta \rangle = \langle s_{\alpha t} s_{\beta t} \rangle + \langle s_{\alpha t} s_{\beta l} \rangle + \langle s_{\alpha l} s_{\beta t} \rangle + \langle s_{\alpha l} s_{\beta l} \rangle \tag{6.16}$$

The first term of this expansion is the covariance between the downlink slope measurements which is the same as would conventionally be determined. The second and third terms account for the path of the LGS beams through the field of view of other WFSs and the resulting tip-tilt observed on the relevant LGS WFSs. These terms can also be determined from the covariance map by considering the separation between the laser beam position and the position of the field of view of each sub-aperture at each turbulence layer altitude.

The final term is a constant for all sub-aperture separations and dependant only upon the separation between the paths of the two LGSs at each turbulence layer altitude, which can again be determined from the covariance map. This term represents a contribution to the tomographic reconstruction error, as it will add a constant to all sub-aperture separations, reducing the contrast between correlating and non-correlating separations. It will be at a maximum when the LGS beams pass through the same patch of turbulence. This is the case at low altitude turbulence layers such as the ground layer when the LGS are centre launched. This will impair the prediction of LGS uplink tip-tilt contributions from these layers, but will affect prediction less for layers at altitude.

An example of a covariance matrix computed using Eq. (6.16) is shown in Fig. 6.3. The matrix is similar to that presented in Fig. 2.14, but differs in that it features vertical and horizontal lines in the sections of x and x covariance, and y and y covariance. These lines correspond with WFS sub-apertures which observe the patch of turbulence the other LGS passes through and hence shows a correlation with the tip-tilt measurement on the other WFS.

As in conventional Learn and Apply, the covariance matrices can be computed in an analytical form as above, or from data gathered in a learn step. In practice, it will be beneficial to again combine both methods, creating a tomographic reconstructor which accounts for system alignment as well as the general statistical properties of the turbulence.

6.5 Discussion

6.5.1 Implications for Adaptive Optics Corrected Sky Coverage

Current AO system are limited to areas of the sky with a star luminous enough to provide some wavefront information. The ability to determine tip-tilt information from LGSs alone allows an AO system to operate without the use of an NGS, providing complete and consistent sky-coverage with no ‘blind-spots’ at any point on the sky.

Eq. (6.16) implies that a centre launched LGS system will not provide good prediction of uplink turbulence if there is a strong turbulence layer at the ground altitude and the results in § 7 begin to explore this effect. It is possible that for some locations the ground turbulence layer will not be dominant, and hence the correction provided by the algorithm for higher layers will be sufficient. If this is the case, then full sky coverage is achieved.

More often, this will not be the case, so some other method is required to correct for tip-tilt on at the ground layer. In these instances, a NGS Ground Layer Adaptive Optics (GLAO) system may be used, which could use NGSs far off-axis from the astronomical science target as it must only isolate the ground layer. The NGS GLAO need only determine tip-tilt information hence would would not require fast frame rates, allowing the use of dim NGSs. There will be further investigation into whether observatories existing fast guiding systems, which already use multiple dim NGSs to maintain accurate telescope pointing across the full sky, would be suitable. The tomographic uplink prediction reconstruction would also require alteration to avoid spurious signals due to errors at the ground layer. This can be performed by only using the conventional downlink tomographic covariance matrices for the ground layer and not the uplink correction terms.

6.5.2 Potential Sources of Tomographic Laser Guide Star Prediction Error

This chapter has described a method of regaining tip-tilt information from a LGS only AO system, but there are a number of potential error sources which we have not accounted for which may reduce system performance.

The analysis presented above does not include the effects of WFS noise. Noise degrades the wavefront measurements, leading to a degradation in AO performance. As the LGS uplink prediction algorithm has a strong dependence on the subset of sub-apertures which observe the other LGSs beams, noise in one or more of those sub-aperture may have a large, adverse impact on system performance. In future works, the effects of noise will be examined analytically, through simulation and with the Durham Real-Time Adaptive Optics Generalised Optical Nexus (DRAGON).

A LGS only AO system would be completely insensitive to vibrations which affected the entire telescope. As the telescope and LGS launch telescopes would vibrate together, it would be completely invisible on the LGS WFSs, adding tip-tilt error to the corrected science Point Spread Function (PSF). Davies et al. (2008) discusses this problem regarding LGS only correction with no tip-tilt correction. They conclude that, whilst degrading correction, the degradation is not significant as the telescope’s fast guiding NGS can detect most vibrations.

Vibrations of the LLT alone would also add tip-tilt errors which would not be corrected by the tomographic reconstructor. Such vibrations would be visible on the LGS WFSs however and would show some periodicity with statistics different to those of atmospheric turbulence, hence it is hoped that this could be corrected using a temporal predictor in the reconstructor. Such temporal predictors have already been demonstrated on the CANARY

AO system (Sivo et al., 2014). Both sources of vibration error would be be eliminated if the LGS uplink retrieval method was used in conjunction with a NGS GLAO tip-tilt detecting system is discussed in § 6.5.1.

6.5.3 Applicability to Current and Planned Tomographic Laser Guide Star Adaptive Optics Systems

One advantage of the method described above in comparison to some of those described in § 2.3.6.4, is that it can be applied to some existing or currently planned AO systems with modification only to the reconstruction algorithm. Gemini Multi-Conjugate Adaptive Optics System (GeMS), CANARY and Advanced Rayleigh Ground Layer Adaptive Optics System (ARGOS) are all centre launched, multiple LGS AO systems, which would be good candidates to implement the algorithm on sky (Myers et al., 2008; Rabien et al., 2010; Rigaut et al., 2012). Unfortunately, the algorithm is not applicable to the Very Large Telescope (VLT) Adaptive Optics Facility (AOF), as it is planned to use side-launched LGSs (Stroebele et al., 2006).

Out of the coming generation of Extremely Large Telescopes (ELTs), only the Thirty Metre Telescope (TMT) features centre launched LGSs (Joyce et al., 2006), thus LGS uplink tip-tilt retrieval would only be possible for the TMT. It is not applicable to the current designs for the Giant Magellan Telescope (GMT) or European Extremely Large Telescope (E-ELT) AO systems, as both feature side-launched LGSs (Lombini et al., 2012; Conan et al., 2012).

6.6 Summary

In this chapter, a method has been presented to determine the uplink deviation of LGSs for multiple LGS tomographic AO systems. Such a method is possible at all because the correlation of tip-tilt aberration modes between the LGS launch aperture and the entire telescope aperture is very small. This means that the measurement observed on the LGS WFSs is a function of the turbulence experienced on the uplink and downlink paths, and not completely reciprocal.

A purely geometrical approach to uplink prediction is presented in § 6.3, which uses information from WFS sub-apertures observing the uplink path of the LGS beams. As this method does not use all information regarding the atmospheric statistics and also requires perfect calibration and alignment of the AO system, the Learn and Apply algorithm is proposed for practical use. In § 6.4 the advantages of using Learn and Apply are outlined. The additions required to form analytical covariance matrices are derived, and an example of an uplink included covariance matrix is shown.

Finally, the advantages and limitations of using LGS uplink prediction are discussed in § 6.5. There is the potential for full sky coverage for some AO systems, but this is dependent upon the turbulent vertical profile of the observing site, as the method will not correct well for ground layer turbulence. Mitigation techniques to aid correction of the ground layer are suggested, though these are not investigated further in this work. WFS noise and telescope vibration are also potential error sources which must be considered. Finally, the applicability of the algorithm for current telescopes is discussed, and a number of potential candidate test AO systems identified.

Chapter 7

Laser Guide Star Uplink Tip-Tilt Retrieval Simulation Results

In the following chapter results of the Laser Guide Star (LGS) tip-tilt retrieval algorithm derived in § 6 are presented. Investigations using the Python Adaptive Optics Simulation (PyAOS) which was described in § 4 have been undertaken to verify the technique and provide estimates of LGS only Adaptive Optics (AO) performance. Results from the Durham Real-Time Adaptive Optics Generalised Optical Nexus (DRAGON) have yet to be obtained as the current reconstructors, made only using the "learn" data, are far from optimal due to the limited number of available independent turbulence frames. Together with the presence of Wavefront Sensor (WFS) noise, this does not allow reliable tomographic correction.

Experiments in simulation create the tomographic reconstructor using only the covariance matrices determined from the learn stage and the analytical fitting step is not performed. A very large number of uncorrelated phase screens can be generated to form covariance matrices which converge to close to the analytical form, so this does not impair the simulated reconstructor. The learn measurements for the simulation are gathered by running the system with no correction for a large number of frames. A "truth" sensor is present, which observes a Natural Guide Star (NGS) in the direction of the science target but is not used when correction is performed. Covariance matrices between the slopes are calculated, which are then used to form a tomographic reconstructor.

7.1 Simulation Parameters

The following simulations compare the AO correction performance of the LGS uplink tip-tilt retrieval method using a Laser Tomographic Adaptive Optics (LTAO) system against the conventional Learn and Apply method, with and without the use of a NGS to provide tip-tilt information. It is expected that whilst the LGS tip-tilt retrieval method will not perform as well as when a NGS is used for tip-tilt information due to increased tomographic error, it will provide superior correction to that without tip-tilt correction.

To avoid errors in the complex process of LTAO reconstruction with a NGS tip-tilt WFS, simulations of LTAO with NGS tip-tilt are modelled ideally, as LGS which do not experience uplink turbulence. This will give the upper bound of NGS tip-tilt corrected LTAO

Parameter	Value
Telescope primary diameter (m)	8
Central Obscuration diameter (m)	1.1
Phase points in pupil	256 × 256
Phase screen size (m)	128 × 128
Off-axis guide star positions	4 LGS on a 10 arc-second radius circle
WFS sub-apertures	16×16
DM Actuators	17×17
Science field wavelength (µm)	1.65
Science integration time (s)	60
Loop frame rate (Hz)	400

Table 7.1: Parameters used in the LGS uplink retrieval simulations, unless otherwise stated.

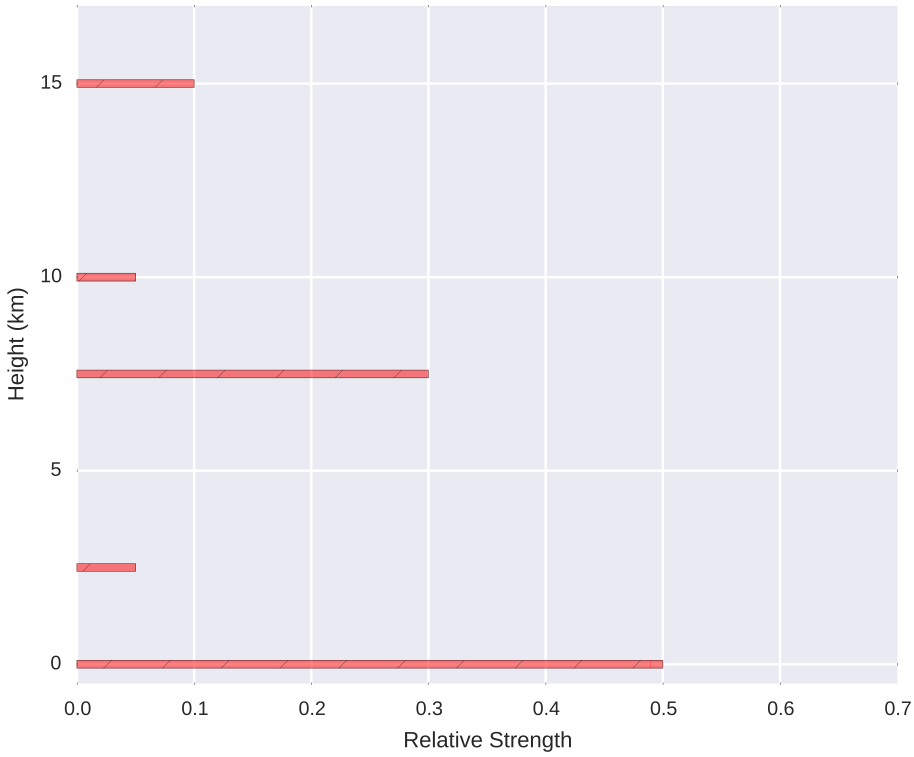

Figure 7.1: The atmospheric turbulence profile used for the simulations performed, unless otherwise stated.

performance, as if a bright, on-axis tip-tilt guide star was being used. It can be expected that in real use with an off-axis tip-tilt NGS, performance would not be as high.

The parameters for the simulation are shown in Table 7.1, they have been chosen to emulate current, 8 m class telescopes, though not one system in particular. The simulated atmospheric profile used to obtain the results presented in Fig. 7.3 and Fig. 7.4 features five turbulence layers with strengths shown in Fig. 7.1. The profile was chosen to be similar to those measured by Shepherd et al. (2014) from the Roque de los Muchachos observatory and features a dominant ground layer.

As was mentioned in § 4, the PyAOS simulation code is not yet optimised for performance, so the parameters represent a balance between simulation accuracy and speed of execution. In particular, it may be useful in future to simulate a turbulence profile with a greater number of turbulence layers.

7.2 Simulated Covariance Matrices

An analytically calculated covariance matrix for tip-tilt included Shack-Hartmann (SH) LGS WFS measurements was presented in § 6.4.2. The noticeable difference to a NGS covariance matrix (Fig. 2.14), or to the case of a LGS with tip-tilt removed, is a number of vertical and horizontal lines corresponding to sup-apertures which view the path of the other LGSs and hence tip-tilt on the corresponding LGS WFSs. Fig. 7.2 shows a pair of simulated covariance matrices for two AO systems, both with one on-axis WFS and four off-axis WFS. All WFSs have spatial order 8×8. The uppermost covariance matrix is calculated from a simulated AO system with only NGSs whilst the lower shows that from a system with an on-axis NGS, and four off-axis LGS WFSs.

Whilst the NGS only covariance matrix shows covariance between WFSs similar to those shown in Fig. 2.14, though with differing offsets, the LGS covariance matrix shows the predicted vertical and horizontal lines between LGS and LGS and LGS and NGS. This is evidence that the simulation is correctly simulating the uplink path of the LGS and the analysis performed in § 6 is correct.

7.3 Performance Estimates

Fig. 7.3 shows the simulated Strehl ratio of the three AO configurations with increasing turbulence strength. These simulations feature the turbulence profile illustrated in Fig 7.1. The results show that the uplink tip-tilt retrieval gives a marginal improvement in performance over tomographic LGS AO correction with no tip-tilt correction. The performance does not approach the case where tip-tilt is well corrected by a NGS, though this is not unexpected as the profile features a strong ground layer.

These results are examined further in Fig. 7.4. This plot shows the ratio of energy in the Point Spread Function (PSF) which is enclosed in a square, analogous to the throughput into a spectrograph, with increasing square size. The Fried parameter for these results is 14 cm. From this plot, it is possible to obtain either the increase in throughput provided by

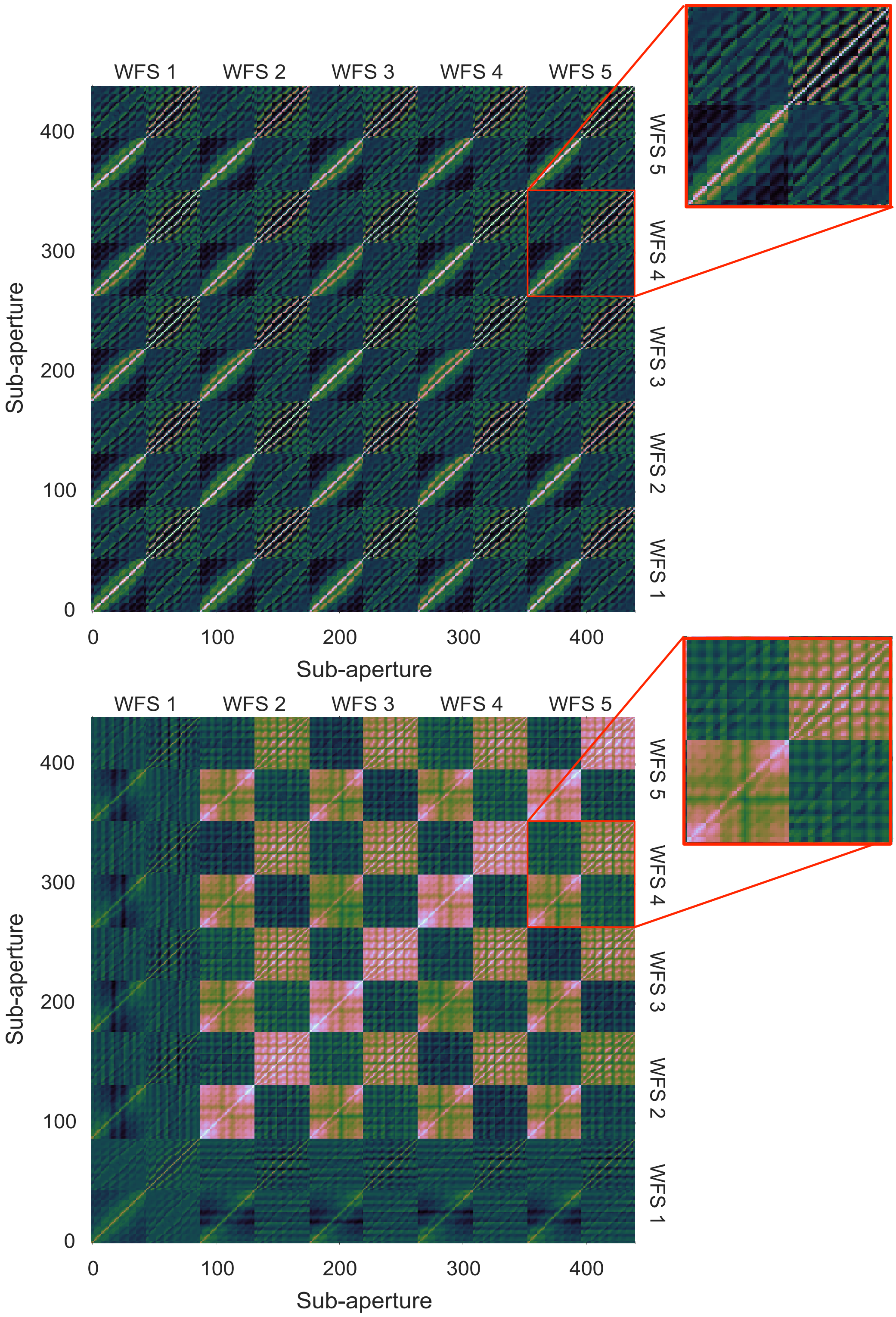

Figure 7.2: Simulated covariance matrices for an AO system with four off-axis NGS WFSs (top), and one with four off-axis LGS WFSs with tip-tilt included (bottom). Both systems use a NGS truth WFS (WFS 1) to form the covariance matrix. The LGS covariance matrix shows horizontal and vertical lines which correspond to sub-apertures which observe the path of other LGSs.

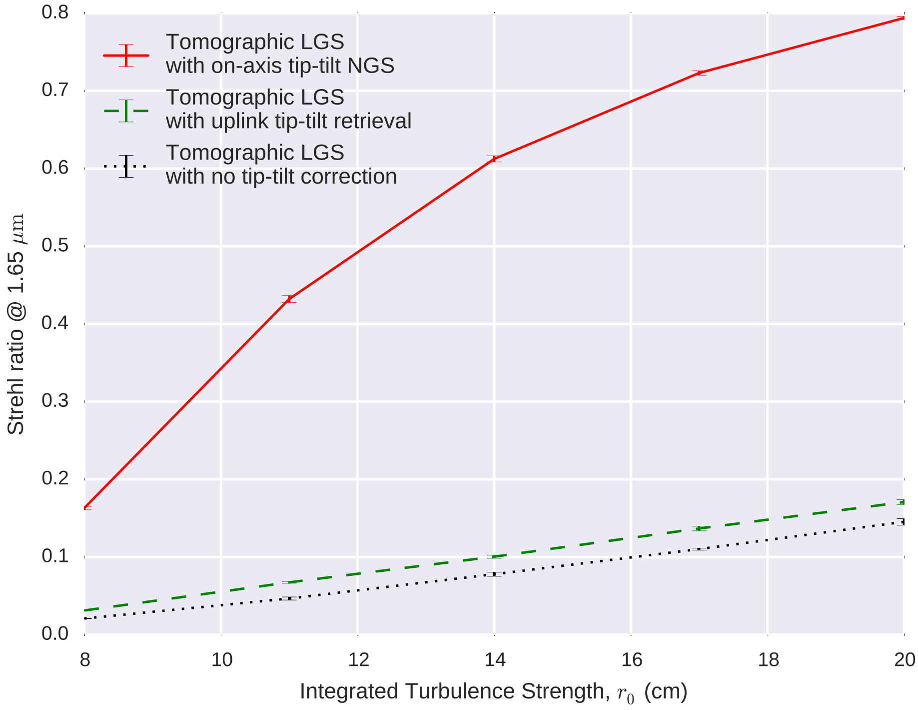

Figure 7.3: The performance of tomographic LGS AO with a NGS tip-tilt sensor (solid curve), the tip-tilt retrieval method (dashed curve) and no tip-tilt correction (dotted curve) versus increasing value of r_0. The LGS tip-tilt prediction gives a slight increase in performance for all turbulence seeing strengths compared to no tip-tilt correction.

LGS uplink tip-tilt retrieval for a given square size (up to a 5 % increase) or the increase in spatial resolution for a required throughput value (up to ≈ 20 mas).

It was predicted in § 6.4.2 that the LGS uplink tip-tilt retrieval method would not give optimal performance with ground layer turbulence present. This effect is explored in Fig. 7.5, where the performance of the method is measured with only a single turbulence layer with an r_0 value of 14 cm which is placed at an increasing altitude. It can be observed that the method does indeed perform poorly when the layer is at low altitudes, however as the layer altitude increases, the performance increases significantly and even begins to approach that of the NGS tip-tilt corrected case. The discontinuities in the curve are a result of differences in overlap between WFS sub-apertures and the footprint of the other LGS beams at different layer altitudes.

7.4 Discussion

7.4.1 Improved Full Sky Coverage Adaptive Optics

The results from the PyAOS simulation have shown that the method can provide increased AO performance in comparison to a tomographic LGS AO system which does not attempt

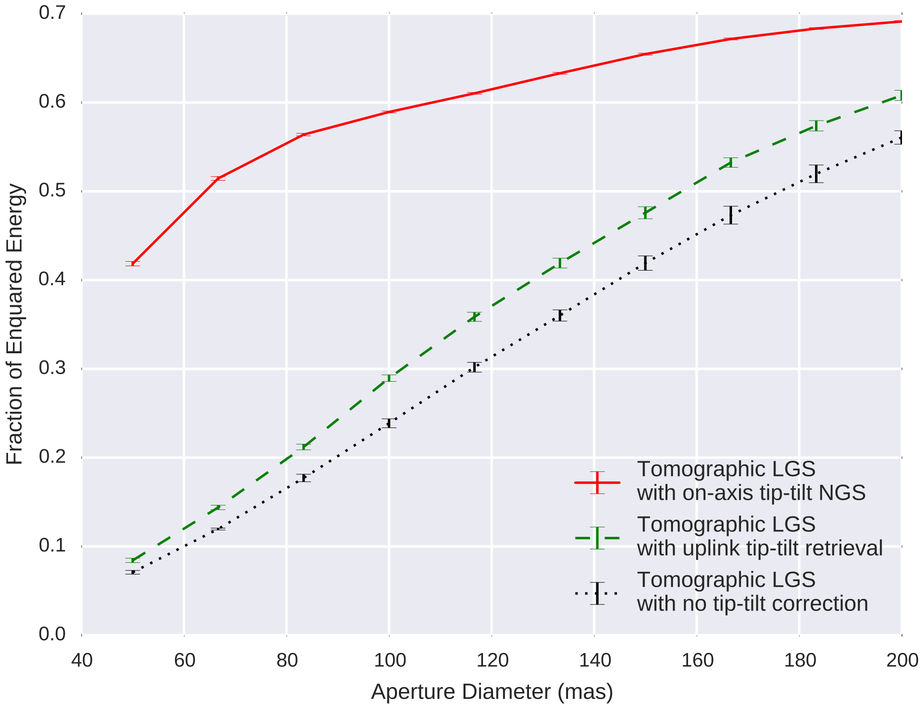

Figure 7.4: The ensquared energy of tomographic LGS AO with a NGS tip-tilt sensor (solid curve), the tip-tilt retrieval method (dashed curve) and no tip-tilt correction (dotted curve) versus square aperture size. This allows the increase in performance to be obtained, for example, a 5 % increase in throughput can be obtained for a spectrograph with 200 mas resolution.

to correct for tip-tilt. In § 2.3.6.4, a study by Davies et al. (2008) was discussed which showed that tomographic LGS only AO systems, with no tip-tilt correction, could be of use for some applications, such as 200 mas resolution spectroscopy.

The simulations presented in this chapter suggest that by simply modifying the reconstruction matrix to include the uplink tip-tilt method, throughput to such instruments would be improved by up to 5 %, even when the atmospheric turbulence profile is dominated by a strong ground layer. This is an alteration which can be easily made to many existing multi-LGS AO systems with no changes required to hardware or increased computational load. Alternatively, instrument designers may choose to increase the spatial resolution of instruments by around 20 mas, whilst maintaining the throughput of a system which does not use LGS uplink tip-tilt retrieval. These AO modes are applicable to the entire sky as there is no requirement to use a bright NGS.

7.4.2 Improved Performance of Ground Layer Adaptive Optics Systems

When low altitude turbulence is not present, the simulations show that the LGS uplink tip-tilt retrieval method can provide Strehl ratios comparable to those obtained with a tip-tilt

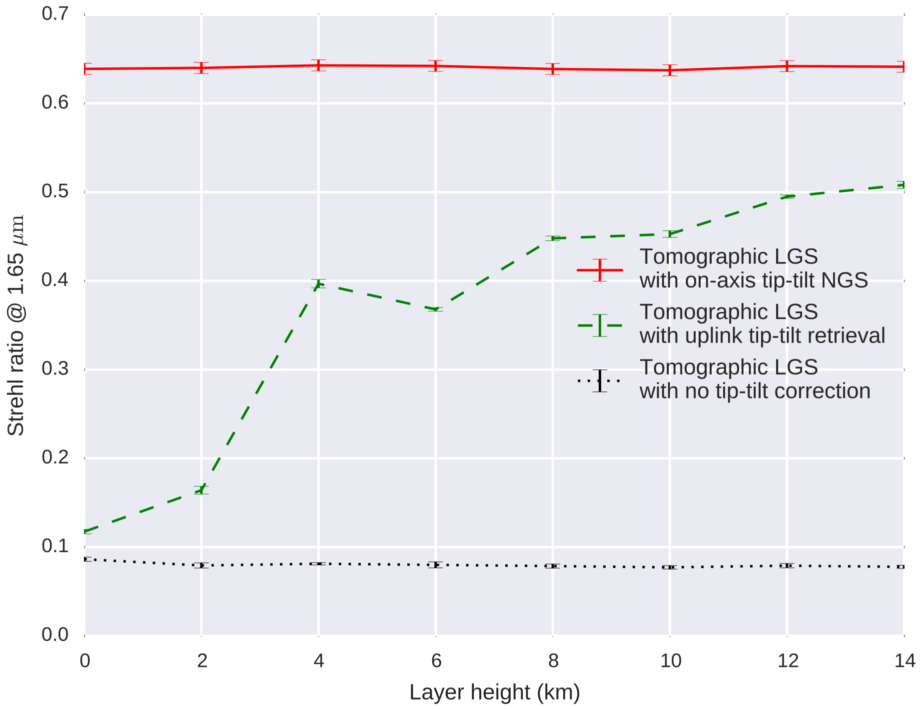

Figure 7.5: The Strehl ratio of tomographic LGS AO with a NGS tip-tilt sensor (solid curve), the tip-tilt retrieval method (dashed curve) and no tip-tilt correction (dotted curve) versus the altitude of a single turbulence layer. The LGS uplink tip-tilt prediction performance increases sharply as the layer increases.

NGS.

Ground Layer Adaptive Optics (GLAO) systems can make use of NGSs far from the science target to correct low turbulence layers which are common over a large field of view. This gives them a high sky-coverage in comparison to other AO modes. A tip-tilt GLAO configuration can be combined with the LGS uplink tip-tilt retrieval method, where the NGSs determine low altitude tip-tilt whilst the LGSs correct for high level tip-tilt and performs all high spatial order correction. For this application, the GLAO system need only detect tip-tilt allowing the use of very dim NGSs. This would significantly increase the sky coverage of tomographic LGS AO, as the NGS no longer need to be as close to the science target.

7.4.3 Future Studies

The results presented in this chapter have shown evidence of the capabilities of the LGS uplink tip-tilt retrieval method. Fitting the "learn" based covariance matrices to those analytically predicted is a priority. This will allow the method to be tested on the DRAGON laboratory bench. It also hugely decreases the execution time of simulation as the "learn" stage currently requires many frames and entails generating new random phase screens for each iteration. The fitting of analytically derived covariance matrices reduces the required number of frames significantly and hence simulation run time.

Future work will continue to optimise the technique. The position of the guide stars for example, may have a large impact on performance as it controls the tomographic altitude resolution. Such investigations can first be performed in simulation, before being tested on DRAGON. Potential sources of error must also be integrated into the simulation. It is planned that realistic WFS noise will soon be integrated into the code, so an analysis of its effect will begin shortly. Vibrations may also affect the LGS uplink tip-tilt retrieval method disproportionately when compared to other AO configurations. These are trivial to test with DRAGON or simulation, at which point investigations into temporal predictors can begin.

The integration of the technique with GLAO type systems used to determine low altitude tip-tilt will also entail careful consideration. It is likely that this can be achieved by tuning the covariance matrices such that the system does not attempt to correct for tip-tilt components common to all LGS WFSs, which correspond to low altitude turbulence. Once complete, performance and sky-coverage can be predicted for such combined systems.

Chapter 8

Conclusions

8.1 Thesis Aims

The aim of this work has been to investigate the recovery of some or all of the tip-tilt information from Laser Guide Star (LGS) Wavefront Sensors (WFSs), in order that the requirements for a Natural Guide Star (NGS) is reduced or removed in astronomical Adaptive Optics (AO). If possible, this would increase the sky coverage of AO systems, such that observations of more objects in the night sky can benefit from the increased resolution and observing efficiency that AO entails.

In order to further explore LGS uplink tip-tilt required, two advanced AO development tools were developed. Both offer novel features making them ideal for this task, with realistic LGS emulation and the flexibility to apply and test new AO configurations and components. The development of these tools into flexible, multipurpose facilities for AO investigations has become a further goal of the project.

8.2 Adaptive Optics Development Tools

8.2.1 Python Adaptive Optics Simulation

To verify and explore the possibility of LGS uplink tip-tilt retrieval, an end to end simulation which accurately represents LGSs was developed. Though existing simulations were explored, it became apparent that the creation of a new code was the best option.

The new simulation code was designed to be extremely flexible, such that new reconstructors, components or configurations can be integrated into the code quickly. This has been extremely useful in investigating LGS uplink tip-tilt, allowing realistic LGS simulation to be easily added to the code and reconstruction options to be rapidly explored. The new code was developed solely by the author of thesis.

As the code is written entirely in the Python programming language, it is very readable in comparison to some other, lower level languages. It also features a simple and intuitive Application Programming Interface (API). For these reason, it is ideal for use by those new to the field of AO to explore parameter spaces, create simple AO configurations and even to extend the code as required. This has already been proven through extensions provided by other PhD. students at the Centre for Advanced Instrumentation (CfAI). The Python

Adaptive Optics Simulation (PyAOS) is also under consideration to be used as a teaching tool at other institutions world wide (Dani Guzman, personal communication, 13th March 2015).

None the less, there is still much room to improve the PyAOS. The performance of the code does not rival other codes which have been designed with speed in mind. This limits its use when exploring large parameter spaces or in investigating Extremely Large Telescope (ELT) scale issues. Investigations are currently being carried out as to the most efficient way to speed up the code, including the use of accelerated Python run-time environments or Graphical Processing Unit (GPU) based acceleration.

8.2.2 DRAGON

The Durham Real-Time Adaptive Optics Generalised Optical Nexus (DRAGON) is a flexible laboratory test bench which is nearing completion in the CfAI. It is designed to be modular such that components can be re-arranged with little re-alignment effort required. This gives the bench enormous flexibility to investigate a large variety of AO configurations. The author has been responsible for overall management and integration of DRAGON development and the construction of many individual components.

DRAGON features multiple LGS and NGS WFSs which will allow it to investigate and optimise tomographic modes of AO. The fact that the bench runs at frame rates comparable to real on-sky AO system makes it invaluable for the development of Real-Time Control System (RTCS) issues applicable to high order and ELT scale problems.

The generation of deterministic turbulence in the laboratory is a non-trivial issue, which has in the past been solved by a complex procedure of applying acrylic spray to a plastic disk with a specific pattern, creating random phase or expensive lithography with low phase resolution. First results of a new method of phase screen creation have been presented in this thesis, where phase is cut into a plastic disk using precision machining. Early examination of the measured power spectra of a prototype machined phase screen demonstrate that it shows statistical properties not inconsistent with measured statistical properties of atmospheric turbulence. This method has much greater flexibility than previous phase screen generation methods, as it allows the exact phase to be prescribed and screens of a larger size and range of statistical properties to be created.

A unique method of LGS emulation has been utilised within DRAGON. This is created by propagating a laser up through the turbulence phase screens to form a guide star in a fluorescent cell. Light from the cell then passes back down through the same phase screens before entering the emulated “telescope”. This method is analogous to the real case, where the laser must pass up through turbulence before forming a LGS. Integration results into this method have been presented, which show that it changes the variance of tip-tilt, as expected.

As well as emulating uplink turbulence, the depth of the fluorescent cell results in potential elongation of the source. Both effects can be studied in real-time, in contrast to many previous laboratory experiments where they were created slowly, by scanning Deformable Mirrors (DMs) or other means. Accurate LGS emulation with multiple LGS WFSs makes

DRAGON the ideal test-bench for exploring LGS tip-tilt retrieval methods, which will be presented in future works.

8.2.3 An Integrated Development Framework

The PyAOS simulation and the DRAGON laboratory test bench are highly complementary. New concepts for AO can be very quickly integrated into the simulation code, which may be used to estimate optimal parameters for the new configuration. A DRAGON module can then be created, or software added to the flexible RTCS to integrate the concept into the laboratory bench for further investigation. This process is especially applicable to LGS based schemes as both the simulation and DRAGON feature novel LGS emulation capabilities.

Finally, components designed for DRAGON are also compatible, with a little alteration, with the CANARY Multi-Object Adaptive Optics (MOAO) demonstrator at the William Herschel Telescope (WHT), where the new concept can be tested and verified on sky. This results in an extremely powerful toolchain for rapid development of new ideas to improve AO correction.

8.3 Laser Guide Star Uplink Tip-Tilt Retrieval

In § 6, an original method for retrieving the tip-tilt experienced by a laser on its path to forming a LGS is presented. Though a purely geometric approach to tip-tilt retrieval may be possible, a Learn and Apply based reconstructor is more performant as it includes information regarding the statical properties of the turbulence and the alignment of the AO system.

The uplink tip-tilt included tomographic reconstructor can be formed through analysis of the analytically derived covariance map of spatial separations in Von Kármán turbulence. Examples of the expected covariance matrices have been created, though further work is required before they can be fitted to real data. This step is required when operating the reconstructor on any real AO system, including the DRAGON test bench.

It is possible to form the tomographic reconstructor in simulation through the direct recording of WFS measurements observing a "learn" step of uncorrelated random phase screens with identical statistics. Using this method LGS uplink tip-tilt retrieval reconstructors have been created for use in simulation. Results from the simulation have shown the technique can give improved performance for all sky-coverage AO, for applications where low spatial resolution is required. This is the case for some spectrographic applications (Davies et al., 2008).

The uplink retrieval reconstructor has been shown to be highly dependent upon the vertical turbulence profile. It is less sensitive to low turbulence layers, as all lasers pass through similar turbulence. At higher altitudes the LGS paths are less correlated, and hence there is little undetectable common motion between all LGSs. For scenarios where only high altitude turbulence is present, the simulations suggest that correction with Strehl ratios up to 70 % of the NGS tip-tilt corrected case is possible. If the LGS uplink tip-tilt retrieval algorithm were combined with existing or future Ground Layer Adaptive Optics (GLAO) systems, far greater performance may be achieved compared to GLAO alone, whilst the already high sky-coverage of such systems is increased as it must only supply low altitude tip-tilt information.

APPENDIX A

The Relationship Between Measured Downlink and Laser Guide Star Uplink Turbulence

To find the relationship between a sub-aperture measurement on WFS β, $s_{\beta t}$ and the measured uplink on LGS α, $s_{\alpha l}$ we consider Fig. A.1, which shows the effect of a small tilt on the uplink of LGS α. For this analysis, it is assumed that both $s_{\alpha l}$ and $s_{\beta t}$ are components of a measurements from a Shack-Hartmann (SH) Wavefront Sensor (WFS), describing the angular deviation of light propagation. The component of the slope on a sub-aperture on WFS α measured due to uplink turbulence is

$$s_{\alpha l} = \theta_\alpha - \theta_x \tag{A.1}$$

where θ_α is the launch angle of LGS α from the centre of the field and θ_x is dependant on the turbulence that LGS α propagates through at height h. θ_x can be expressed as,

$$\theta_x = \frac{H\theta_\alpha - x}{H} \tag{A.2}$$

It can be safely assumed that the laser beam angular deviation of $s_{\beta t}$ is small, so

$$x = s_{\beta t}(H - h) \tag{A.3}$$

Substituting Eq. (A.3) and Eq. (A.2) back into Eq. (A.1), an expression relating the downlink component of the slope measured on WFS β to the Laser Guide Star (LGS) uplink component of the slope measured on WFS α is obtained.

$$\begin{aligned} s_{\alpha l} &= \theta_\alpha - \frac{H\theta_\alpha - s_{\beta t}(H - h)}{H} \\ &= s_{\beta t}\left(1 - \frac{h}{H}\right) \end{aligned} \tag{A.4}$$

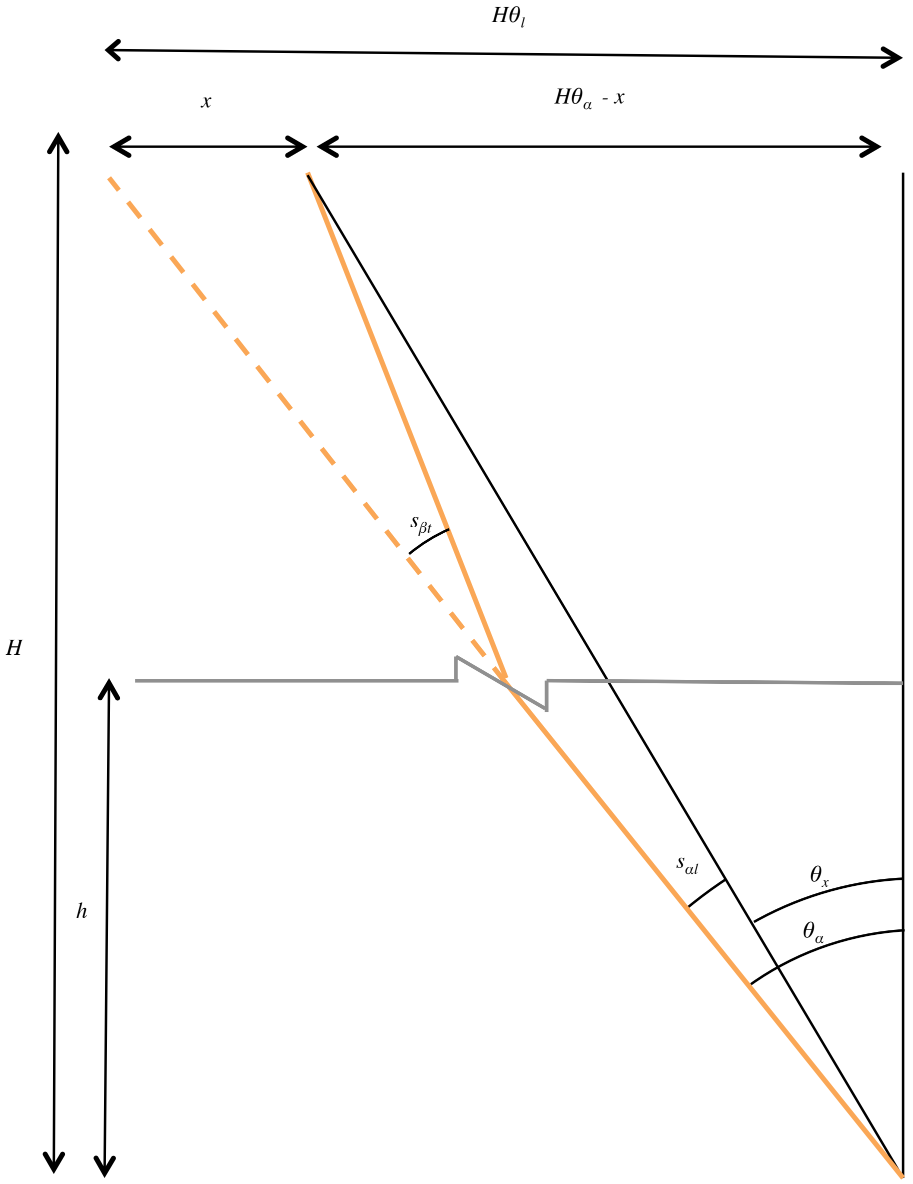

Figure A.1: The displacement on LGS α caused by turbulence encountered on uplink.

Appendix B

Calculating Resolved Tomographic Vertical Bin Heights

Only a finite number of LGS uplink offsets at turbulence layers can be predicted by the method described in § 6. This is a result of finite spatial resolution of the WFS being used. For a centre launched tomographic LGS Adaptive Optics (AO) system, only half the number of WFS sub-apertures view the path of another LGS, hence only half can be used to predict uplink LGS tip-tilt.

Turbulence which affects the path of a LGS can only be measured in vertical "bins", where the beam overlaps with field of view of a WFS sub-aperture. The measurement is the sum of the turbulence in the sub-aperture field of view within the vertical bin. The central heights of these bins can be calculated by considering the geometry of the system, illustrated in detail in Fig. B.1. θ_α, θ_β are the launch angles for LGS α and β respectively, H is the height of the LGS constellation, D_s is the displacement of the centre of sub-aperture n to the LGS launch position and D is the diameter of the telescope pupil.

For small angles

$$D_s = h\theta_s + h\theta_\alpha \tag{B.1}$$

so

$$h = \frac{D_s}{\theta_s + \theta_\alpha} \tag{B.2}$$

θ_s can be obtained by considering the displacement on the ground between the LGS beacon position and the centre of the sub-aperture, $D_s + H\theta_\beta$.

$$\theta_s = \frac{D_s + H\theta_\beta}{H} \tag{B.3}$$

The observed altitude of the a sub-aperture at distance D_s from the launch position can now be expressed as

$$h = \frac{HD_S}{D_s + H(\theta_\beta + \theta_\alpha)} \tag{B.4}$$

In practice, it is more useful to know the altitude each sub-aperture observes by the sub-aperture index, rather than its displacement. D_s is dependent on the sub-aperture of

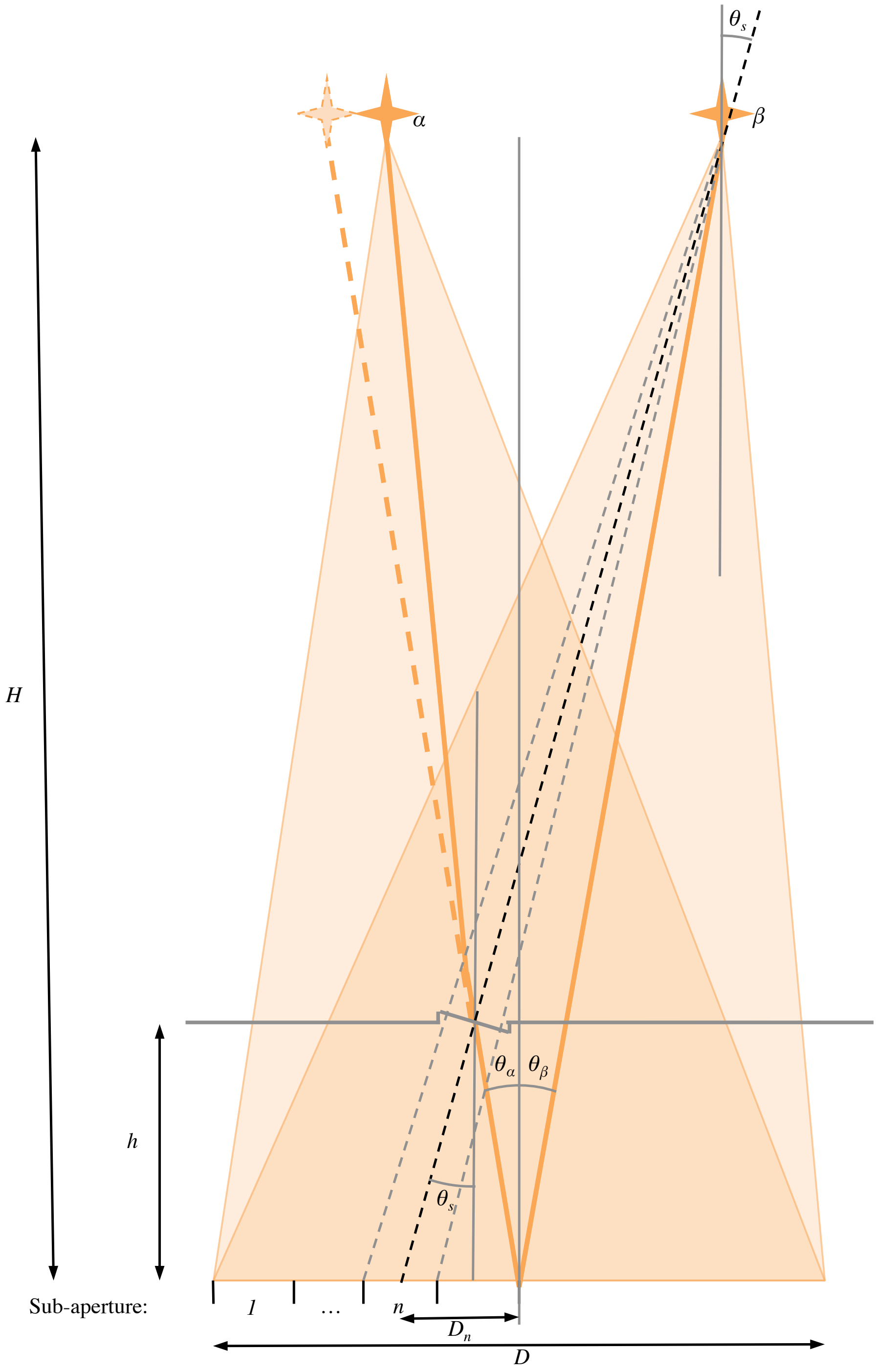

Figure B.1: A diagram illustrating the variables required to calculate the height which each sub-aperture of a WFS observes the LGS beam.

interest, n. The position of the centre of a sub-aperture is $(n-0.5)d$ from the edge of the telescope pupil, where d is the diameter of sub-aperture. For the centre launched case,

$$D_s = \frac{D}{2} - (\mathrm{n} - 0.5)\mathrm{d} \tag{B.5}$$

Finally, an expression for the height of the centre of the resolved height bin for each sub-aperture, h_n, can be obtained.

$$h_n = \frac{H(D-(2n-1)d)}{D-(2n-1)d+2H(\theta_\beta+\theta_\alpha)} \tag{B.6}$$

Bibliography

A. Agabi, J. Borgnino, F. Martin, A. Tokovinin, and A. Ziad. GSM: A grating scale monitor for atmospheric turbulence measurements. II. first measurements of the wavefront outer scale at the OCA. *Astronomy and Astrophysics Supplement Series*, 109:557–562, 1995.

E. Aller-Carpentier, M. Kasper, P. Martinez, E. Vernet, E. Fedrigo, C. Soenke, S. Tordo, N. Hubin, C. Verinaud, S. Esposito, et al. High order test bench for extreme adaptive optics system optimization. In *SPIE Astronomical Telescopes+ Instrumentation*, pages 70153Z–70153Z. International Society for Optics and Photonics, 2008.

D. R. Andersen, J. Stoesz, S. Morris, M. Lloyd-Hart, D. Crampton, T. Butterley, B. Ellerbroek, L. Jolissaint, N. M. Milton, R. Myers, et al. Performance Modelling of a Wide-Field Ground-Layer Adaptive Optics System. *Publications of the Astronomical Society of the Pacific*, 118(849):1574–1590, 2006.

D. R. Andersen, M. Fischer, R. Conan, M. Fletcher, and J.-P. Véran. VOLT: the Victoria Open Loop Testbed. In *SPIE Astronomical Telescopes+ Instrumentation*, pages 70150H–70150H. International Society for Optics and Photonics, 2008.

D. R. Andersen, K. J. Jackson, C. Blain, C. Bradley, C. Correia, M. Ito, O. Lardière, and J.-P. Véran. Performance modelling for the RAVEN Multi-Object Adaptive Optics Demonstrator. *Publications of the Astronomical Society of the Pacific*, 124(915):pp. 469–484, 2012. ISSN 00046280. URL `http://www.jstor.org/stable/10.1086/665924`.

R. Arsenault, P.-Y. Madec, J. Paufique, P. La Penna, S. Ströbele, E. Vernet, J.-F. Pirard, W. Hackenberg, H. Kuntschner, L. Jochum, et al. ESO adaptive optics facility progress report. In *SPIE Astronomical Telescopes+ Instrumentation*, pages 84470J–84470J. International Society for Optics and Photonics, 2012.

R. Arsenault, P.-Y. Madec, J. Paufique, P. La Penna, S. Stroebele, E. Vernet, J.-F. Pirard, W. Hackenberg, H. Kuntschner, J. Kolb, et al. ESO adaptive optics facility progress and first laboratory test results. In *SPIE Astronomical Telescopes+ Instrumentation*, pages 914802–914802. International Society for Optics and Photonics, 2014.

F. Assémat, E. Gendron, and F. Hammer. The FALCON concept: multi-object adaptive optics and atmospheric tomography for integral field spectroscopy–principles and performance on an 8-m telescope. *Monthly Notices of the Royal Astronomical Society*, 376(1): 287–312, 2007.

W. Baade and H. Swope. The palomar survey of variables in M 31 (first results). *The Astronomical Journal*, 60:151–152, 1955.

H. W. Babcock. The possibility of compensating astronomical seeing. *Publications of the Astronomical Society of the Pacific*, pages 229–236, 1953.

C. Baranec, R. Riddle, A. Ramaprakash, N. Law, S. Tendulkar, S. Kulkarni, R. Dekany, K. Bui, J. Davis, M. Burse, et al. Robo-AO: autonomous and replicable laser-adaptive-optics and science system. In *SPIE Astronomical Telescopes+ Instrumentation*, pages 844704–844704. International Society for Optics and Photonics, 2012.

A. Basden, T. Butterley, R. Myers, and R. Wilson. Durham extremely large telescope adaptive optics simulation platform. *Appl. Opt.*, 46(7):1089–1098, Mar 2007. doi: 10.1364/AO.46.001089. URL `http://ao.osa.org/abstract.cfm?URI=ao-46-7-1089`.

A. Basden, D. Geng, R. Myers, and E. Younger. Durham adaptive optics real-time controller. *Applied optics*, 49(32):6354–6363, 2010.

A. G. Basden. Visible near-diffraction-limited lucky imaging with full-sky laser-assisted adaptive optics. *MNRAS*, 442:1142–1150, Aug. 2014. doi: 10.1093/mnras/stu941.

M. Bec, F. J. Rigaut, R. Galvez, G. Arriagada, M. Boccas, G. Gausachs, D. Gratadour, E. James, R. Rojas, R. Rogers, et al. The Gemini MCAO bench: system overview and lab integration. In *SPIE Astronomical Telescopes+ Instrumentation*, pages 701568–701568. International Society for Optics and Photonics, 2008.

J. M. Beckers. Detailed compensation of atmospheric seeing using multiconjugate adaptive optics. In *1989 Orlando Symposium*, pages 215–219. International Society for Optics and Photonics, 1989.

M. S. Belen'kii. Fundamental limitation in adaptive optics: how to eliminate it? A full-aperture tilt measurement technique with a laser guide star. In *1994 Symposium on Astronomical Telescopes & Instrumentation for the 21st Century*, pages 321–323. International Society for Optics and Photonics, 1994.

M. S. Belen'kii. Fundamental limitation in adaptive optics: how to eliminate it? a full-aperture tilt measurement technique with a laser guide star. In *1994 Symposium on Astronomical Telescopes & Instrumentation for the 21st Century*, pages 321–323. International Society for Optics and Photonics, 1994.

M. S. Belen'kii. Full aperture tilt measurement technique with a laser guide star. In *SPIE's 1995 Symposium on OE/Aerospace Sensing and Dual Use Photonics*, pages 289–300. International Society for Optics and Photonics, 1995.

M. S. Belen'kii. Tilt angular anisoplanatism and a full-aperture tilt-measurement technique with a laser guide star. *Applied optics*, 39(33):6097–6108, 2000.

C. Benn, D. Abrams, T. Agocs, D. Cano, T. Gregory, J. C. Guerra, O. Martin, T. Morris, R. Myers, S. Rix, et al. GLAS/NAOMI: ground-layer AO at the William Herschel Telescope. In *Proc. SPIE*, volume 7015, page 701523, 2008.

J.-L. Beuzit, M. Feldt, K. Dohlen, D. Mouillet, P. Puget, F. Wildi, L. Abe, J. Antichi, A. Baruffolo, P. Baudoz, et al. SPHERE: a'Planet Finder'instrument for the VLT. In *SPIE Astronomical Telescopes+ Instrumentation*, pages 701418–701418. International Society for Optics and Photonics, 2008.

U. Bitenc, A. Basden, N. A. Bharmal, T. Morris, N. Dipper, E. Gendron, F. Vidal, D. Gratadour, G. Rousset, and R. Myers. On-sky tests of the CuReD and HWR fast wavefront reconstruction algorithms with CANARY. *Monthly Notices of the Royal Astronomical Society*, 448(2):1199–1205, 2015.

M. Boccas, F. Rigaut, M. Bec, B. Irarrazaval, E. James, A. Ebbers, C. d'Orgeville, K. Grace, G. Arriagada, S. Karewicz, et al. Laser guide star upgrade of Altair at Gemini North. In *Astronomical Telescopes and Instrumentation*, pages 62723L–62723L. International Society for Optics and Photonics, 2006.

D. Bonaccini-Calia, E. Allaert, C. Araujo, E. Brunetto, B. Buzzoni, M. Comin, M. J. Cullum, R. I. Davies, C. Dichirico, P. Dierickx, et al. VLT Laser guide star facility. In *Astronomical Telescopes and Instrumentation*, pages 381–392. International Society for Optics and Photonics, 2003.

D. Bonaccini-Calia, E. Allaert, J. Alvarez, C. A. Hauck, G. Avila, E. Bendek, B. Buzzoni, M. Comin, M. Cullum, R. Davies, et al. First light of the ESO laser guide star facility. In *Astronomical Telescopes and Instrumentation*, pages 627207–627207. International Society for Optics and Photonics, 2006.

M. Born and E. Wolf. Principles of optics electromagnetic theory of propagation. *Principles of Optics Electromagnetic Theory of Propagation, INterference and Diffraction of Light 2nd edition by Max Born, Emil Wolf New York, NY: Pergamon Press, 1964*, 1, 1964.

A. H. Bouchez, R. G. Dekany, J. R. Angione, C. Baranec, K. Bui, R. S. Burruss, J. R. Crepp, E. E. Croner, J. L. Cromer, S. R. Guiwits, et al. Status of the palm-3000 high-order adaptive optics system. In *SPIE Optical Engineering+ Applications*, pages 74390H–74390H. International Society for Optics and Photonics, 2009.

W. Brandner, G. Rousset, R. Lenzen, N. Hubin, F. Lacombe, R. Hofmann, A. Moorwood, A.-M. Lagrange, E. Gendron, M. Hartung, et al. NAOS+ CONICA at YEPUN: first VLT adaptive optics system sees first light. *The Messenger*, 107:1–6, 2002.

J.-M. Conan, G. Rousset, and P.-Y. Madec. Wave-front temporal spectra in high-resolution imaging through turbulence. *JOSA A*, 12(7):1559–1570, 1995.

R. Conan and C. Correia. Object-oriented Matlab adaptive optics toolbox, 2014. URL `http://dx.doi.org/10.1117/12.2054470`.

R. Conan, F. Bennet, A. Bouchez, M. van Dam, B. Espeland, W. Gardhouse, C. d'Orgeville, S. Parcell, P. Piatrou, I. Price, et al. The Giant Magellan Telescope laser tomography adaptive optics system. In *SPIE Astronomical Telescopes+ Instrumentation*, pages 84473P–84473P. International Society for Optics and Photonics, 2012.

R. Conan et al. Raven: a harbinger of multi-object adaptive optics-based instruments at the Subaru Telescope. In *SPIE Astronomical Telescopes+ Instrumentation*, pages 77360T–77360T. International Society for Optics and Photonics, 2010.

A. Consortini, C. Innocenti, and G. Paoli. Estimate method for outer scale of atmospheric turbulence. *Optics communications*, 214(1):9–14, 2002.

A. Costille, C. Petit, J.-M. Conan, C. Kulcsár, H.-F. Raynaud, and T. Fusco. Wide field adaptive optics laboratory demonstration with closed-loop tomographic control. *JOSA A*, 27(3):469–483, 2010.

J.-G. Cuby, S. Morris, I. Bryson, M. Lehnert, C. Evans, T. Fusco, P. Jagourel, R. Myers, G. Rousset, H. Schnetler, et al. EAGLE: an moao fed multi-IFU in the NIR on the E-ELT. In *SPIE Astronomical Telescopes+ Instrumentation*, pages 70141K–70141K. International Society for Optics and Photonics, 2008.

J.-G. Cuby, S. Morris, T. Fusco, M. Lehnert, P. Parr-Burman, G. Rousset, J.-P. Amans, S. Beard, I. Bryson, M. Cohen, et al. Eagle: a MOAO fed multi-IFU NIR workhorse for E-ELT. In *SPIE Astronomical Telescopes+ Instrumentation*, pages 77352D–77352D. International Society for Optics and Photonics, 2010.

R. Davies and M. Kasper. Adaptive Optics for Astronomy. *Annual Review of Astronomy and Astrophysics*, 50:305–351, Sept. 2012. doi: 10.1146/annurev-astro-081811-125447.

R. Davies, S. Rabien, C. Lidman, M. Le Louarn, M. Kasper, N. M. Förster Schreiber, V. Roccatagliata, N. Ageorges, P. Amico, C. Dumas, and F. Mannucci. Laser Guide Star Adaptive Optics without Tip-tilt. *The Messenger*, 131:7–10, Mar. 2008.

N. Dipper, A. Basden, U. Bitenc, R. Myers, A. Richards, and E. Younger. Adaptive Optics Real-time Control Systems for the E-ELT. In *Proceedings of the Third AO4ELT Conference*, volume 1, page 41, 2013.

A. P. Doel, C. N. Dunlop, J. V. Major, R. M. Myers, and R. M. Sharples. MARTINI: System operation and astronomical performance. In *San Diego,'91, San Diego, CA*, pages 319–326. International Society for Optics and Photonics, 1991.

C. d'Orgeville, S. Diggs, V. Fesquet, B. Neichel, W. Rambold, F. Rigaut, A. Serio, C. Araya, G. Arriagada, R. Balladares, et al. Gemini South multi-conjugate adaptive optics (GeMS) laser guide star facility on-sky performance results. In *SPIE Astronomical Telescopes+ Instrumentation*, pages 84471Q–84471Q. International Society for Optics and Photonics, 2012.

C. M. Dubbeldam, P. Clark, A. K. Kirby, K. Parkin, D. J. Robertson, S. Rolt, D. A. Ryder, and R. M. Sharples. The KMOS Integral Field System: fabrication, alignment, and test of 1000+ optical surfaces. In *SPIE Astronomical Telescopes+ Instrumentation*, pages 84501M–84501M. International Society for Optics and Photonics, 2012.

B. L. Ellerbroek and D. W. Tyler. Adaptive optics sky coverage calculations for the gemininorth telescope. *Publications of the Astronomical Society of the Pacific*, 110(744):pp. 165–185, 1998. ISSN 00046280. URL `http://www.jstor.org/stable/10.1086/316120`.

B. L. Ellerbroek, F. J. Rigaut, B. J. Bauman, C. Boyer, S. L. Browne, R. A. Buchroeder, J. W. Catone, P. Clark, C. d'Orgeville, D. T. Gavel, et al. MCAO for Gemini south. In *Astronomical Telescopes and Instrumentation*, pages 55–66. International Society for Optics and Photonics, 2003.

S. Esposito, A. Riccardi, E. Pinna, A. Puglisi, F. Quirós-Pacheco, C. Arcidiacono, M. Xompero, R. Briguglio, G. Agapito, L. Busoni, et al. Large Binocular Telescope Adaptive Optics System: new achievements and perspectives in adaptive optics. In *SPIE Optical Engineering+ Applications*, pages 814902–814902. International Society for Optics and Photonics, 2011.

C. L. Fefferman. Existence and smoothness of the Navier-Stokes equation. *The millennium prize problems*, pages 57–67, 2000.

L. Feng, E. Fedrigo, C. Béchet, E. Brunner, and W. Pirani. Computational performance comparison of wavefront reconstruction algorithms for the European Extremely Large Telescope on multi-CPU architecture. *Applied optics*, 51(16):3564–3583, 2012.

R. Flicker, F. J. Rigaut, and B. L. Ellerbroek. Comparison of multiconjugate adaptive optics configurations and control algorithms for the gemini south 8-m telescope. In *Astronomical Telescopes and Instrumentation*, pages 1032–1043. International Society for Optics and Photonics, 2000.

R. Foy and A. Labeyrie. Letter to the Editor Feasibility of adaptive telescope with laser probe. *Astron. Astrophys*, 152:L29–L31, 1985.

D. L. Fried. Statistics of a geometric representation of wavefront distortion. *JOSA*, 55(11): 1427–1431, 1965.

D. L. Fried. Optical Resolution Through a Randomly Inhomogeneous Medium for Very Long and Very Short Exposures. *J. Opt. Soc. Am.*, 56(10):1372–1379, Oct 1966. doi: 10.1364/JOSA.56.001372. URL `http://www.opticsinfobase.org/abstract.cfm?URI=josa-56-10-1372`.

D. L. Fried. Anisoplanatism in adaptive optics. *JOSA*, 72(1):52–52, 1982.

D. L. Fried. Time-delay-induced mean-square error in adaptive optics. *JOSA A*, 7(7): 1224–1225, 1990.

D. L. Fried and J. F. Belsher. Analysis of fundamental limits to artificial-guide-star adaptive-optics-system performance for astronomical imaging. *JOSA A*, 11(1):277–287, 1994.

R. Fugate, L. Wopat, D. Fried, G. Ameer, S. Browne, P. Roberts, G. Tyler, B. Boeke, and R. Ruane. Measurement of atmospheric wavefront distortion using scattered light from a laser guide-star. *Nature*, 353:144–146, 1991.

R. Q. Fugate, B. Ellerbroek, C. Higgins, M. Jelonek, W. Lange, A. Slavin, W. Wild, J. Wynia, J. Spinhirne, B. Boeke, et al. Two generations of laser-guide-star adaptive-optics experiments at the starfire optical range. *JOSA A*, 11(1):310–324, 1994.

T. Fusco, J.-F. Sauvage, C. Petit, A. Costille, K. Dohlen, D. Mouillet, J.-L. Beuzit, M. Kasper, M. Suarez, C. Soenke, et al. Final performance and lesson-learned of SAXO, the VLT-SPHERE extreme AO: from early design to on-sky results. In *SPIE Astronomical Telescopes+ Instrumentation*, pages 91481U–91481U. International Society for Optics and Photonics, 2014.

J. P. Gardner, J. C. Mather, M. Clampin, R. Doyon, M. A. Greenhouse, H. B. Hammel, J. B. Hutchings, P. Jakobsen, S. J. Lilly, K. S. Long, et al. The james webb space telescope. *Space Science Reviews*, 123(4):485–606, 2006.

D. T. Gavel. Tomography for multiconjugate adaptive optics systems using laser guide stars. In *Astronomical Telescopes and Instrumentation*, pages 1356–1373. International Society for Optics and Photonics, 2004.

E. Gendron, M. Brangier, G. Chenegros, F. Vidal, Z. Hubert, G. Rousset, and F. Pouplard. A new sensor for laser tomography on ELTs. In *1st AO4ELT conference-Adaptive Optics for Extremely Large Telescopes*, page 05003. EDP Sciences, 2010.

E. Gendron, F. Vidal, M. Brangier, T. Morris, Z. Hubert, A. Basden, G. Rousset, R. Myers, F. Chemla, A. Longmore, et al. MOAO first on-sky demonstration with canary. *Astronomy and Astrophysics*, 529:L2, 2011.

E. Gendron, C. Morel, J. Osborn, O. Martin, D. Gratadour, F. Vidal, M. Le Louarn, and G. Rousset. Robustness of tomographic reconstructors versus real atmospheric profiles in the ELT perspective. In *SPIE Astronomical Telescopes+ Instrumentation*, pages 91484N–91484N. International Society for Optics and Photonics, 2014.

R. Gilmozzi and J. Spyromilio. The European extremely large telescope (E-ELT). *The Messenger*, 127(11), 2007.

D. Gratadour, M. Puech, C. Vérinaud, P. Kestener, M. Gray, C. Petit, J. Brulé, Y. Clénet, F. Ferreira, et al. COMPASS: an efficient, scalable and versatile numerical platform for the development of ELT AO systems. volume 9148, pages 91486O–91486O–8, 2014. doi: 10.1117/12.2056358. URL `http://dx.doi.org/10.1117/12.2056358`.

J. L. Greenstein and E. Tandberg Hanssen. The abundance of beryllium in the sun. *The Astrophysical Journal*, 119:113, 1954.

D. P. Greenwood. Bandwidth specification for adaptive optics systems. *JOSA*, 67(3):390–393, 1977.

J. Hardy. *Adaptive Optics for Astronomical Telescopes*. Oxford series in optical and imaging sciences. Oxford University Press, 1998. ISBN 9780195090192. URL `http://books.google.co.uk/books?id=-0aAWyckS_8C`.

M. Hart. Recent advances in astronomical adaptive optics. *Applied optics*, 49(16):D17–D29, 2010.

M. Hart, S. Rabien, L. Busoni, L. Barl, U. Beckmann, M. Bonaglia, Y. Boose, J. Borelli, T. Bluemchen, L. Carbonaro, et al. Status report on the Large Binocular Telescope's ARGOS ground-layer AO system. In *SPIE Optical Engineering+ Applications*, pages 81490J–81490J. International Society for Optics and Photonics, 2011.

Y. Hayano, H. Takami, O. Guyon, S. Oya, M. Hattori, Y. Saito, M. Watanabe, N. Murakami, Y. Minowa, M. Ito, et al. Current status of the laser guide star adaptive optics system for Subaru Telescope. In *SPIE Astronomical Telescopes+ Instrumentation*, pages 701510–701510. International Society for Optics and Photonics, 2008.

E. Hecht. Optics. *Addison Wesley*, 997:213–214, 1998.

G. Herriot, S. Morris, A. Anthony, D. Derdall, D. Duncan, J. Dunn, A. W. Ebbers, J. M. Fletcher, T. Hardy, B. Leckie, et al. Progress on altair: the Gemini North adaptive optics system. In *Astronomical Telescopes and Instrumentation*, pages 115–125. International Society for Optics and Photonics, 2000.

J. M. Hill. The large binocular telescope. *Applied optics*, 49(16):D115–D122, 2010.

S. Hippler, F. Hormuth, D. J. Butler, W. Brandner, and T. Henning. Atmosphere-like turbulence generation with surface-etched phase-screens. *Opt. Express*, 14(22):10139–10148, Oct 2006. doi: 10.1364/OE.14.010139. URL `http://www.opticsexpress.org/abstract.cfm?URI=oe-14-22-10139`.

R. Holzlöhner, D. B. Calia, and W. Hackenberg. Physical optics modelling and optimization of laser guide star propagation. In *Proc. SPIE*, volume 7015, page 701521, 2008.

E. Hubble. A relation between distance and radial velocity among extra-galactic nebulae. *Proceedings of the National Academy of Sciences*, 15(3):168–173, 1929. doi: 10.1073/pnas.15.3.168. URL `http://www.pnas.org/content/15/3/168.short`.

N. Hubin, B. L. Ellerbroek, R. Arsenault, R. M. Clare, R. Dekany, L. Gilles, M. Kasper, G. Herriot, M. Le Louarn, E. Marchetti, et al. Adaptive optics for extremely large telescopes. *Proceedings of the International Astronomical Union*, 1(S232):60–85, 2005.

K. Jackson, C. Correia, O. Lardière, D. Andersen, and C. Bradley. Tomographic wavefront error estimation and measurement for Raven, a multi-object adaptive optics demonstrator. In *SPIE Astronomical Telescopes+ Instrumentation*, pages 84475F–84475F. International Society for Optics and Photonics, 2012.

D. C. Johnston and B. M. Welsh. Atmospheric turbulence sensing for a multi-conjugate adaptive optics system. In *San Diego,'91, San Diego, CA*, pages 76–87. International Society for Optics and Photonics, 1991.

D. C. Johnston and B. M. Welsh. Analysis of multiconjugate adaptive optics. *JOSA A*, 11 (1):394–408, 1994.

L. Jolissaint, J.-P. Véran, and R. Conan. Analytical modelling of adaptive optics: foundations of the phase spatial power spectrum approach. *J. Opt. Soc. Am. A*, 23(2):382–394, Feb 2006a. doi: 10.1364/JOSAA.23.000382. URL `http://josaa.osa.org/abstract.cfm?URI=josaa-23-2-382`.

L. Jolissaint, J.-P. Véran, and R. Conan. Analytical modelling of adaptive optics: foundations of the phase spatial power spectrum approach. *JOSA A*, 23(2):382–394, 2006b.

R. Joyce, C. Boyer, L. Daggert, B. Ellerbroek, E. Hileman, M. Hunten, and M. Liang. The laser guide star facility for the Thirty Meter Telescope. In *Astronomical Telescopes and Instrumentation*, pages 62721H–62721H. International Society for Optics and Photonics, 2006.

A. Kellerer, F. Vidal, E. Gendron, Z. Hubert, D. Perret, and G. Rousset. Deformable mirrors for open-loop adaptive optics. In *SPIE Astronomical Telescopes+ Instrumentation*, pages 844765–844765. International Society for Optics and Photonics, 2012.

A. N. Kolmogorov. The local structure of turbulence in incompressible viscous fluid for very large Reynolds numbers. In *Dokl. Akad. Nauk SSSR*, volume 30, pages 299–303, 1941.

H. Kuntschner, P. Amico, J. Kolb, P. Madec, R. Arsenault, M. Sarazin, and D. Summers. Operational concept of the VLT's adaptive optics facility and its instruments. In *SPIE Astronomical Telescopes+ Instrumentation*, pages 844808–844808. International Society for Optics and Photonics, 2012.

O. Lardière, D. Andersen, C. Blain, C. Bradley, D. Gamroth, K. Jackson, P. Lach, R. Nash, K. Venn, J.-P. Véran, et al. Multi-object adaptive optics on-sky results with Raven. In *SPIE Astronomical Telescopes+ Instrumentation*, pages 91481G–91481G. International Society for Optics and Photonics, 2014.

M. Le Louarn, C. Verinaud, V. Korkiakoski, and E. Fedrigo. Parallel simulation tools for AO on ELTs. volume 5490, pages 705–712, 2004. doi: 10.1117/12.551088. URL `http://dx.doi.org/10.1117/12.551088`.

M. Le Louarn, C. Béchet, and M. Tallon. Of spiders and elongated spots. In *Proceedings of the Third AO4ELT Conference, S. Esposito and L. Fini, eds*, 2013.

M. Lombini, I. Foppiani, L. Schreiber, E. Diolaiti, G. Bregoli, and G. Cosentino. Design of the multiple Laser Guide Stars wavefront sensor prototype for the E-ELT. In *SPIE Astronomical Telescopes+ Instrumentation*, pages 84474O–84474O. International Society for Optics and Photonics, 2012.

B. Macintosh, J. R. Graham, P. Ingraham, Q. Konopacky, C. Marois, M. Perrin, L. Poyneer, B. Bauman, T. Barman, A. S. Burrows, et al. First light of the gemini planet imager. *Proceedings of the National Academy of Sciences*, 111(35):12661–12666, 2014.

B. A. Macintosh, A. Anthony, J. Atwood, N. Barriga, B. Bauman, K. Caputa, J. Chilcote, D. Dillon, R. Doyon, J. Dunn, et al. The Gemini planet imager: integration and status. In *SPIE Astronomical Telescopes+ Instrumentation*, pages 84461U–84461U. International Society for Optics and Photonics, 2012.

P.-Y. Madec. Overview of deformable mirror technologies for adaptive optics and astronomy. In *SPIE Astronomical Telescopes+ Instrumentation*, pages 844705–844705. International Society for Optics and Photonics, 2012.

M. Manetti, M. Morandini, P. Mantegazza, R. Biasi, M. Andrighettoni, and D. Gallieni. VLT DSM, the control system of the largest deformable secondary mirror ever manufactured. In *SPIE Astronomical Telescopes+ Instrumentation*, pages 91484G–91484G. International Society for Optics and Photonics, 2014.

E. Marchetti, N. N. Hubin, E. Fedrigo, J. Brynnel, B. Delabre, R. Donaldson, F. Franza, R. Conan, M. Le Louarn, C. Cavadore, et al. MAD the ESO multi-conjugate adaptive optics demonstrator. In *Astronomical Telescopes and Instrumentation*, pages 317–328. International Society for Optics and Photonics, 2003.

E. Marchetti, R. Brast, B. Delabre, R. Donaldson, E. Fedrigo, C. Frank, N. Hubin, J. Kolb, M. Le Louarn, J.-L. Lizon, et al. MAD star oriented: laboratory results for ground layer and multi-conjugate adaptive optics. In *Astronomical Telescopes and Instrumentation*, pages 62720O–62720O. International Society for Optics and Photonics, 2006.

E. Marchetti, R. Brast, B. Delabre, R. Donaldson, E. Fedrigo, C. Frank, N. Hubin, J. Kolb, J.-L. Lizon, M. Marchesi, et al. MAD on sky results in star oriented mode. In *SPIE Astronomical Telescopes+ Instrumentation*, pages 70150F–70150F. International Society for Optics and Photonics, 2008.

A. Maréchal. Étude des effets combinés de la diffraction et des aberrations géométriques sur l'image d'un point lumineux. *Rev. Opt*, 26:257–277, 1947.

MATLAB. *version R2014b*. The MathWorks Inc., Natick, Massachusetts, 2014.

C. E. Max, S. S. Olivier, H. W. Friedman, J. An, K. Avicola, B. V. Beeman, H. D. Bissinger, J. M. Brase, G. V. Erbert, D. T. Gavel, et al. Image improvement from a sodium-layer laser guide star adaptive optics system. *Science*, 277(5332):1649–1652, 1997.

T. Morris, Z. Hubert, R. Myers, E. Gendron, A. Longmore, G. Rousset, G. Talbot, T. Fusco, N. Dipper, F. Vidal, et al. CANARY: The NGS/LGS MOAO demonstrator for EAGLE. In *1st AO4ELT conference-Adaptive Optics for Extremely Large Telescopes*, page 08003. EDP Sciences, 2010.

T. Morris, Z. Hubert, F. Chemla, S. Todd, E. Gendron, J.-M. Huet, E. Younger, A. Basden, N. Dipper, D. Geng, et al. CANARY phase B: the LGS upgrade to the CANARY tomographic MOAO pathfinder. In *Second International Conference on Adaptive Optics for Extremely Large Telescopes.*, volume 1, page 3P, 2011.

T. Morris, E. Gendron, A. Basden, O. Martin, J. Osborn, D. Henry, Z. Hubert, G. Sivo, D. Gratadour, F. Chemla, et al. Multiple Object Adaptive Optics: Mixed NGS/LGS tomography. In *Proceedings of the Third AO4ELT Conference*, volume 1, page 114, 2013.

R. M. Myers, A. J. Longmore, C. R. Benn, D. F. Buscher, P. Clark, N. A. Dipper, N. Doble, A. P. Doel, C. N. Dunlop, X. Gao, et al. NAOMI adaptive optics system for the 4.2-m William Herschel Telescope. In *Astronomical Telescopes and Instrumentation*, pages 647–658. International Society for Optics and Photonics, 2003.

R. M. Myers, Z. Hubert, T. J. Morris, E. Gendron, N. A. Dipper, A. Kellerer, S. J. Goodsell, G. Rousset, E. Younger, M. Marteaud, et al. CANARY: the on-sky NGS/LGS MOAO demonstrator for EAGLE. In *SPIE Astronomical Telescopes+ Instrumentation*, pages 70150E–70150E. International Society for Optics and Photonics, 2008.

B. Neichel, T. Fusco, and J.-M. Conan. Tomographic reconstruction for wide-field adaptive optics systems: Fourier domain analysis and fundamental limitations. *JOSA A*, 26(1): 219–235, 2009.

B. Neichel, F. Rigaut, M. Bec, and A. Garcia-Rissmann. Reconstruction Strategies for GeMS. In *1st AO4ELT conference-Adaptive Optics for Extremely Large Telescopes*, page 02010. EDP Sciences, 2010.

I. Newton. *Opticks:: Or, A Treatise of the Reflections, Refractions, Inflections and Colours of Light.* Opticks:: Or, A Treatise of the Reflections, Refractions, Inflections and Colours of Light. William Innys at the West-End of St. Paul's., 1730. URL `http://books.google.co.uk/books?id=GnAFAAAAQAAJ`.

R. J. Noll. Zernike polynomials and atmospheric turbulence. *JOsA*, 66(3):207–211, 1976.

J. Osborn, F. J. De Cos Juez, D. Guzman, T. Butterley, R. Myers, A. Guesalaga, and J. Laine. Using artificial neural networks for open-loop tomography. *Optics express*, 20 (3):2420–2434, 2012.

J. Osborn, D. Guzman, F. de Cos Juez, A. Basden, T. Morris, E. Gendron, T. Butterley, R. Myers, A. Guesalaga, F. S. Lasheras, et al. Open-loop tomography with artificial neural networks on CANARY: on-sky results. *Monthly Notices of the Royal Astronomical Society*, 441(3):2508–2514, 2014.

J. Paufique, J. Argomedo, R. Arsenault, R. Conzelmann, R. Donaldson, N. Hubin, L. Jochum, A. Jost, M. Kiekebusch, J. Kolb, et al. Status of the GRAAL system development: very wide-field correction with 4 laser guide-stars. In *SPIE Astronomical Telescopes+ Instrumentation*, pages 844738–844738. International Society for Optics and Photonics, 2012.

J. Pearson and S. Hansen. Experimental studies of a deformable-mirror adaptive optical system. *JOSA*, 67(3):325–332, 1977.

J. A. Perreault, T. G. Bifano, B. M. Levine, and M. N. Horenstein. Adaptive optic correction using microelectromechanical deformable mirrors. *Optical Engineering*, 41(3):561–566, 2002.

C. Petit, T. Fusco, J. Charton, D. Mouillet, P. Rabou, T. Buey, G. Rousset, J.-F. Sauvage, P. Baudoz, P. Gigan, et al. The SPHERE XAO system: design and performance. In *SPIE Astronomical Telescopes+ Instrumentation*, pages 70151U–70151U. International Society for Optics and Photonics, 2008.

T. Pfrommer, P. Hickson, and C.-Y. She. A large-aperture sodium fluorescence lidar with very high resolution for mesopause dynamics and adaptive optics studies. *Geophysical Research Letters*, 36(15), 2009.

G. Pilbratt, J. Riedinger, T. Passvogel, G. Crone, D. Doyle, U. Gageur, A. Heras, C. Jewell, L. Metcalfe, S. Ott, et al. Herschel Space Observatory – an ESA facility for far-infrared and submillimetre astronomy. *arXiv preprint arXiv:1005.5331*, 2010.

B. C. Platt et al. History and principles of shack-hartmann wavefront sensing. *Journal of Refractive Surgery*, 17(5):S573–S577, 2001.

J. Pott, M. Kürster, M. Böhm, T. Ruppel, S. Engelke, J. Trowitzsch, J. Borelli, W. Gässler, R. Rohloff, and T. Herbst. Vibration control of ELTs. *Proc. of AO4ELT*, 2, 2012.

L. A. Poyneer, D. T. Gavel, and J. M. Brase. Fast wave-front reconstruction in large adaptive optics systems with use of the fourier transform. *JOSA A*, 19(10):2100–2111, 2002.

C. A. Primmerman, D. V. Murphy, D. A. Page, B. G. Zollars, and H. T. Barclay. Compensation of atmospheric optical distortion using a synthetic beacon. *Nature*, 353(6340): 141–143, 1991.

D. J. Purll, D. R. Lobb, A. R. Barnes, R. G. Talbot, S. Rolt, D. J. Robertson, M. F. Closs, and M. Te Plate. Flight model performance of the integral field unit for the james webb space telescope's near-infrared spectrograph. In *SPIE Astronomical Telescopes+ Instrumentation*, pages 773917–773917. International Society for Optics and Photonics, 2010.

S. Rabien, N. Ageorges, L. Barl, U. Beckmann, T. Blümchen, M. Bonaglia, J. Borelli, J. Brynnel, L. Busoni, L. Carbonaro, et al. ARGOS: the laser guide star system for the LBT. In *SPIE Astronomical Telescopes+ Instrumentation*, pages 77360E–77360E. International Society for Optics and Photonics, 2010.

R. Ragazzoni. Pupil plane wavefront sensing with an oscillating prism. *Journal of modern optics*, 43(2):289–293, 1996.

R. Ragazzoni. Robust tilt determination from Laser Guide Stars using a combination of different techniques. *Astronomy and Astrophysics*, 319:L9–L12, Mar. 1997.

R. Ragazzoni, S. Esposito, and E. Marchetti. Auxiliary telescopes for the absolute tip–tilt determination of a laser guide star. *Monthly Notices of the Royal Astronomical Society*, 276(1):L76–L78, 1995.

R. Ragazzoni, E. Marchetti, and F. Rigaut. Modal tomography for adaptive optics. *Astronomy and Astrophysics*, 342:L53–L56, 1999.

R. Ragazzoni, E. Marchetti, and G. Valente. Adaptive-optics corrections available for the whole sky. *Nature*, 403(6765):54–56, 2000.

R. Rampy, D. Gavel, D. Dillon, and S. Thomas. Production of phase screens for simulation of atmospheric turbulence. *Applied optics*, 51(36):8769–8778, 2012.

L. Rayleigh. V. Investigations in optics, with special reference to the spectroscope. *The London, Edinburgh, and Dublin Philosophical Magazine and Journal of Science*, 9(53): 40–55, 1880.

A. Reeves, R. Myers, T. Morris, A. Basden, and N. Bharmal. Real-Time Laser Guide Star Elongation and Uplink Turbulence in the Lab. In *Proceedings of the Third AO4ELT Conference*, volume 1, page 35, 2013.

A. P. Reeves, R. M. Myers, T. J. Morris, A. G. Basden, N. A. Bharmal, S. Rolt, D. G. Bramall, N. A. Dipper, and E. J. Younger. DRAGON: a wide-field multipurpose real time adaptive optics test bench. In *SPIE Astronomical Telescopes+ Instrumentation*, pages 84474Y–84474Y. International Society for Optics and Photonics, 2012.

O. Reynolds. On the dynamical theory of incompressible viscous fluids and the determination of the criterion. *Proceedings of the Royal Society of London*, 56(336-339):40–45, 1894.

F. Rigaut. Ground-conjugate wide field adaptive optics for the ELTs. *Beyond conventional adaptive optics*, 58:11–16, 2002.

F. Rigaut, G. Rousset, P. Kern, J. Fontanella, J. Gaffard, F. Merkle, and P. Léna. Adaptive optics on a 3.6-m telescope–Results and performance. *Astronomy and Astrophysics*, 250: 280–290, 1991.

F. Rigaut, D. Salmon, R. Arsenault, J. Thomas, O. Lai, D. Rouan, J. Véran, P. Gigan, D. Crampton, J. Fletcher, et al. Performance of the Canada-France-Hawaii Telescope Adaptive Optics Bonnette. *Publications of the Astronomical Society of the Pacific*, 110 (744):152–164, 1998.

F. Rigaut, B. Neichel, M. Bec, M. Boccas, A. Garcia-Rissmann, and D. Gratadour. A sample of GeMS calibrations and control schemes. In *1st AO4ELT conference-Adaptive Optics for Extremely Large Telescopes*, volume 8001, page 08001. EDP Sciences, 2010.

F. Rigaut, B. Neichel, M. Boccas, C. d'Orgeville, G. Arriagada, V. Fesquet, S. J. Diggs, C. Marchant, G. Gausach, W. N. Rambold, et al. GeMS: first on-sky results. In *SPIE Astronomical Telescopes+ Instrumentation*, pages 84470I–84470I. International Society for Optics and Photonics, 2012.

F. Rigaut, B. Neichel, M. Boccas, C. d'Orgeville, F. Vidal, M. A. van Dam, G. Arriagada, V. Fesquet, R. L. Galvez, G. Gausachs, et al. Gemini multiconjugate adaptive optics system review–I. Design, trade-offs and integration. *Monthly Notices of the Royal Astronomical Society*, page stt2054, 2013.

J. E. Roberts, R. G. Dekany, R. S. Burruss, C. Baranec, A. Bouchez, E. E. Croner, S. R. Guiwits, D. D. Hale, J. R. Henning, D. L. Palmer, et al. Results from the PALM-3000 high-order adaptive optics system. In *SPIE Astronomical Telescopes+ Instrumentation*, pages 84470Y–84470Y. International Society for Optics and Photonics, 2012.

F. Roddier. The Effects of Atmospheric Turbulence in Optical Astronomy. *Progress in optics*, 19:281–376, 1981.

F. Roddier. *Adaptive optics in astronomy.* Cambridge university press, 1999.

F. Roddier and C. Roddier. Curvature sensing and compensation: a new concept in adaptive optics. In *Very Large Telescopes and their Instrumentation, Vol. 2*, volume 2, pages 667–673, 1988.

S. Rolt, A. Basden, N. Bharmal1a, D. Bramall, N. Dipper, D. Geng, T. Morris, R. Myers, and A. Reeves. DRAGON, a flexible, visible-light AO testbed. In *Second International Conference on Adaptive Optics for Extremely Large Telescopes.*, volume 1, page 8P, 2011.

M. Rosensteiner. Cumulative reconstructor: fast wavefront reconstruction algorithm for extremely large telescopes. *JOSA A*, 28(10):2132–2138, 2011.

M. Rosensteiner and R. Ramlau. Kaczmarz algorithm for multiconjugated adaptive optics with laser guide stars. *JOSA A*, 30(8):1680–1686, 2013.

G. Rousset, J. Fontanella, P. Kern, P. Gigan, and F. Rigaut. First diffraction-limited astronomical images with adaptive optics. *Astronomy and Astrophysics*, 230:L29–L32, 1990.

G. Rousset, F. Lacombe, P. Puget, E. Gendron, R. Arsenault, P. Y. Kern, D. Rabaud, P.-Y. Madec, N. N. Hubin, G. Zins, et al. Status of the VLT Nasmyth adaptive optics system (NAOS). In *Astronomical Telescopes and Instrumentation*, pages 72–81. International Society for Optics and Photonics, 2000.

G. Rousset, F. Lacombe, P. Puget, N. N. Hubin, E. Gendron, T. Fusco, R. Arsenault, J. Charton, P. Feautrier, P. Gigan, et al. NAOS, the first AO system of the VLT: on-sky performance. In *Astronomical Telescopes and Instrumentation*, pages 140–149. International Society for Optics and Photonics, 2003.

J. D. Schmidt. *Numerical Simulations of Optical Wave Propagation with examples in MATLAB®*. Society of Photo-Optical Instrumentation Engineers (SPIE), 2010. ISBN 9780819483263.

L. Schreiber, I. Foppiani, C. Robert, E. Diolaiti, J.-M. Conan, and M. Lombini. Laser guide stars for extremely large telescopes: efficient Shack–Hartmann wavefront sensor design using the weighted centre–of–gravity algorithm. *Monthly Notices of the Royal Astronomical Society*, 396(3):1513–1521, 2009.

H. Shepherd, J. Osborn, R. Wilson, T. Butterley, R. Avila, V. Dhillon, and T. Morris. Stereo-SCIDAR: optical turbulence profiling with high sensitivity using a modified SCIDAR instrument. *Monthly Notices of the Royal Astronomical Society*, 437(4):3568–3577, 2014.

G. Sivo, C. Kulcsár, J.-M. Conan, H.-F. Raynaud, E. Gendron, A. Basden, F. Vidal, T. Morris, S. Meimon, C. Petit, et al. Full LQG control with vibration mitigation: from theory to first on-sky validation on the CANARY MOAO demonstrator. In *Adaptive Optics: Methods, Analysis and Applications*, pages OTu2A–2. Optical Society of America, 2013.

G. Sivo, C. Kulcsár, J.-M. Conan, H.-F. Raynaud, É. Gendron, A. Basden, F. Vidal, T. Morris, S. Meimon, C. Petit, et al. First on-sky SCAO validation of full LQG control with vibration mitigation on the CANARY pathfinder. *Optics Express*, 22(19):23565–23591, 2014.

J. A. Stoesz, J.-P. Veran, F. J. Rigaut, G. Herriot, L. Jolissaint, D. Frenette, J. Dunn, and M. Smith. Evaluation of the on-sky performance of Altair. In *SPIE Astronomical Telescopes+ Instrumentation*, pages 67–78. International Society for Optics and Photonics, 2004.

K. Strehl. *Theorie des fernrohrs: auf grund der beugung des Lichts*. JA Barth (A. Meiner), 1894.

K. Strehl. Über luftschlieren und zonenfehler. *Zeitschrift für Instrumentenkunde*, 22:213–217, 1902.

S. Ströbele, P. La Penna, R. Arsenault, R. Conzelmann, B. Delabre, M. Duchateau, R. Dorn, E. Fedrigo, N. Hubin, J. Quentin, et al. GALACSI system design and analysis. In *SPIE Astronomical Telescopes+ Instrumentation*, pages 844737–844737. International Society for Optics and Photonics, 2012.

S. Stroebele et al. The ESO adaptive optics facility. In *Astronomical Telescopes and Instrumentation*, pages 62720B–62720B. International Society for Optics and Photonics, 2006.

H. Takami, N. Takato, M. Otsubo, T. Kanzawa, Y. Kamata, K. Nakashima, and M. Iye. Adaptive optics system for Cassegrain focus of Subaru 8.2-m telescope. In *Astronomical Telescopes & Instrumentation*, pages 500–507. International Society for Optics and Photonics, 1998.

H. Takami, N. Takato, Y. Hayano, M. Iye, S. Oya, Y. Kamata, T. Kanzawa, Y. Minowa, M. Otsubo, K. Nakashima, et al. Performance of Subaru Cassegrain adaptive optics system. *Publications of the Astronomical Society of Japan*, 56(1):225–234, 2004.

R. Tamai and J. Spyromilio. European Extremely Large Telescope: progress report. In *SPIE Astronomical Telescopes+ Instrumentation*, pages 91451E–91451E. International Society for Optics and Photonics, 2014.

V. Tatarski, R. Silverman, and N. Chako. Wave Propagation in a Turbulent Medium. *Physics Today*, 14:46, 1961.

G. I. Taylor. The spectrum of turbulence. In *Proceedings of the Royal Society of London A: Mathematical, Physical and Engineering Sciences*, volume 164, pages 476–490. The Royal Society, 1938.

L. A. Thompson and R. M. Castle. Experimental demonstration of a Rayleigh-scattered laser guide star at 351 nm. *Optics letters*, 17(21):1485–1487, 1992.

L. A. Thompson and C. S. Gardner. Experiments on laser guide stars at Mauna Kea Observatory for adaptive imaging in astronomy. *Nature*, 328:229–231, 1987.

A. Tokovinin. Seeing Improvement with Ground-Layer Adaptive Optics. *Publications of the Astronomical Society of the Pacific*, 116(824):941–951, 2004.

A. Tokovinin, M. Le Louarn, E. Viard, N. Hubin, and R. Conan. Optimized modal tomography in adaptive optics. *Astronomy & Astrophysics*, 378(2):710–721, 2001.

T. N. Truong, A. H. Bouchez, R. S. Burruss, R. G. Dekany, S. R. Guiwits, J. E. Roberts, J. C. Shelton, and M. Troy. Design and implementation of the PALM-3000 real-time control system. In *SPIE Astronomical Telescopes+ Instrumentation*, pages 84472F–84472F. International Society for Optics and Photonics, 2012.

P. Turri, D. R. Andersen, J.-P. Véran, P. Spanò, M. Rosensteiner, and E. A. McVeigh. An MCAO test bench for NFIRAOS. In *SPIE Astronomical Telescopes+ Instrumentation*, pages 91485Y–91485Y. International Society for Optics and Photonics, 2014.

G. A. Tyler. Rapid evaluation of d0: the effective diameter of a laser-guide-star adaptive-optics system. *JOSA A*, 11(1):325–338, 1994.

M. Van Dam, A. H. Bouchez, R. Conan, and B. A. McLeod. Wavefront Reconstruction for a Natural Guide Star Ground Layer Adaptive Optics System on the Giant Magellan Telescope. *Adaptive Optics for Extremely Large Telescopes III*, 2013.

M. A. van Dam, P. M. Hinz, J. L. Codona, M. Hart, A. Garcia-Rissmann, M. W. Johns, S. A. Shectman, A. H. Bouchez, B. A. McLeod, and F. Rigaut. Modeling the adaptive optics systems on the Giant Magellan Telescope, 2010. URL `http://dx.doi.org/10.1117/12.856771`.

E. Vernet, M. Kasper, C. Vérinaud, E. Fedrigo, S. Tordo, N. Hubin, S. Esposito, E. Pinna, A. Puglisi, A. Tozzi, et al. Extreme adaptive optics system optimization with the high order test bench. In *Astronomical Telescopes and Instrumentation*, pages 62722K–62722K. International Society for Optics and Photonics, 2006.

J. Vernin, C. Muñoz-Tuñón, M. Sarazin, H. V. Ramió, A. M. Varela, H. Trinquet, J. M. Delgado, J. J. Fuensalida, M. Reyes, A. Benhida, et al. European extremely large telescope site characterization i: Overview. *Publications of the Astronomical Society of the Pacific*, 123(909):1334–1346, 2011.

F. Vidal, E. Gendron, and G. Rousset. Tomography approach for multi-object adaptive optics. *J. Opt. Soc. Am. A*, 27(11):A253–A264, Nov 2010. doi: 10.1364/JOSAA.27.00A253. URL `http://josaa.osa.org/abstract.cfm?URI=josaa-27-11-A253`.

F. Vidal, B. Neichel, F. Rigaut, R. Carrasco, C. Winge, P. Pessev, A. Serio, G. Arriagada, C. Moreno, W. Rambold, et al. GeMS: from the on-sky experimental system to science operation. The AO point of view. In *Proceedings of the Third AO4ELT Conference*, volume 1, page 46, 2013.

T. Von Kármán. Progress in the statistical theory of turbulence. *Proceedings of the National Academy of Sciences of the United States of America*, 34(11):530, 1948.

Z. Warhaft. The engine and the atmosphere: An introduction to engineering, 1997.

R. E. Williams, B. Blacker, M. Dickinson, W. Van, D. Dixon, H. C, A. S. Fruchter, M. Giavalisco, R. L. Gillil, I. Heyer, H. martin Adorf, and R. N. Hook. The hubble deep field: Observations, data reduction, and galaxy photometry. *Astronomical Journal*, 1996.

R. W. Wilson and C. R. Jenkins. Adaptive optics for astronomy: theoretical performance and limitations. *MNRAS*, 278:39–61, Jan. 1996.

P. Wizinowich, D. Acton, C. Shelton, P. Stomski, J. Gathright, K. Ho, W. Lupton, K. Tsubota, O. Lai, C. Max, et al. First light adaptive optics images from the Keck II telescope: a new era of high angular resolution imagery. *Publications of the Astronomical Society of the Pacific*, 112(769):315–319, 2000a.

P. Wizinowich, R. Dekany, D. Gavel, C. Max, S. Adkins, B. Bauman, J. Bell, A. Bouchez, M. Britton, J. Chin, et al. [WM Keck Observatory's next-generation adaptive optics facility. In *SPIE Astronomical Telescopes+ Instrumentation*, pages 701511–701511. International Society for Optics and Photonics, 2008.

P. L. Wizinowich, D. S. Acton, O. Lai, J. Gathright, W. Lupton, and P. J. Stomski Jr. Performance of the WM Keck observatory natural guide star adaptive optic facility: The first year at the telescope. In *Astronomical Telescopes and Instrumentation*, pages 2–13. International Society for Optics and Photonics, 2000b.

P. L. Wizinowich, D. Le Mignant, A. H. Bouchez, R. D. Campbell, J. C. Chin, A. R. Contos, M. A. van Dam, S. K. Hartman, E. M. Johansson, R. E. Lafon, et al. The WM Keck Observatory laser guide star adaptive optics system: overview. *Publications of the Astronomical Society of the Pacific*, 118(840):297–309, 2006.

L. Zhang, H. Jiang, S. Cui, J. Hu, and Y. Feng. Versatile Raman fiber laser for sodium laser guide star. *Laser & Photonics Reviews*, 8(6):889–895, 2014.